DE-EE0006375

Final Project Report

Open-source FCPEM-Performance & Durability Model

Consideration of Membrane Properties on Cathode Degradation

Submitted to the U.S. Department of Energy

20 January 2017

By

Ballard Fuel Cell Systems Inc.
63065 NE 18th Street
Bend, Oregon 97701
Phone: 541-639-8640
DUNS #078639476
USA

Shanna Knights, David Harvey (PI)
Email: shanna.knights@ballard.com

Prime Contractor: **Ballard Fuel Cell Systems Inc.**

Project Collaborators: **Dr. Kateryna Artyushkova** – Center for Emerging Energy Technologies, University of New Mexico, School of Engineering (UNM)

Foreword and Acknowledgements

This report summarizes and documents the work conducted by Ballard Fuel Cell Systems Inc and its sub-contractors under the DOE Federal Assistance Contract DE-EE0006375 “Open-source FCPEM-Performance & Durability Model Consideration of Membrane Properties on Cathode Degradation”. This work, covering the period of January 1, 2014 to May 31, 2015, is an extension of the work that commenced under the recently completed project DE-EE0000466: “Micro-structural Mitigation Strategies for PEM Fuel Cells: Morphological Simulation and Experimental Approaches.

The overall objective of this project extension is to enhance the predictive capability of the PEM Fuel Cell Performance & Durability Model called FC-APOLLO (Application Package for Open-source Long Life Operation) by including interaction effects of membrane transport properties such as water transport, changes in proton conductivity, and overall water uptake/adsorption and the state of the catalyst layer local conditions to further understand the driving forces for platinum dissolution.

The project was led by Ballard Fuel Cell Systems Inc via a direct subcontract to Ballard Power Systems and included contributions from the other subcontractor, University of New Mexico. Ballard’s work, which encompassed the development of the performance and degradation models as well as experimental investigation for model validation and the correlation development, was carried out at Ballard Power Systems’ facility in Burnaby, B.C. Canada.

Ballard recognizes the significant contribution made by the project collaborators and their team members. As well, Ballard recognizes the support provided from the DOE project managers Dr. David Peterson and Donna Ho, and the project technical advisor, Dr. John Kopasz.

Ballard recognizes the contributions of Dr. Silvia Wessel during her years of service, including her leadership of the DE-EE0000466 and DE-EE0006375 projects, and wishes her well during her retirement.

This material is based upon work supported by the Department of Energy, Office of Energy Efficiency and Renewable Energy (EERE), under Award Number DE-EE0006375.

Executive Summary

The durability of PEM fuel cells is a primary requirement for large scale commercialization of these power systems in transportation and stationary market applications which target operational lifetimes of 5,000 hours and 60,000 hours by 2020, respectively. Key degradation modes contributing to fuel cell lifetime limitations have been largely associated with the platinum-based cathode catalyst layer. Furthermore, as fuel cells are driven to low cost materials and lower catalyst loadings in order to meet the cost targets for commercialization, the catalyst durability has become even more important. While over the past few years significant progress has been made in identifying the underlying causes of fuel cell degradation and key parameters that greatly influence the degradation rates, many gaps with respect to knowledge of the driving mechanisms still exist; in particular, the acceleration of the mechanisms due to different membrane compositions remains an area not well understood.

The focus of this project extension was to enhance the predictive capability of the PEM Fuel Cell Performance & Durability Model called FC-APOLLO (Application Package for Open-source Long Life Operation) by including interaction effects of membrane transport properties such as water transport, changes in proton conductivity, and overall water uptake/adsorption and the state of the catalyst layer local conditions to further understand the driving forces for platinum dissolution.

The major technical areas/issues of catalyst and catalyst layer performance and durability that were addressed were:

1. Membrane properties
    - Effect of the membrane properties on the local conditions within the catalyst layer.
2. Catalyst and catalyst layer degradation mechanisms (Pt dissolution, agglomeration, Pt loss)
    - Relationships between MEA performance, catalyst and catalyst layer degradation and operational conditions, catalyst layer composition, structure, and membrane properties
3. Catalyst performance
    - Relationships between membrane structure changes and performance
4. Membrane water transport
    - Effect of membrane properties and operational conditions on predicted water fluxes in the membrane

The key accomplishments of this project are:

1. Correlations that link membrane transport properties with MEA performance and durability
    - Effect of membrane transport properties on performance and catalyst layer degradation

- Impact of membrane degradation on performance and the Pt dissolution mechanism
- Correlations of XPS catalyst layer speciation content changes with in situ membrane transport properties and membrane degradation effects

2. A design flow path of interactions from membrane materials properties to effective membrane transport properties
3. Continued development of the FC-APOLLO code base, which has further transitioned into the FAST-FC platform. Development of the membrane and degradation physics will continue according to a publically available roadmap. Ballard Power Systems will continue to support the work by providing access to relevant data sets for model validation.

Contents

List of Figures

List of Tables

List of Abbreviations

AA	Atomic Absorption
AST	Accelerated Stress Test
BFCS	Ballard Fuel Cell Systems
BMP	Ballard Material Products
BOL = BOT	Beginning of Life = Beginning of Test
BPS	Ballard Power Systems
CB	Carbon Black
CCL	Cathode Catalyst Layer
CCM	Catalyst Coated Membrane
CL	Catalyst Layer
Cond	Conductivity
CV	Cyclic Voltammetry
DIP	Digital Image Processing
DLC	Double Layer Capacitance
DMA	Dynamic Mechanical Analysis
DSC	Differential Scanning Calorimetry
DFT	Density Functional Theory
ECSA	Effective Electrochemical Surface Area
EDX	Energy Dispersive X-ray Analysis
EIS	Electrode Impedance Spectroscopy
EOL = EOT	End of Life = End of Test
EPSA	Effective Pt Surface Area (cm^2 Pt / cm^2 geometric)
EW	Equivalent Weight
FA	Failure Analysis
FIB-SEM	Focused Ion Beam SEM
GDL	Gas Diffusion Layer
GIT	Georgia Institute of Technology
HFR	High Frequency Resistance
HOR	Hydrogen Oxidation Reaction
HREELS	High Resolution Electron Energy Loss Spectroscopy
HRTEM	High Resolution Transmission Electron Microscopy
HSAC	High Surface Area Carbon
HSAC-HT	High Surface Area Carbon – Heat Treated
LANL	Los Alamos National Laboratory
LPL	Lower Potential Limit
LSAC	Low Surface Area Carbon
MD	Molecular Dynamics
MEA	Membrane Electrode Assembly
MIP	Mercury Intrusion Porosimetry
MOL = MOT	Middle of Life = Middle of Test
MPL	Micro-porous Layer
MSAC	Mid-range Surface Area Carbon
MTU	Michigan Technologic University
NAA	Neutron Activation Analysis
NI	Neutron Imaging
OER	Oxygen Evolution Reaction
ORR	Oxygen Reduction Reaction
PEM	Polymer Electrolyte Membrane
PEMFC	Polymer Electrolyte Membrane Fuel Cell
PITM	Pt in the Membrane
Pt/C	Pt/Carbon Ratio
PTL	Porous Transport Layer
Queen's	Queen's University

RDE	Rotating Disk Electrode
RH	Relative humidity
SA	Surface Area
SD/SU	Shut-down/Start-up
SEM	Scanning Electron Microscopy
UNM	University of New Mexico
UoC	University of Calgary
UPL	Upper Potential Limit
VLB	Voltage Loss Breakdown
XPS	X-ray Photoelectron Spectroscopy
XRD	X-ray Diffraction

1 Introduction

1.1 Introduction and Background

To be commercially viable, automotive and stationary fuel cells must exhibit comparable performance, durability, and cost to incumbent technologies. Of greatest importance is achieving cost reduction, fuel cell performance, and durability to 5000 hrs for automotive applications and 60,000 hrs for 1 to 10kW stationary applications (2020 DOE targets) under realistic operating conditions including stop/start, low power, idling, dynamic operation, and sub-zero start-up. Although, PEMFC technology has progressively advanced towards meaningful commercialization over the last several years and has made substantial advancements towards the DOE targets, further improvements in cost and durability are needed for high volume, full scale adoption of fuel cell products in the transportation and stationary markets. Of particular interest is the durability of the catalyst and catalyst layer which remain to be substantial contributions to fuel cell performance degradation specifically as MEAs are driven to lower Pt loadings in order to meet the commercialization cost targets.

Over the years significant progress has been made in identifying catalyst degradation mechanisms[1,2] and several key parameters that greatly influence the degradation rates, including electrode potentials, potential cycling, temperature, humidity, and reactant gas composition[2,3,4,5]; however, many gaps with respect to catalyst layer degradation and an understanding of its driving mechanisms still exist. In particular, acceleration of the mechanisms under different fuel cell operating conditions, due to different structural compositions, and as a function of the drive to lower Pt loadings, remains an area not well understood. In order to close these gaps, an understanding of the effect of

---

[1] Wu, J.; Yuan, X. Z.; Martin, J. J.; Wang, H.; Zhang, J.; Shen, J.; Wu, S.; Merida, W., A review of PEM fuel cell durability: Degradation mechanisms and mitigation strategies. *Journal of Power Sources* **2008,** *184* (1), 104-119.

[2] Borup, R.; Meyers, J.; Pivovar, B.; Kim, Y. S.; Mukundan, R.; Garland, N.; Myers, D.; Wilson, M.; Garzon, F.; Wood, D.; Zelenay, P.; More, K.; Stroh, K.; Zawodzinski, T.; Boncella, J.; McGrath, J. E.; Inaba, M.; Miyatake, K.; Hori, M.; Ota, K.; Ogumi, Z.; Miyata, S.; Nishikata, A.; Siroma, Z.; Uchimoto, Y.; Yasuda, K.; Kimijima, K.-i.; Iwashita, N., Scientific Aspects of Polymer Electrolyte Fuel Cell Durability and Degradation. *Chemical Reviews* **2007,** *107* (10), 3904-3951.

[3] Shao, Y.; Yin, G.; Gao, Y., Understanding and approaches for the durability issues of Pt-based catalysts for PEM fuel cell. *Journal of Power Sources* **2007,** *171* (2), 558-566.

[4] Wilson, M. S.; Garzon, F. H.; Sickafus, K. E.; Gottesfeld, S., Surface Area Loss of Supported Platinum in Polymer Electrolyte Fuel Cells. *Journal of The Electrochemical Society* **1993,** *140* (10), 2872-2877.

[5] Ferreira, P. J.; la O', G. J.; Shao-Horn, Y.; Morgan, D.; Makharia, R.; Kocha, S.; Gasteiger, H. A., Instability of Pt/C Electrocatalysts in Proton Exchange Membrane Fuel Cells: A Mechanistic Investigation. *Journal of The Electrochemical Society* **2005,** *152* (11), A2256-A2271.

operating conditions and the layer structure and composition on catalyst layer degradation mechanisms and degradation rates is needed.

The degradation mechanisms of the catalyst layer are represented by the cartoons in Figure 1 and Figure 2. These figures show that voltage is a key driver for catalyst degradation. Within the normal range of fuel cell operation bare Pt particles will exist only at low cathode potentials (high current densities) while PtOx films are being formed at potentials of > 0.7V and possibly lower. Removal and re-forming of the PtOx layer will occur to some extent under dynamic operating condition, but specifically during shut-down and start-up of the fuel cell due to the presence of air in the anode compartment. During start-up and shut-down the cathode may experience potential spikes in excess of 1.3V; this high cathode potential is a powerful driver for carbon corrosion.

The structure of the catalyst can also greatly affect the voltage and water distribution in the catalyst layer, as well as the proton and electron conduction facilitating local operating conditions that can greatly shift the onset of the Pt dissolution and/or carbon corrosion mechanisms. Thus, a better understanding of the mechanistic interactions as a function of operating conditions, membrane and cathode structure and composition is needed to enable the MEA designer to trade off fuel cell performance, durability and cost more effectively.

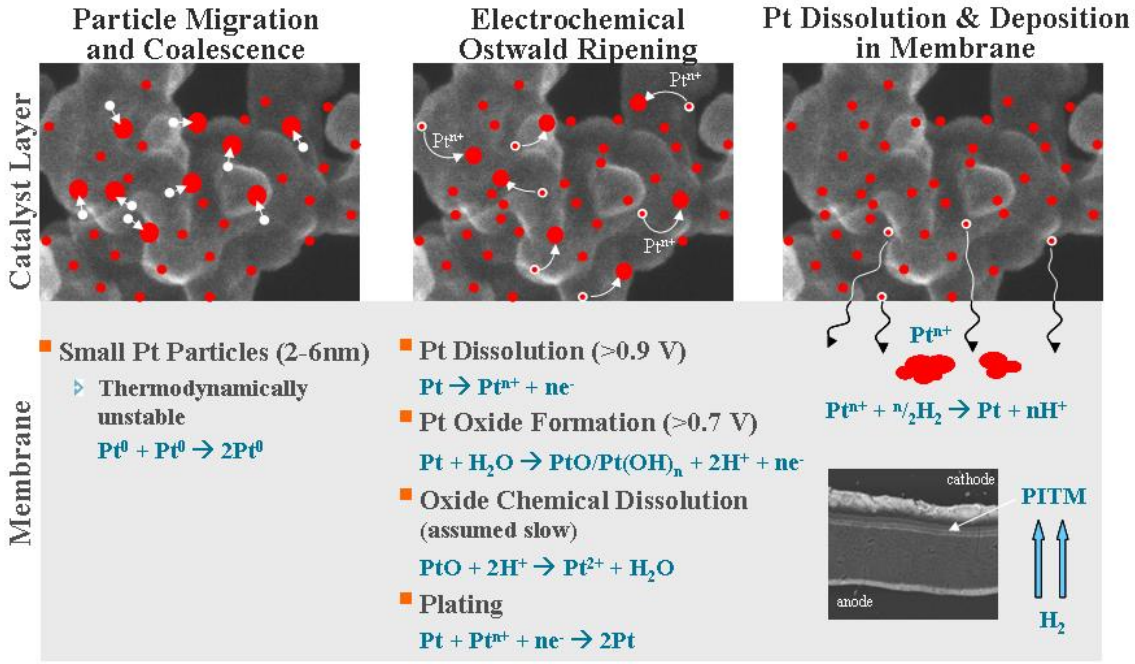

Figure 1: Representation of the Pt catalyst dissolution and agglomeration mechanisms under fuel cell operation.

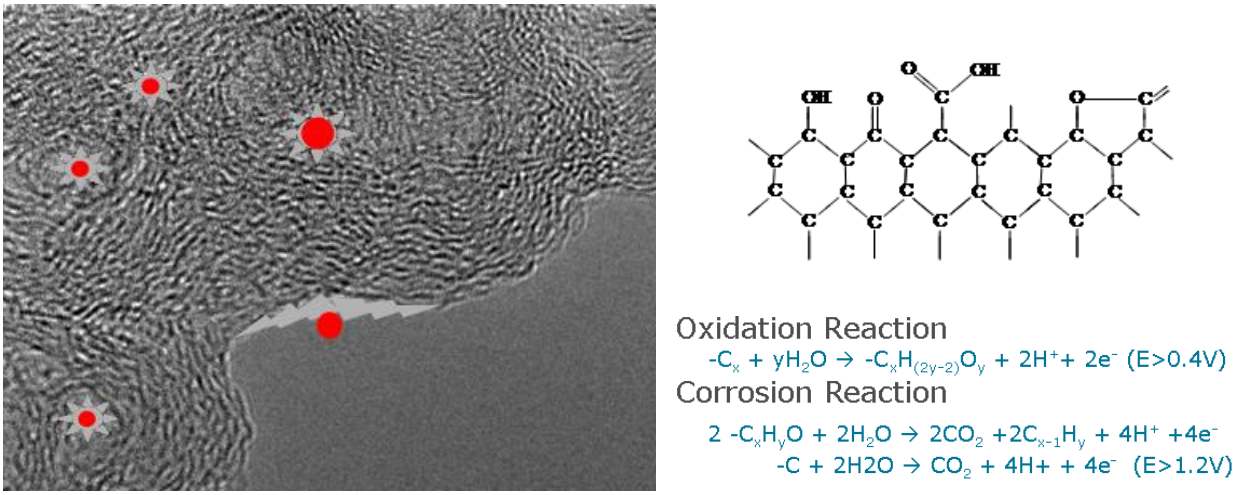

Figure 2: Depiction of the catalyst carbon support corrosion mechanisms.

Ballard's project "Micro-structural Mitigation Strategies for PEM Fuel Cells through Morphological Simulation and Experimental Design Windows" (DE-EE0000466 Ballard Material Products Inc.) addressed performance and durability, and indirectly cost, via state of the art MEA designs and materials. This project focused on the following key objectives, aligned with the 2015 technical targets for stationary and automotive fuel cell applications:

1. Identification and verification of catalyst degradation mechanisms: (a) Pt dissolution, transport, and plating, (b) carbon-support oxidation and corrosion, (c) ionomeric thinning and conductivity loss, and (d) mechanism coupling, feedback, and acceleration.
2. Correlations of compiled data for catalyst performance and structural change as a function of: (a) catalyst layer and unit cell operational conditions, (b) catalyst layer morphology and composition, and (c) gas diffusion layer (GDL) properties.
3. Development of kinetic and material models for catalyst layer aging: (a) macro-level unit cell degradation model, (b) micro-scale catalyst layer degradation model, and (c) molecular dynamics degradation model of the platinum/carbon/ionomer interface.
4. Mitigation strategies for catalyst degradation through modification of: (a) operational conditions and (b) component structural morphologies and compositions.

To address these objectives a dual path approach was taken that coupled an extensive range of experimental analysis and testing with a multi-scale modeling approach. The major technical areas/issues of catalyst and catalyst layer performance and durability that were addressed using this approach are:

1. Catalyst and catalyst layer degradation mechanisms (Pt dissolution, agglomeration, Pt loss, e.g. Pt in the membrane, carbon oxidation, and/or corrosion).

- Driving force for the different degradation mechanisms.
- Relationships between MEA performance, catalyst and catalyst layer degradation and operational conditions, catalyst layer composition, and structure.

2. Materials properties
    - Changes in catalyst, catalyst layer, and MEA materials properties due to degradation.
3. Catalyst performance
    - Relationships between catalyst structural changes and performance.
    - Stability of the three-phase boundary and its effect on performance/catalyst degradation.

This work provided significant advancements in the ability to model and design durable fuel cell products and has subsequently reduced the iterative design/test cycle process for next generation fuel cell products. However, in order to further address primary barriers to commercialization, there were several critical areas still to be addressed in the area of performance and durability.

In particular, acceleration of the mechanisms under different fuel cell operating conditions, due to different structural compositions/neighboring components, and as a function of the drive to lower Pt loadings remains an area not well understood. In order to close these gaps an understanding of the effect of the membrane properties on the local conditions within the catalyst layer and the subsequent manifestation of those local conditions on performance and durability, in particular the catalyst layer degradation mechanisms and rates, was needed.

Membrane properties such as water and proton transport and changes due to degradation such as thinning, equivalent weight change, pinhole formation, or degradation by-products can affect the voltage degradation rate due to different water transport rates, or surface interactions at the platinum reactions sites and/or nature of the degradation reactions proceeding within the catalyst layer[6,7]. As an example, internal results had shown a 3-fold increase in voltage degradation rate at an upper potential of 1.3V for two different membrane types that exhibit different water transport properties (shown in Figure 3). Furthermore, as the membrane degrades, changes in the local water content and behavior of the cathode catalyst layer are possible, which will influence the move to lower loaded, cost effective catalyst materials.

---

[6] Christ, J. M.; Neyerlin, K. C.; Wang, H.; Richards, R.; Dinh, H. N., Impact of Polymer Electrolyte Membrane Degradation Products on Oxygen Reduction Reaction Activity for Platinum Electrocatalysts. *Journal of The Electrochemical Society* **2014,** *161* (14), F1481-F1488.

[7] Zhang, J.; Litteer, B. A.; Coms, F. D.; Makharia, R., Recoverable Performance Loss Due to Membrane Chemical Degradation in PEM Fuel Cells. *Journal of The Electrochemical Society* **2012,** *159* (7), F287-F293.

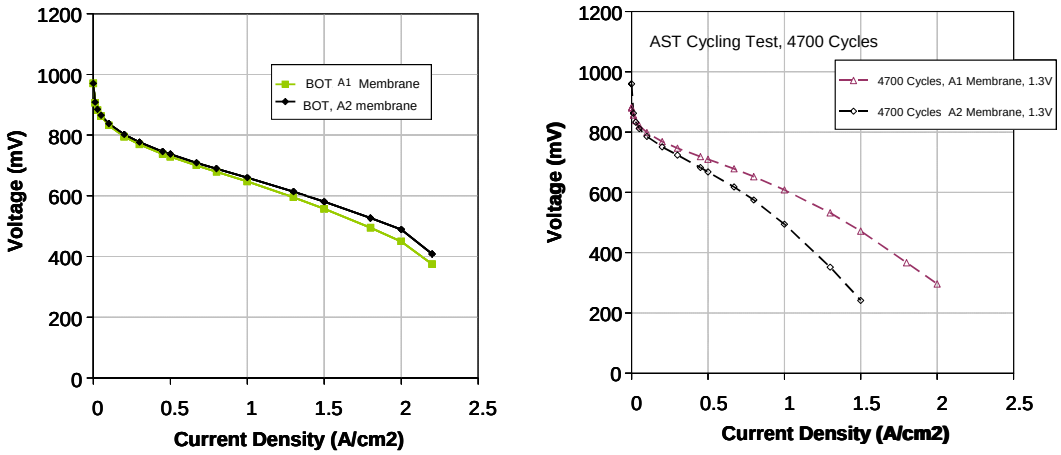

Figure 3: Membrane properties and changes during aging.

1.2 Project Objectives and Scope

This project was a 9-month extension of the work that commenced under the recently completed project DE-EE0000466: "Micro-structural Mitigation Strategies for PEM Fuel Cells: Morphological Simulation and Experimental Approaches. The overall objective of the new work was to enhance the predictive capability of the PEM Fuel Cell Performance & Durability Model called FC-APOLLO (Application Package for Open-source Long Life Operation) by including interaction effects of membrane transport properties such as water transport, changes in proton conductivity, and overall water uptake/adsorption and the state of the catalyst layer local conditions to further understand the driving forces for platinum dissolution.

The project goal was a validated extension of the originally developed FC-APOLLO that includes the capability to capture the effect of membrane type/properties and the ability to account for the membrane interaction effect on catalyst layer degradation.

This project addressed the performance and durability of Pt catalysts and catalyst layers which have been identified as key technical barriers in the DOE Hydrogen, Fuel Cell, and Infrastructure Technology Program Multi-year Research, Development, and Demonstration Plan[8]. The project follows a parallel 3-path approach of (1) theoretical simulations, (2) experimental investigations, and (3) material/component characterization (collaborative work) with the overall goal to advance the ability to model and design durable fuel cell products and subsequently reduce the iterative design/test cycle process for next generation fuel cell products.

The scope of the project included: (1) Refinement of the membrane model that is an integral part of FC-APOLLO in order to describe changes in transport properties as a function of the change in membrane type (material characteristics), (2) Quantification of

[8] http://www1.eere.energy.gov/hydrogenandfuelcells/mypp/

the impact of membrane type, transport and materials properties on the MEA performance loss mechanisms and the Pt dissolution mechanism/rate, and (3) Development of correlations that link membrane materials properties and catalyst layer effective properties to MEA/cathode performance and degradation loss mechanisms.

1.3 Approach

The technical research was separated into three sections that follow the same systematic approach as the previous work: (a) theoretical simulation, (b) experimental investigations, and (c) material/component characterization (collaborative work). The planned project deliverables were an enhanced open source PEM Fuel Cell Performance and Durability Model and a final report, including:

1. Model programming codes (Open-source)
2. Validation data used for model verification
3. Documentation on model theory and application
4. Catalyst Layer performance correlated with membrane transport properties
5. Catalyst Layer durability correlated with membrane transport properties

Workstream 1: Theoretical Simulations: Membrane Water Transport Model

The planned progression for this workstream was: i) identify the most promising set of candidate physics to describe the membrane over a broad compositional and operational design space, ii) develop a membrane sub-model and validate the physics and transport properties against ex-situ water transport data, and iii) integrate the membrane physics into the FC-APOLLO MEA model framework and then use the integrated model to explore possible interactions between catalyst degradation and membrane properties.

The model development and validation approach *as-planned* is summarized in Figure 4. The first stage is development of a prototype membrane sub-model in COMSOL, a commercial Multiphysics package. COMSOL allows for rapid model development, typically up to a certain level of complexity, and enables quick exploration of model physics and parameter sensitivities. Lessons learned from the prototype model are then used to develop the detailed membrane sub-model in an open source platform (Foam Extend). This model is validated against ex-situ water transport data to confirm proper implementation of physics and appropriate estimation of effective transport properties. After validation of the membrane sub-model, it is then incorporated into the FC-APOLLO MEA model, which is then used to understand possible interactions between membrane water transport and catalyst degradation.

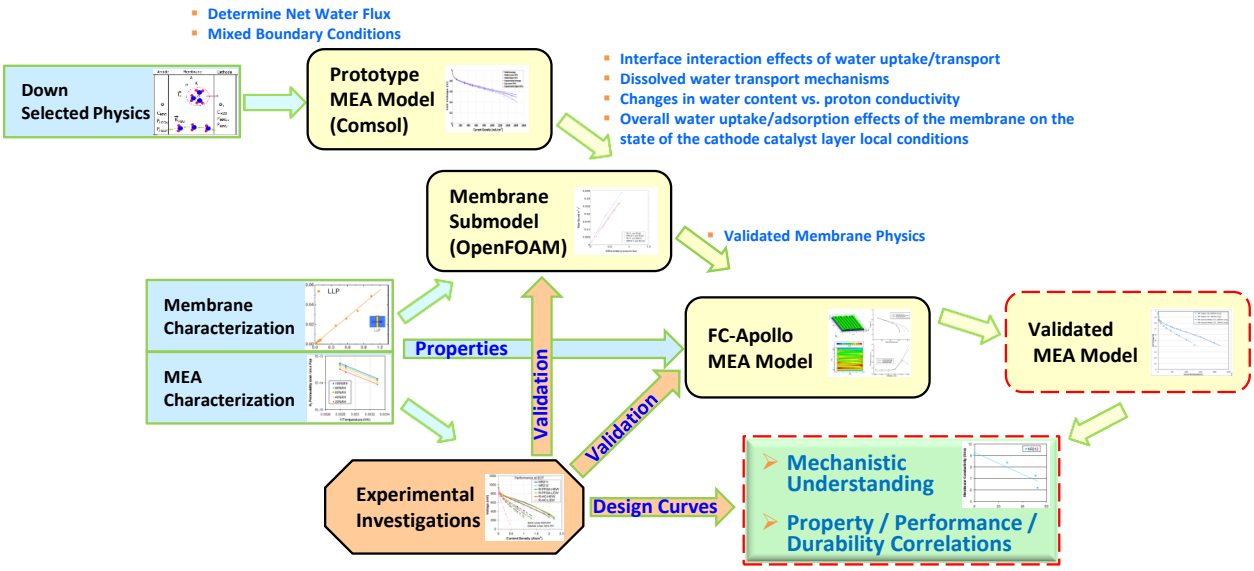

Figure 4: High-level approach for model development and validation

Workstream 2: Experimental Investigations

The objective of workstream 2 was to evaluate the impact of membrane transport properties on performance and catalyst layer degradation under a range of operating conditions, focusing on the Pt dissolution mechanism. The experimental work followed the same approach that was taken in the previous project (see Figure 5), using a variety of membranes with different transport properties and chemical and mechanical stability.

The membranes were characterized for transport and materials properties and the MEAs were subjected to AST cycling and detailed characterization of the transport characteristics (e.g. proton conductivity, reactant cross-over as a function of temperature and relative humidity etc.) and in-situ and ex-situ diagnostics to establish performance, degradation rates, and structural/compositional changes within the catalyst layer. Down-selected membranes were subjected to a Membrane Degradation AST (Ballard) which uses consecutive cycle sets of OCV to stress the chemical degradation mode of the membrane and further tested to understand the effect of changes of membrane transport properties on cathode catalyst layer degradation. The ultimate goal of this workstream was to correlate membrane degradation/transport properties with catalyst layer degradation/structure changes and to provide model validation data.

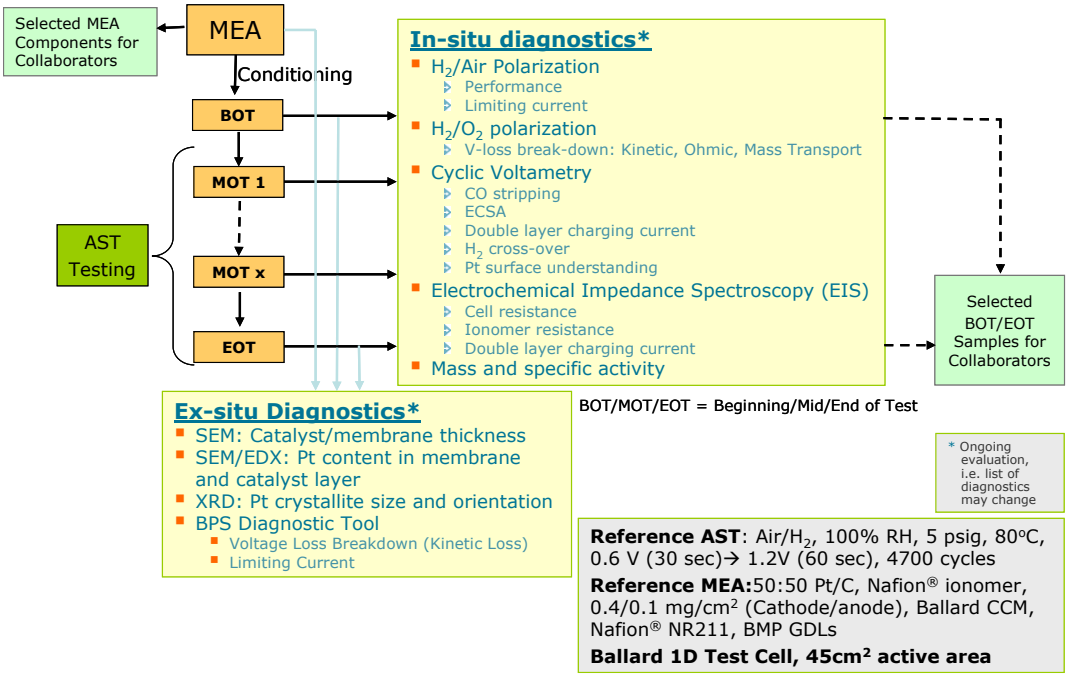

Figure 5: Schematics of the experimental approach.

Workstream 3: Material/Component Characterization (Collaborators)
The objective of the third workstream was to complement the AST investigations and modeling activities at Ballard by identifying catalyst layer surface speciation and content changes using X-ray Photoelectron Spectroscopy (XPS) measurements. This work was carried out at the University of New Mexico.

1.4 Subcontractors / Collaborators

The responsibilities and expertise of the key program team members are introduced below.

Ballard Power Systems:
Dr. Silvia Wessel was the PI for the project and was responsible for the program technical management as well as the coordination of the collaborator's activities**. David Harvey** led the modeling activities and replaced Dr. Wessel as PI upon her retirement. **Michael Lauritzen and Dr. Siyu Ye** provided technical support in their respective areas of expertise; Mr. Lauritzen in membrane transport properties and membrane/ionomer degradation; Dr. Ye in catalyst design and degradation mechanisms.

Project Collaborators:
Dr. Plamen Atanassov and **Dr. Kateryna Artyushkova** of the University of New Mexico, experts in the areas of applied electrochemistry and nano materials characterization and analysis, investigated catalyst layer surface speciation by XPS and principle component parameters.

1.5 Summary of Accomplishments

The key and unique accomplishments that have been disseminated in various forms throughout the project duration are:

- Correlations that link membrane transport properties with MEA performance and durability
    - Effect of membrane transport properties on performance and catalyst layer degradation
    - Impact of membrane degradation on performance and the Pt dissolution mechanism
    - Correlations of XPS catalyst layer speciation content changes with in situ membrane transport properties and membrane degradation effects.
- A design flow path of interactions from membrane materials properties to effective membrane transport properties

This work has provided significant advancements in the understanding of the role of membrane properties on catalyst layer durability and should assist in reducing the iterative design/test cycle process for next generation fuel cell products. Development of the FC-APOLLO code base and of the membrane and degradation physics will continue as part of the FAST-FC open source platform. Ballard Power Systems will continue to support the work by providing access to relevant data sets for model validation.

1.6 Publicatons and Conference Presentations

1.6.1 Publications

2013

1. A. Nanjundappa, A. S. Alavijeh, M. El Hannach, D. Harvey, E. Kjeang, “A customized framework for 3-D morphological characterization of microporous layers” Electrochimica Acta 110, 349-357 (2013)

2. K. Artyushkova, A. Patel, P. Atanassov, V. Colbow, M. Dutta, D. Harvey, S. Wessel, “Statistical structure-to-property relationships for fuel cell materials” Materials Characterisation VI: Computational Methods and Experiments 77, 77-86 (2013)

2014

3. Adam P Hitchcock, Viatcheslav Berejnov, Vincent Lee, Marcia West, Vesna Colbow, Monica Dutta, Silvia Wessel, “Carbon corrosion of proton exchange membrane fuel cell catalyst layers studied by scanning transmission X-ray microscopy” Journal of Power Sources 266, 66-78 (2014)

4. Adam Z. Weber, Rodney L. Borup, Robert M. Darling, Prodip K. Das, Thomas J. Dursch, Wenbin Gu, David Harvey, Ahmet Kusoglu, Shawn Litster, Matthew M. Mench, Rangachary Mukundan, Jon P. Owejan, Jon G. Pharoah, Marc Secanell, Iryna V. Zenyuk, “A critical review of modeling transport phenomena in polymer-electrolyte fuel cells” Journal of The Electrochemical Society 161 (12), F1254-F1299 (2014)

2015

5. Kateryna Artyushkova, Plamen Atanassov, Monica Dutta, Silvia Wessel, Vesna Colbow, “Structural correlations: Design levers for performance and durability of catalyst layers” Journal of Power Sources 284, 631-641(2015).

1.6.2 Conference Presentations

2013

1. B. Jayasankar, K. Karan, D. Harvey, “Platinum degradation model in the presence of oxygen” 224th ECS Meeting, San Francisco, California, October 27 - November 1, 2013

2. B. Jayasankar, D. Harvey, K. Karan, “Analyses of Kinetic Models for Oxygen Reduction Reaction” 223rd ECS Meeting, Toronto, Ontario, Canada, May 12 - 16, 2013

2014

3. B. Jayasankar, K. Karan, D. Harvey, “Modeling ORR/Oxide Formation and Pt Dissolution-from Liquid Electrolyte to Polymer Electrolyte Systems: Issues and Approaches” 225th ECS Meeting, Orlando, Florida, May 11-15, 2014

2015

4. M. Dutta, L. Ghassemzadeh, M. Lauritzen, D. Harvey, S. Wessel, A. P. Young, “Impact of Membrane Properties and Membrane Degradation on Cathode Catalyst Layer Degradation” 228th ECS Meeting, Phoenix, Arizona, October 11-15, 2015

1.6.3 Other Technical Presentations

2014

1. 2014 Annual Merit Review Presentation, Washington, June 18, 2014
2. Fuel Cell Tech Team Presentation, Detroit, April 9, 2014
3. Technical Progress Review, Vancouver, September 17, 2014

2015

4. 2015 Annual Merit Review Presentation, Washington, June 8, 2015
5. 2015 Annual Merit Review Workshop, FC-Apollo, Washington, June 10, 2015

2 Experimental Investigations of the Effect of Membrane Properties on Performance and Catalyst Layer Degradation

2.1 Objective/Scope/Approach

The overall objective of this workstream was to understand the effect of membrane properties on cathode degradation (Pt dissolution) and correlate membrane properties with Beginning of Test (BOT) performance and cathode degradation. In-situ accelerated stress test (AST) based fuel cell experimental investigations for MEA performance and degradation were conducted. These results were intended to serve as validation for the developed models.

This workstream consisted of three subtasks:

Task 2.1: Effect of Membrane Transport Properties on Performance and Catalyst Layer Degradation
Task 2.2: Impact of Membrane Degradation on the Pt Dissolution Mechanism
Task 2.3: Correlation of Membrane Type and Transport Properties with MEA Performance and Durability

Task 2.1 and Task 2.2 will be discussed in sections 2.3.1 and 2.3.2, respectively. In addition, these sections will also cover the details of the correlations developed for Task 2.3 as the related results are discussed.

2.2 Experimental Details

Test Hardware and Reference MEA

The test hardware used in this project was designed by Ballard to provide quasi-uniform operational conditions with the following features: bladder compression, high flow rates, liquid cooled temperature control, carbon composite plates with parallel flow fields designed for low pressure and uniform flow, and an active area of 45 cm^2. A reference MEA was used made of a catalyst coated membrane (CCM) with a Pt loading of 0.4/0.1 mg/cm^2 (cathode/anode), Pt supported on graphitized carbon, a 50:50 Pt/C ratio, and Nafion® ionomer. The CCM was manufactured in-house using the Nafion® NR211 membrane. The gas diffusion layers (GDL) were made by AvCarb using a continuous process.

Accelerated Cathode Stress Test Protocol

A Ballard preferred reference cathode AST protocol for this program used a square voltage cycling profile. As this protocol is substantially different to the DOE recommended electrocatalyst AST protocol, a comparison between the two protocols was undertaken. The three primary AST protocol differences are: (1) N_2 vs. Air, (2) voltage cycling profile and (3) 1.0V vs. 1.2V upper potential. The DOE AST was adapted, in terms of inlet pressure and flow rates, to enable operation in the Ballard research hardware. Details of the two ASTs are given in Table 1.

Table 1: Summary of DOE and Ballard AST conditions.

Attributes	DOE AST Adapted for BPS Hardware	Ballard AST
Cycle Profile	Triangular Wave	Square Wave
	0.6V to 1.0V, 50mV/s	0.6V (30s) to 1.2V (60s)
Time / Cycle	16s	90s
Number of Cycles	30,000	5,000
Total Cycling Time	133 hours	125 hours
Temperature	80°C	80°C
RH Anode/Cathode	100% / 100%	100% / 100%
Fuel / Oxidant	H_2 4450 sccm N_2 9000 sccm	H_2 4450 sccm 21%O_2/N_2 9000 sccm
Pressure	5 psig	5 psig

The comparison of DOE and Ballard AST results indicates that the performance and ECSA losses are very similar (Figure 6) and consistent with predominately kinetic performance changes for both ASTs at lower current densities and some contribution of non-kinetic losses occurring at higher current densities. However, the Ballard AST shows higher performance losses at higher current densities and there is a significant discrepancy in the degradation mechanisms resulting from the different ASTs.

Figure 7a shows that the DOE AST resulted in larger average Pt crystallite growth compared to the Ballard AST (9.3 nm vs. 7.4 nm). This is expected since the DOE AST exhibits Pt accumulation at the cathode/membrane interface resulting in larger Pt crystallites at the interface, while the Ballard AST resulted in Pt in the membrane (PITM) (Figure 7 b and c). The primary operational factor accounting for these differences is the oxidant gas (air vs. N_2) used during the AST.

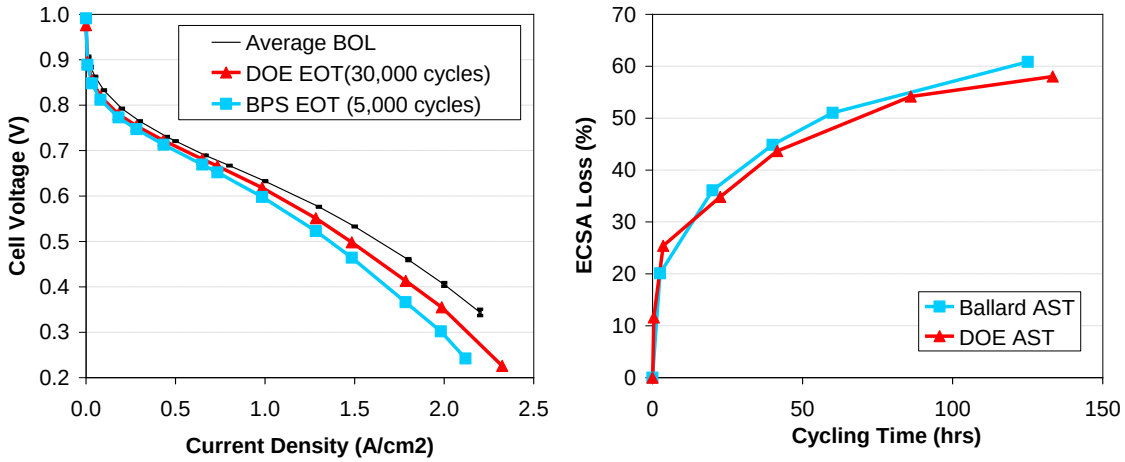

a) b)

Figure 6: End of test (EOT) data for both the DOE and the Ballard ASTs. (a) Performance diagnostics were done at 65°C, 100%RH, 5 psig. (b) ECSA obtained using CO-stripping.

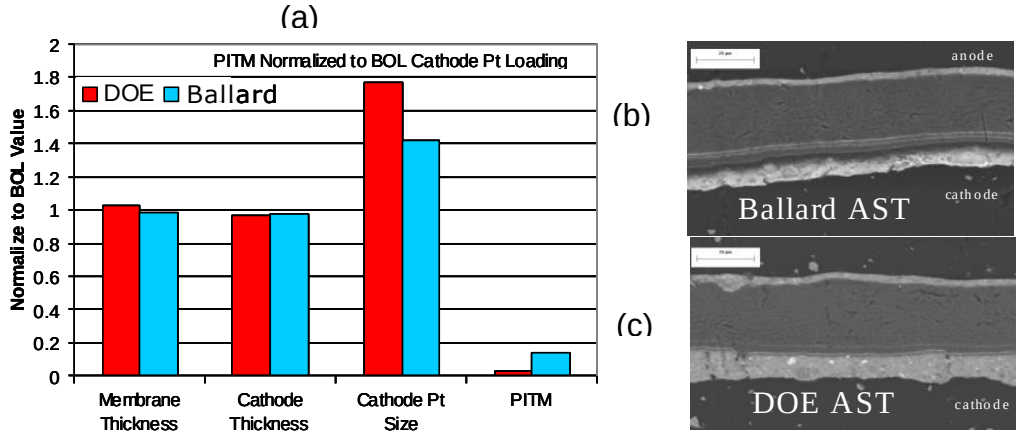

Figure 7: Ex-situ characterization at end of test (EOT) for the DOE and Ballard ASTs. (a) Quantification of the changes in membrane and the cathode catalyst layer. (b) SEM of MEA cross-section tested using Ballard AST at EOT. (c) SEM of MEA cross-section tested using DOE AST at EOT.

Table 2 lists the failure modes, advantages and the limitations associated with using either air or N_2 during the AST. Based on the findings it was recommended to use the Ballard reference voltage degradation AST in this program for the following operational features: (1) Square wave potential cycling provides better control of upper and lower potential limits and more accurate control of dwell times resulting in accurate operational design curves; (2) Air operation is more realistic to field data and will enable quantification of PITM; (3) The upper potential limit of 1.2V used in conjunction with the Ballard reference MEA enables better comparisons of state-of-the-art catalysts.

Table 2: Effect of different oxidants (air vs. N_2) on AST results.

Oxidant	Failure Modes	Advantages	Limitations
Nitrogen	▪ Pt Agglomeration ▪ Carbon Surface Oxidation ▪ Carbon Corrosion	▪ Relationships can be established without interference of other degradation modes ▪ RH can be controlled (No product water effects)	▪ Does not simulate PITM ▪ Does not take into account possible interference of membrane degradation bi-products
Air	▪ Pt Agglomeration ▪ PITM ▪ Carbon Surface Oxidation ▪ Carbon Corrosion	▪ Effect of Membrane Degradation (bi-products) on voltage degradation are captured ▪ Will capture effect of ionomer degradation ▪ More realistic to field data	▪ More difficult to control RH due to water production ▪ May be more difficult to separate failure modes ▪ More difficult to control/ set-up equipment (potentiostat & loadbank)

Accelerated Membrane Stress Test Protocol

Initially, a membrane stress test protocol which alternated between chemical and mechanical degradation phases was proposed as shown in Figure 8. This was later

considered to be too harsh, and lead to difficulties with data interpretation and modelling, due to the formation of pinholes and tears in the membrane. Therefore the mechanical portion of the AST was eliminated and the modified cyclic OCV AST consisted of a chemical degradation OCV phase with operation at increased temperature, increased oxygen concentration and decreased relative humidity followed by a short diagnostic phase. MEAs for membrane degradation were subjected to a maximum of 3 modified cyclic OCV AST cycles.

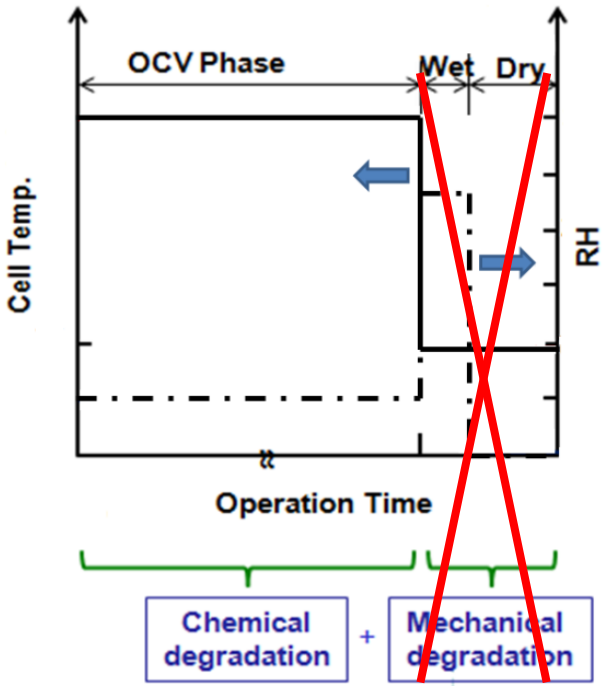

Figure 8: Schematic of the cyclic OCV membrane stress test protocol, consisting of chemical and mechanical degradation phases. The wet/dry phase leading to mechanical degradation was eliminated for this body of work**.**

Ex-situ and In-situ Characterization Techniques

A suite of characterization techniques were down-selected for in-situ and ex-situ MEA/catalyst layer diagnostics of BOL and progressively aged samples. BOT and EOT samples were also supplied to collaborators for analytical analyses. A schematic of the AST diagnostics is shown in Figure 9.

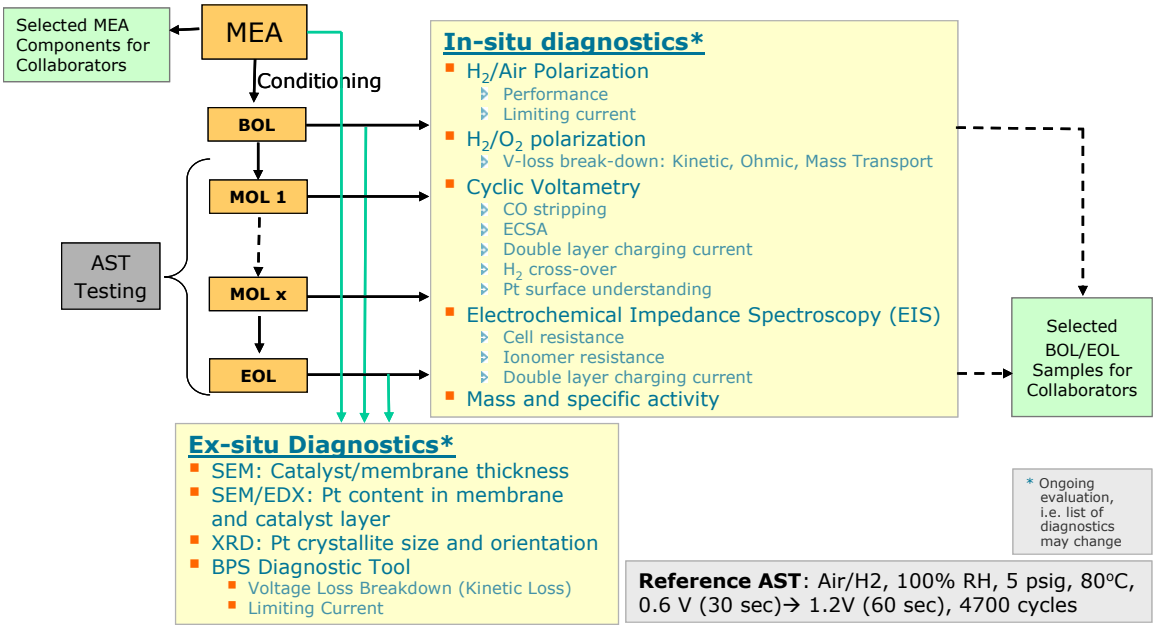

Figure 9: Schematics of AST diagnostics including list of down-selected ex-situ and in-situ measurement techniques.

Operating conditions

The cell was conditioned at standard steady state operating conditions of 75°C, 100%RH, 5 psig, 1.3 A/cm^2 as listed in Table 3. The AST conditions (Table 3) utilized 100% gas RH to maximize the amount of degradation[9,10] and minimize the required test duration. The voltage was cycled in an air (cathode)/H_2 (anode) environment from a lower potential limit (LPL) of 0.6 V_{RHE} for 30 s, to an upper potential limit (UPL) of 1.2 V_{RHE} for 60 s. During the AST period, polarization curves, CV and EIS measurements were conducted after 0, 50, 700, 1400, 2100, 2800 and 4700 cycles. SEM and XRD analyses were conducted with beginning of test (BOT) and degraded end of test (EOT) MEAs. As discussed the standard AST held the UPL for 60 s in order to accelerate the degradation; however, in an operating system the PEMFC would only experience high UPLs for much shorter durations, typically of less than 1 sec.

[9] Maass, S.; Finsterwalder, F.; Frank, G.; Hartmann, R.; Merten, C., Carbon support oxidation in PEM fuel cell cathodes. *Journal of Power Sources* **2008,** *176* (2), 444-451.
[10] Stevens, D. A.; Hicks, M. T.; Haugen, G. M.; Dahn, J. R., Ex Situ and In Situ Stability Studies of PEMFC Catalysts: Effect of Carbon Type and Humidification on Degradation of the Carbon. *Journal of The Electrochemical Society* **2005,** *152* (12), A2309-A2315.

Table 3: List of operating conditions for standard fuel cell operation and the cathode accelerated stress test.

Operating Conditions	Temperature (°C)	Pressure (psig)	Oxidant Flow Rate (slpm)	Fuel Flow Rate (slpm)	Anode & Cathode Gas RH %	Current Density (A/cm^2)
Standard	75	5	9 (air)	4.45 (H_2)	100	1.3
AST	80	5	9 (air)	4.45 (H_2)	100	

Cyclic Voltammetry (CV)

CV scans were conducted using a Solatron SI1287 potentiostat to calculate the ECSA, the H_2 crossover current, and the double layer capacitance (C_{dl}). Hydrogen present at the anode acted as the reference electrode, while the cathode potential was cycled between 0.1–1.2 V_{RHE} at 20 mV/s. The ECSA was determined by CO stripping, assuming a charge density of 420 $\mu C/cm^2$ to break the linear Pt-CO bond.[11]

Electrochemical Impedance Spectroscopy (EIS)

EIS measurements were taken by applying a 10 mV AC perturbation signal with a 0.45 V_{RHE} DC bias potential. A SI1287 Solatron potentiostat and a 1250 Solatron Frequency Response analyzer were used in a 4-electrode configuration to sweep the frequency between 50 kHz to 0.05 Hz. The bias potential was applied to eliminate any pseudo-capacitive effects that result from hydrogen and oxygen adsorption-desorption.[12] Z-plot and Z-view software were used to conduct and analyze the EIS spectra to determine the impedance and capacitance. Measurements were taken in a nitrogen and hydrogen atmosphere on the cathode and anode, respectively. The EIS spectra were fit to an equivalent circuit representing a transmission line network of the porous catalyst layer (CL). As discussed elsewhere[13] in greater detail, the fitted parameters consisted of the high frequency cell resistance, the cathode CL protonic resistance, and the double layer capacitance (Cdl).

[11] Ralph, T. R.; Hards, G. A.; Keating, J. E.; Campbell, S. A.; Wilkinson, D. P.; Davis, M.; St-Pierre, J.; Johnson, M. C., Low Cost Electrodes for Proton Exchange Membrane Fuel Cells: Performance in Single Cells and Ballard Stacks. *Journal of The Electrochemical Society* **1997,** *144* (11), 3845-3857.

[12] Easton, E. B.; Pickup, P. G., An electrochemical impedance spectroscopy study of fuel cell electrodes. *Electrochimica Acta* **2005,** *50* (12), 2469-2474.

[13] Young, A. P.; Stumper, J.; Gyenge, E., Characterizing the Structural Degradation in a PEMFC Cathode Catalyst Layer: Carbon Corrosion. *Journal of The Electrochemical Society* **2009,** *156* (8), B913-B922.

Water Crossover

Water crossover was measured at the end of test using a specialized setup, containing outlet heaters, and sensors[14]. The inlet humidification water was accurately controlled, while the amount of water in the anode and cathode exhaust streams was determined by heating the outlet streams to vaporize all of the water and measuring temperature, relative humidity and pressure to calculate the outlet water contents. The outlet gas water content of each gas stream was compared against the inlet water humidification and water production at the cathode to determine the net water transferred between cathode and anode. Net water crossover towards the cathode is reported as positive water crossover, while net water crossover toward the anode is reported as negative values. The water balance closes within 3%.

Dynamic Vapor Sorption

Water uptake of the bare membranes was measured using Quantachrome Instruments Hydrosorb V5.1. The as received sample (~200mg) was vacuum dried within the instrument at 110-115ºC for at least 5 hours. After this degas step the dry sample weight was measured, and the dynamic vapor sorption analysis was performed at 40ºC.

Scanning Electron Microscopy

After operation, MEA cross-sections were analyzed with a Philips XL30 SEM to detect changes in the MEA structure due to the Pt dissolution and carbon corrosion. MEA samples were cast into epoxy pucks. Pictures were taken using a backscatter detector at 400 x magnification and with a beam energy of 15 kV. The membrane and CL thickness was measured. The cathode CL thickness, in conjunction with a carbon mass balance, was used to calculate the CL porosity in new and degraded samples. The Pt content in the membrane and catalyst layers was measured using an EDS detector.

X-ray Diffraction

Powder samples of the cathode catalyst layer were scraped from the catalyst coated membrane (CCM) and submitted to an external lab for XRD analysis, where the samples were then gently stirred in an alumina mortar and smeared on a zero-background quartz plate with ethanol. Step-scan X-ray powder-diffraction data were collected over the range 6-103°2θ (0.04°2θ step, 1.5s/step) with CoKα radiation (1.7902 Å) on a Siemens (now Bruker AXS) D5000 Bragg-Brentano diffractometer equipped with an Fe monochromator foil, 0.6 mm (0.3°) divergence slit, incident- and diffracted-beam Soller slits and a VÅNTEC-1 strip detector. The long fine-focus Co X-ray tube was operated at 35 kV and 40 mA, using a take-off angle of 6°. The average platinum crystallite size was determined using the Scherrer Equation,

$$D = \kappa \lambda / (\beta \cos \theta) \quad (1)$$

[14] Bellerive, J.; Bellemare-Davis, A., Effect of Gas Diffusion Layer Design on PEM Fuel Cell MEA Water Removal in an Under Humidified Environment. *Meeting Abstracts* **2012,** *MA2012-02* (13), 1677.

where D is the diameter of the crystallite, β is the width of the peak at half maximum intensity of a specific phase (hkl) in radians, κ is the Scherrer constant equal to 0.9, λ is the wavelength of incident x-rays and θ is the center angle of the peak.

Reproducibility of MEA results

The reproducibility of performance and properties of 57 BOT MEAs is summarized in Table 4. The MEA to MEA variability was found to be within a few percent for the measured parameters with the exception of the catalyst layer ionic resistance. It is believed that the larger error is associated with MEA variability and data fitting variability.

Table 4 : Reproducibility of MEAs (BOT and EOT), including MEA and test station variability.

Characteristics	% Variation (1 Std. Deviation)	
	BOT (57 MEAs)	EOT (3 to 5 MEAs)
OCV	1	1
Air Performance, 1.0A/cm^2	3	1
Air Kinetic Loss, 1.0A/cm^2	4	0.2
ECSA	6	4
Double Layer Capacitance	5	12
Catalyst Layer Ionomer Resistance	17	12
EOT: 4700 Cycles, 80°C, 100%RH, 0.6V (30s) to 1.2V (60s), square wave		

Membrane Variations

Two membranes for each of the three membrane types, dense Nafion® membrane, reinforced perfluorosulphonic acid (R-PFSA) membrane and reinforced partially fluorinated hydrocarbon (R-HC) membrane (experimental) were selected for investigation. The dense Nafion® membranes included the baseline membrane, NR211, and NR212, while both the reinforced PFSA and reinforced partially fluorinated hydrocarbon membranes had low and high EW varieties that were studied. The membranes are summarized in Table 5 in the following section.

2.3 Results and Discussions

2.3.1 Effect of Membrane Transport Properties on Performance and Catalyst Layer Degradation

The objective of this task is to determine the impact of membrane transport properties on performance and catalyst layer degradation for a range of operating conditions, focusing on the Pt dissolution mechanism. The tasks were (1) measuring transport properties of a variety of membranes with different chemical and mechanical stability and (2) evaluating the membrane impact on BOT performance and catalyst layer durability.

2.3.1.1 Measurements of Membrane Transport Properties

Membrane transport properties such as water transport, changes in proton conductivity, and overall water uptake/adsorption can have an interaction effect on the state of the catalyst layer local conditions and catalyst layer degradation. Therefore, an understanding of the variation in membrane transport properties with different membrane types is essential. Figure 10 shows the interactions of the membrane component characteristics and membrane transport properties. The chart shows the flow path of the membrane component characteristics at the center of the chart (membrane type, density, thickness and EW) through to the membrane transport properties of protonic, gas, dissolved water and thermal energy transport, positioned at the outer edges. The flow chart demonstrates the complexity of these interactions, with the component characteristics and dissolved water concentration showing connections to multiple effective membrane transport properties. These transport properties, in turn interact with the local conditions of the catalyst layer to affect both MEA performance and durability.

The selection of membranes for this study includes the following membrane types: Nafion®211 (baseline membrane), Nafion®212, experimental reinforced PFSA membranes with low and high equivalent weights (EW), and reinforced partially fluorinated hydrocarbon membranes of high and low equivalent weights (EW).

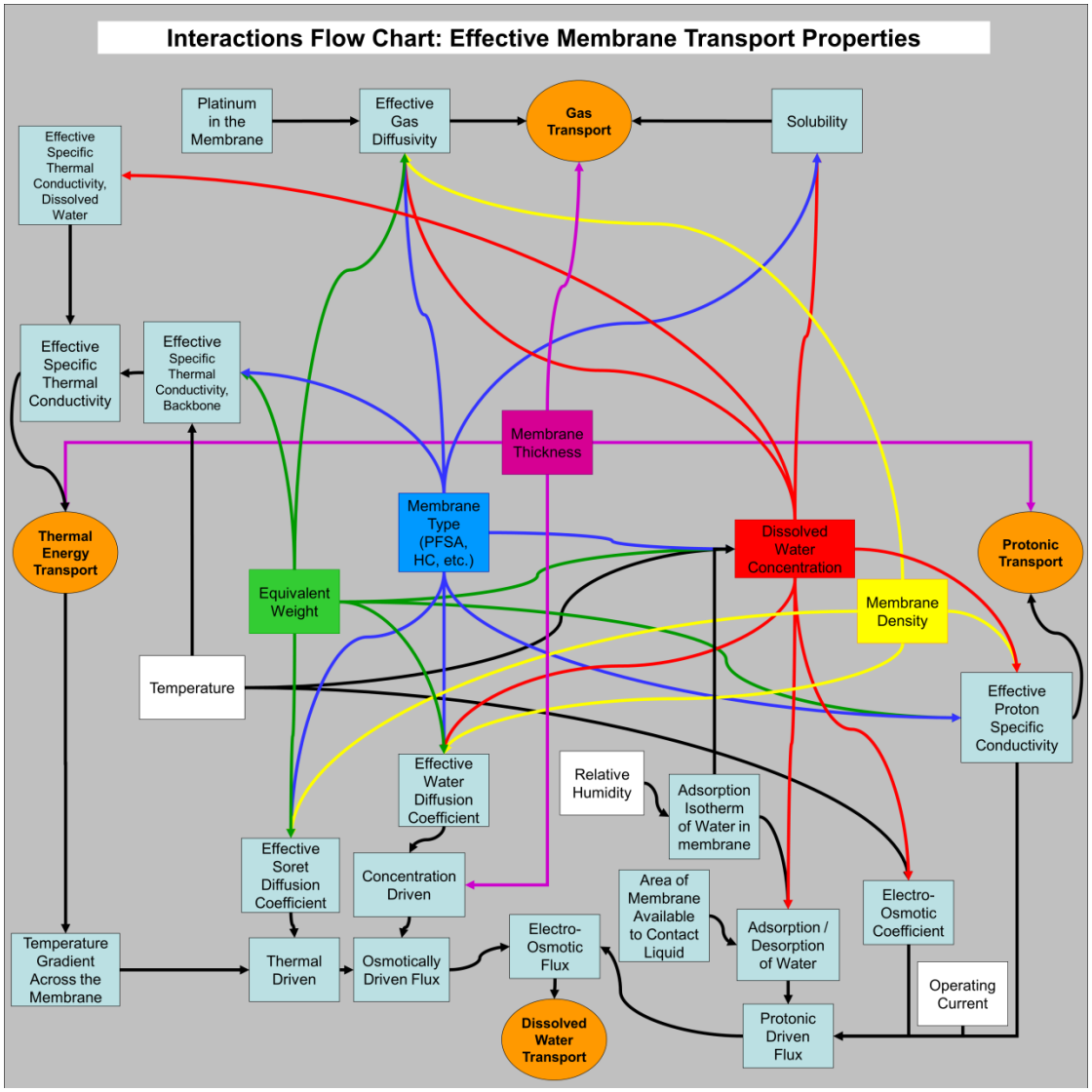

Figure 10: Interactions of membrane component characteristics and membrane transport properties.

Table 5 shows the membranes examined, their acronyms and some general characteristics. The dry densities of the membranes were similar, near 2 g/mL. The EW values ranged from ~ 600 to 1100 g/mol SA (sulfonic acid), while the dry thicknesses ranged from 13 to 50 microns. For the R-PFSA and R-HC membranes, the higher EW membrane was also thicker, so correlations of results to thickness effects would also have to consider EW effects and vice versa.

Table 5: Characteristics of Membranes Examined.

Membrane	Acronym Used	EW (g/mol SA)	Density (g/mL)	Dry Thickness (micron)
Baseline: Nafion NR211	NR211	1099	2.0	25
Nafion NR212	NR212	1099	2.0	50
Reinforced PFSA High EW	R-PFSA-HEW	1136	2.0	18
Reinforced PFSA Low EW	R-PFSA-LEW	872	2.0	14
Partially Fluorinated Hydrocarbon High EW	R-HC-HEW	758	1.8	15
Partially Fluorinated Hydrocarbon Low EW	R-HC-LEW	625	1.8	13

While a number of membrane properties were supplied by the manufacturers or taken from other sources, additional in-house collection of the membrane transport properties data were completed. Figure 11 compares the bare membrane water content (λ, lambda in mol H_2O / mol SO_3^-) as a function of humidity for a) R-PFSA manufacturer and literature[15] and b) collected in-house. These data show that lambda increases with RH as a Type II Isotherm behaviour, and that the R-PFSA membranes had a similar relationship as the NR211 membrane. R-HC membrane water uptake was not measured due to limited material availability. The in-house data, collected at 40°C (Figure 11b), is in agreement with the manufacturer and literature data at lower humidity levels. At $\geq$80%RH the water uptake values were lower than literature values and this may be related to the sample preparation or analysis conditions used. Since this testing activity was delayed due to equipment availability, time constraints did not permit a thorough development of the analysis method / conditions. Although the in-house water uptake results at $\geq$80%RH were lower than expected, relative trends between membranes are expected to be consistent and the results correlated well with other membrane properties measured in situ, as discussed further on.

Although, the R-PFSA and Nafion membranes had the same lambda vs RH relationship, the absolute water contents of the membranes were dependent on the EW. Figure 12 shows the absolute and normalized (lambda) water content as a function of EW for the Nafion and R-PFSA membranes. The absolute water content decreased with EW, while the lambda values did not show a strong relationship, as expected. The NR212 membrane did not fit the trend and had lower water content than expected.

[15] Luo, X.; Ghassemzadeh, L.; Holdcroft, S., Effect of free radical-induced degradation on water permeation through PFSA ionomer membranes. *International Journal of Hydrogen Energy* **2015,** *40* (46), 16714-16723.

Although the NR212 had lower water content than NR211, correlations of water content to other membrane transport properties were observed, as discussed further in the report.

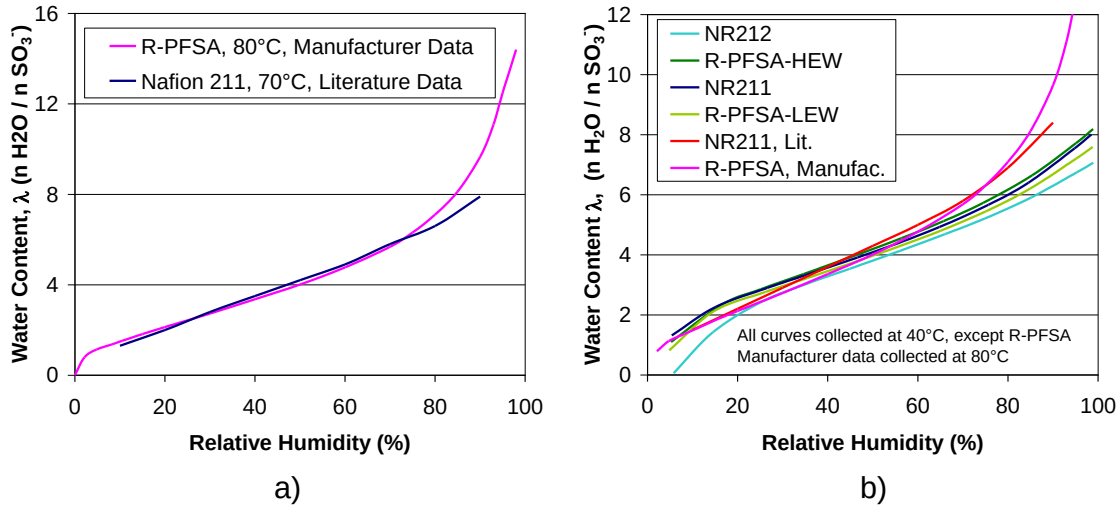

a) b)

Figure 11: Water content (lambda) as a function of relative humidity for Nafion and R-PFSA membranes, a) manufacturer and literature data[15] and b) in-house measurements.

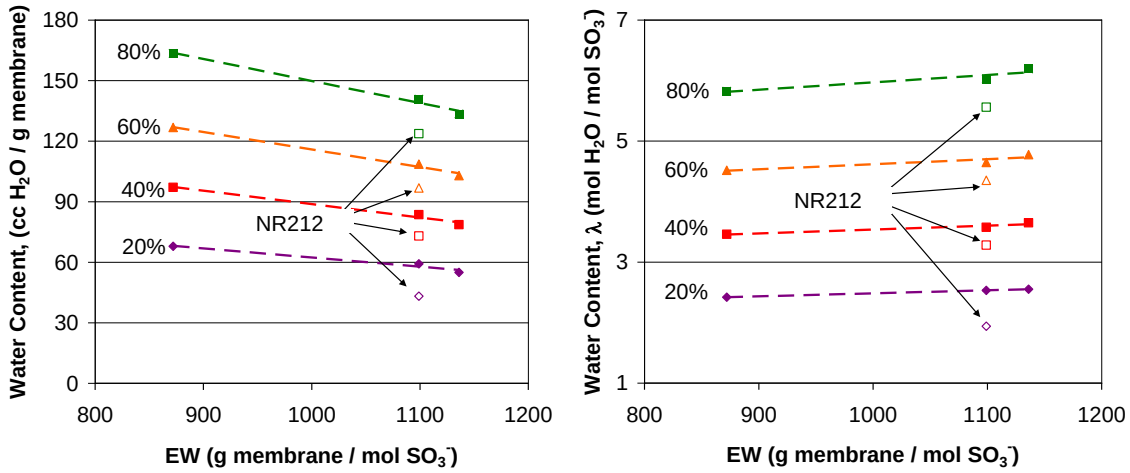

a) b)

Figure 12: a) Volumetric and b) Normalized (lambda) water content as a function of equivalent weight for bare membranes: NR211, NR212, R-PFSA-HEW and R-PFSA-LEW.

Figure 13 shows agreement of the through plane membrane resistance changes with RH for a) bare membranes determined by the manufacturer at 80°C and 95°C and b) in situ results collected in-house at 75°C. The through-pane resistance decreased with increased RH and temperature. The low EW membrane had lower resistance due to improved conductivity and decreased thickness. The calculated through-plane membrane conductivities, based on the conditioned membrane thickness, are shown as

a function of the RH in Figure 14a. These results also include any effects of the reinforcement layer and may not be a true measure of the ionomer conductivity. The R-PFSA-LEW has the highest conductivity followed by NR211, NR212, R-PFSA-HEW and the R-HC membranes. Comparing the calculated membrane conductivities with the water uptake measured for each RH, a linear correlation is observed, as shown in Figure 14b, and agrees with literature findings[16]. The R-PFSA membranes have slightly lower conductivity than the Nafion membranes for the same water content which may be due to the reinforcement layer.

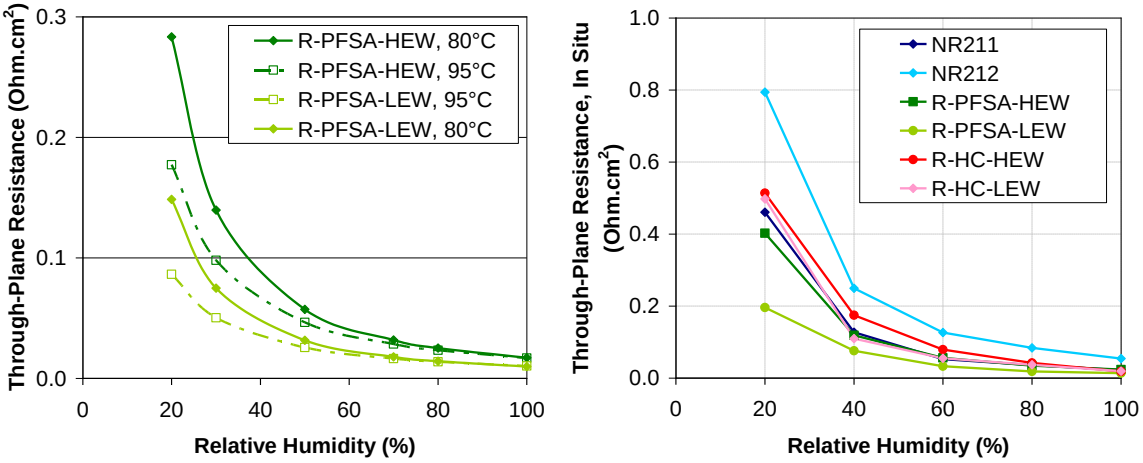

Figure 13: a) Through-plane membrane resistance as a function of RH by a) manufacturer, bare membrane at 80°C and 95°C and b) in-house, in situ MEA at 75°C measurements.

[16] Zawodzinski, T. A. Jr.; Derouin, C.; Radzinski, S.; Sherman, R. J.; Smith, V. T.; Springer, T. E.; Gottesfeld, S., Water Uptake by and Transport Through Nafion® 117 Membranes. *Journal of The Electrochemical Society* **1993,** *140* (4), 1041-1047.

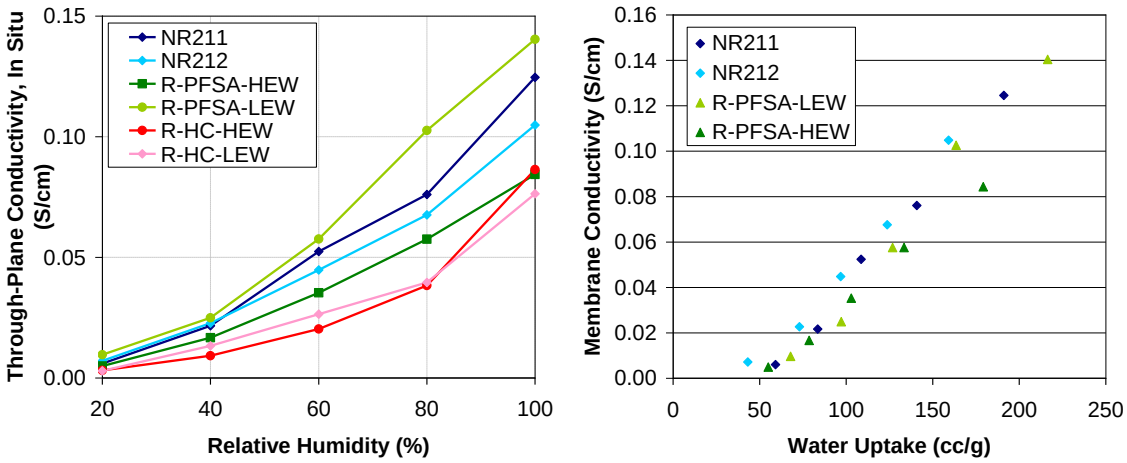

a) b)

Figure 14: In situ, through-plane membrane conductivity a) as a function of RH and b) correlated to bare membrane water uptake results for the corresponding RH.

Figure 15 compares the hydrogen permeance vs. RH relationship for a) R-PFSA bare membranes measured by the manufacturer at 90°C and 95°C and b) the in-house, in situ results for R-PFSA-LEW measured at 30°C, 75°C and 85°C. Hydrogen permeance increases linearly with relative humidity. The results for the R-PFSA membranes measured in the MEA in situ agreed well with the membrane data provided by the manufacturer, so additional membrane transport properties, such as hydrogen crossover, and resistance were measured for the MEA in situ, as part of the BOT / EOT diagnostics.

Figure 16 a) shows that the hydrogen permeability follows an Arrhenius relationship with temperature (R-PFSA-LEW results shown), while Figure 16b) shows the hydrogen permeance as a function of thickness for the 6 membranes tested. Each membrane family showed that the hydrogen permeance increased as thickness decreased, but the slopes were different for each family due to the different structures and/or transport mechanisms. After normalizing for thickness, the dependence of the hydrogen permeability on water uptake values is shown in Figure 17. Hydrogen permeability increased as membrane water content increased. The R-PFSA-LEW membrane showed a similar relationship as the Nafion membranes, while the R-PFSA-HEW hydrogen permeability was significantly lower. The difference between the two R-PFSA membranes after accounting for thickness and water uptake is consistent with the manufacture's data and suggests that other parameters are also affecting the hydrogen permeability.

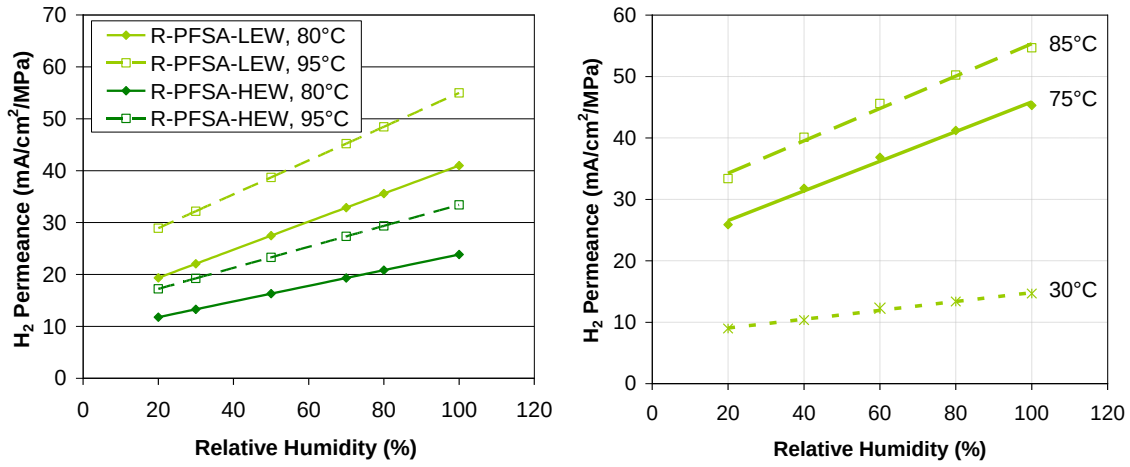

a) b)

Figure 15: Hydrogen permeance vs. RH for a) R-PFSA membranes (manufacturer data) and b) R-PFSA-LEW membrane measured in situ (in-house).

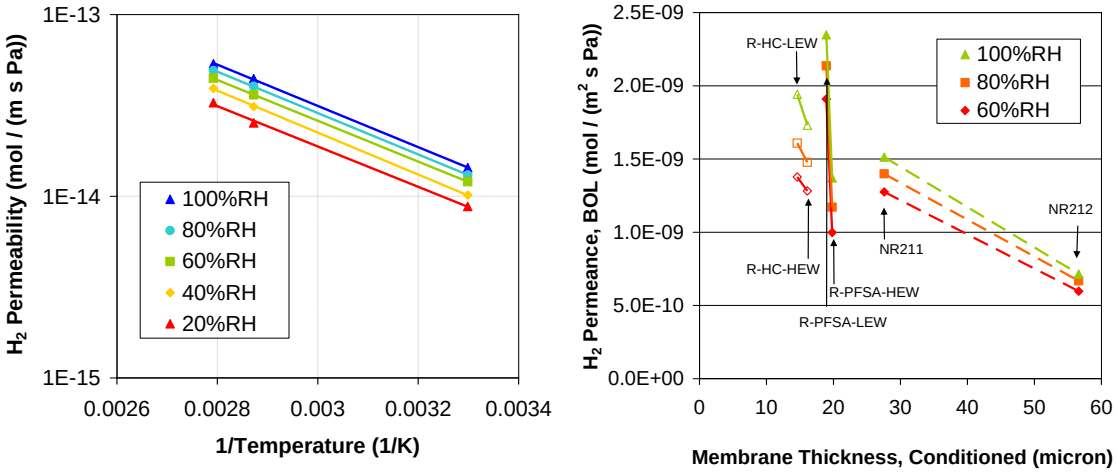

a) b)

Figure 16: a) Impact of temperature on in situ hydrogen permeability for R-PFSA-LEW membrane and b) hydrogen permeance as a function of membrane thickness for R-HC, R-PFSA and Nafion membranes.

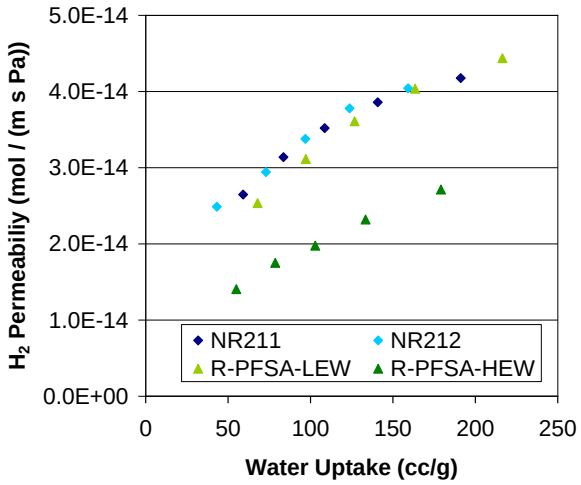

Figure 17: Impact of membrane water uptake on in situ hydrogen permeability.

Water crossover values were measured in situ by determining the amount of water in the fuel and oxidant exhaust streams and after taking into account inlet humidification and product water, calculating the net movement of water from anode to cathode. Measurements were taken at different current densities for a range of humidity levels, including drier cathode / wetter anode conditions and vice versa. Net water crossover towards the cathode is reported as positive water crossover, while net water crossover toward the anode is reported as negative values. Figure 18 shows that water crossover increases as fuel RH is increased or air RH is decreased. Increasing current density resulted in increased water crossover to the cathode, as shown in Figure 19a). It was found that more water stays on the cathode for thicker membranes regardless of the inlet humidity levels, as shown in Figure 19b).

Water crossover processes occurring in the MEA include pressure driven hydraulic permeation, diffusion and electro-osmotic drag. The dependence of water crossover on membrane thickness suggests that diffusion from cathode to anode is an important contributing factor and agrees with literature findings[17, 18]. Thicker membranes reduce the amount of water crossover due to diffusion, and result in a higher overall water crossover than for thinner membranes. The larger spread in water crossover values for the thinner membranes at the different RH combinations is also related to their higher amounts of diffusion. Analogous to the hydrogen crossover results, the R-HC and R-PFSA families showed larger variations in water crossover than expected due to

[17] Ibid.
[18] Dai, W.; Wang, H.; Yuan, X.; Martin, J. J.; Yang, D.; Qiao, J.; Ma, J., A Review on Water Balance in the Membrane Electrode Assembly of Proton Exchange Membrane Fuel Cells. *International Journal of Hydrogen Energy* **2009,** *34* (23), 9461-9478.

thickness effects, suggesting that the membrane water transport properties are influenced by the differences in structure and/or chemistry.

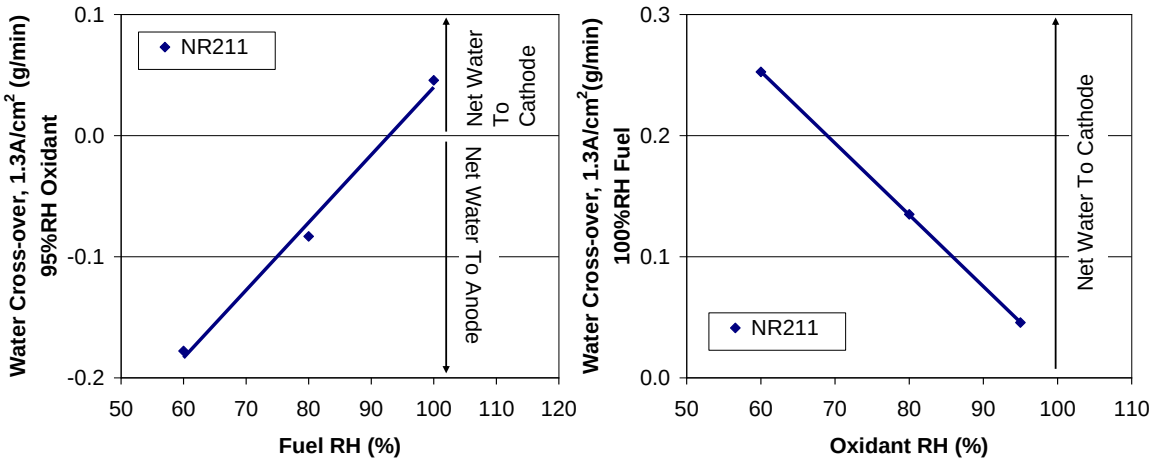

Figure 18: Effect of a) fuel RH and b) air RH on in situ water crossover rate for NR211.

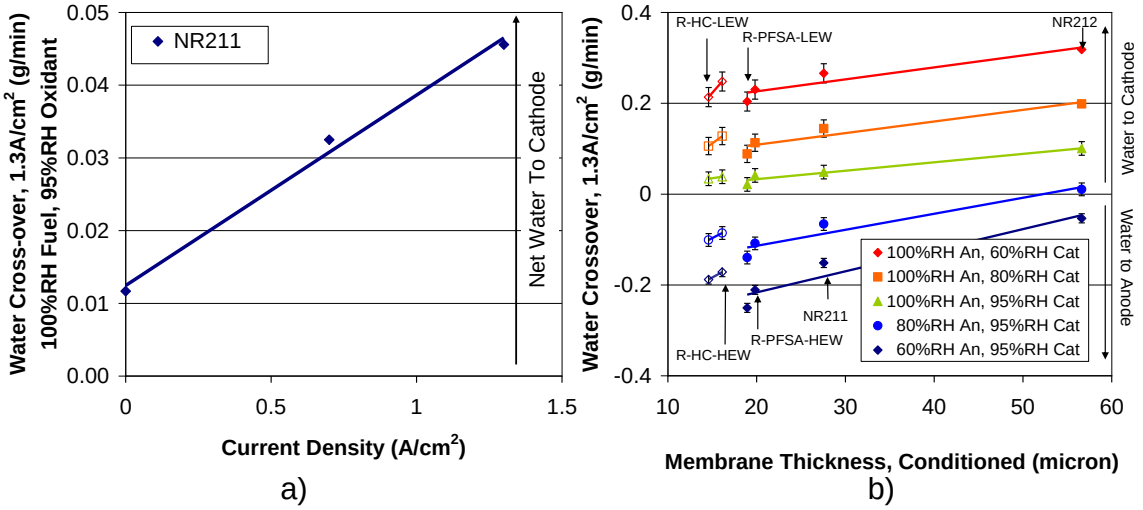

Figure 19: a) Effect of current on water crossover rate for NR211and b) in situ water crossover rates as a function of membrane thickness for R-HC, R-PFSA and Nafion membranes.

Table 6: Membrane Transport Properties.

Membrane	Water uptake, 80%RH (cc/g)	Through-plane Conductivity*, 80%RH (S/cm)	Hydrogen Permeance, 100%RH (mol / m^2 s Pa)	Water Crossover, 1.3A/cm^2, 60%RH Fuel, 95% RH Ox (g/min)
NR211	141	0.064	1.5×10^{-9}	-0.15
NR212	124	0.069	7.1×10^{-10}	-0.05
R-PFSA-HEW	133	0.046	1.4×10^{-9}	-0.21
R-PFSA-LEW	163	0.064	2.3×10^{-9}	-0.25
R-HC-HEW	N/A	0.030	1.8×10^{-9}	-017
R-HC-LEW	N/A	0.031	1.9×10^{-9}	-0.19

* Through-plane conductivity values include reinforcement effects for the reinforced membranes.

In summary, membrane water uptake increased with RH, and membranes of different EW had similar lambda values. Membrane conductivity and hydrogen permeability also increase with RH and correlated well with the membrane water uptake values. Water crossover is affected by RH gradients, with water crossover increasing as the RH gradient is increased. Water crossover increases with current production due to electro-osmotic drag and variations in water crossover with different membranes at the same current density were found to be correlated to thickness due to diffusion effects. Additional parameters such as membrane structure, chemistry or transport mechanisms may also affect the transport properties.

2.3.1.2 Effect of Membrane Type/Properties on Cell Performance and Durability

MEAs containing the six different membrane types were tested for performance and durability. The CCMs were prepared by applying the same cathode and anode catalyst inks using the different membranes. The baseline MEA, the test hardware, the cathode AST, and suite of diagnostic tools are those described in section 1.2.

The average BOT performance results and voltage loss breakdowns for the six different membranes are shown in Figure 20 and Figure 21. In general, the R-PFSA membranes showed the best performance, followed by the Nafion membranes and lastly, the R-HC membranes which had the lowest performance. The poorer performance of the R-HC membranes was likely impacted by catalyst layer / membrane interface resistance due to dissimilar ionomers, causing higher kinetic and CL ionic losses, while the better performance of the R-PFSA membranes is related to the lower CL ionic losses

observed (Figure 21). The NR212 membrane showed lower performance than the thinner NR211 membrane due to the increased resistance and ohmic losses related to the increased membrane thickness. Similarly, R-PFSA-HEW had lower performance than the R-PFSA-LEW membrane due to the increased resistance and ohmic losses related to the increased EW and thickness effects. In contrast, the R-HC-LEW membrane had lower performance than the R-HC-HEW membrane, but the results for these experimental materials are not considered to be representative, as the R-HC membranes showed irregularities in the membrane consistency by SEM imaging, and had stability issues during the testing.

At low humidity (60% RH) the performance sensitivity increased with membrane equivalent weight and/or membrane thickness. For each membrane family the thicker and/or higher EW membrane had lower performance or more sensitivity to lower humidity. The RH performance sensitivities agree with the membrane resistance changes with RH given in Figure 13b, which showed that the NR212 membrane had the highest resistance at low RH, followed by the R-HC membrane, NR211 and then the R-PFSA-HEW and R-PFSA-LEW membranes.

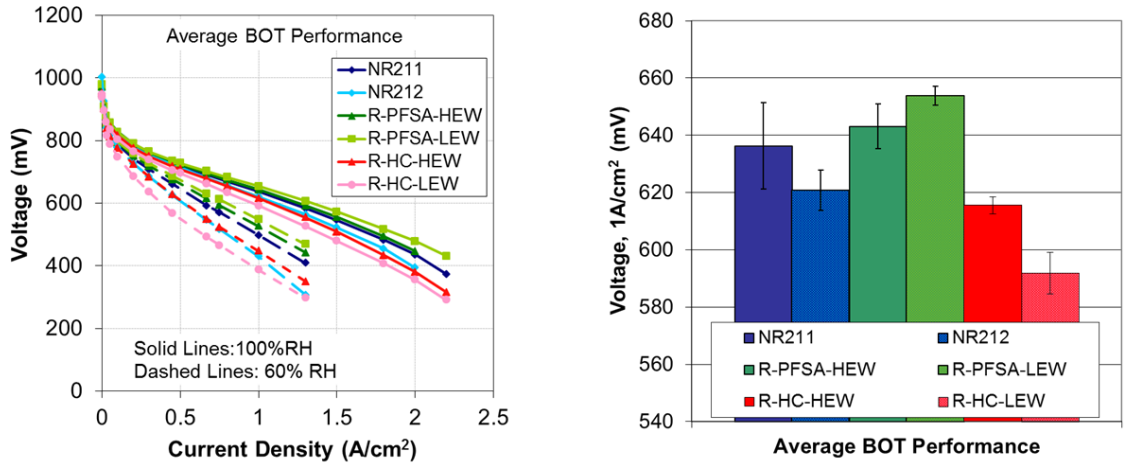

Figure 20: a) Average BOT performance at 100%RH and 60%RH and b) Average BOT performance at 100%RH and 1A/cm^2 of MEAs with different membranes.

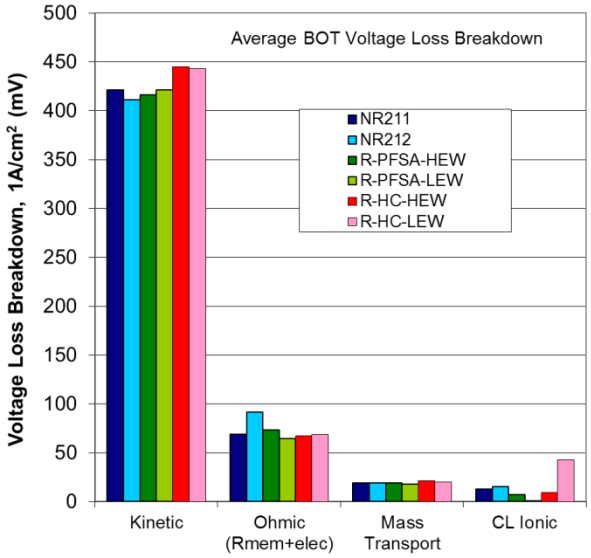

Figure 21: Voltage loss break down at BOT at 1A/cm^2 and 100%RH.

After the MEAs were subjected to the cathode AST for 4700 cycles, ECSA and performance losses occurred (Figure 22 and Table 7). Although the performance losses were not as large, in general they followed the same trend as the ECSA losses. The polarization curves at EOT in (Figure 23) show that the spread in performance between membranes decreased in comparison to BOT (except the R-HC LEW), as the higher performing MEAs had greater performance degradation. The R-HC-LEW had exceptionally high degradation and cell resistance. The voltage loss breakdown in Figure 21 shows a large increase in the ohmic loss suggesting that there was membrane degradation causing a loss of membrane conductivity. Membrane degradation was confirmed by EOT membrane thickness measurements revealing 50% thinning had occurred. In contrast, the voltage loss breakdown in Figure 23 shows that the performance loss of the other MEAs was mostly due to increased CL Ionic losses, which is typical of cathode AST degradation.

Table 7: ECSA Loss and Performance Loss after 4700 Cathode AST cycles.

Membrane Type	EOT ECSA Loss (%)	BOT Performance, 1A/cm^2, 100%RH (mV)	EOT Performance Loss, 1A/cm^2, 100%RH (mV)
NR211	64	658	48
NR212	57	613	54
R-PFSA-HEW	50	636	34
R-PFSA-LEW	58	657	58
R-HC-HEW	62	613	60
R-HC-LEW*	81	597	239

*showed signs of membrane degradation during Cathode AST testing

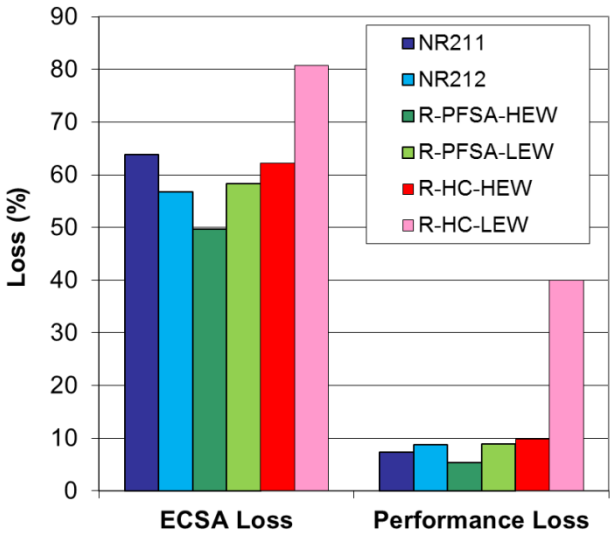

Figure 22: Relative ECSA and Performance Losses after 4700 AST cycles.

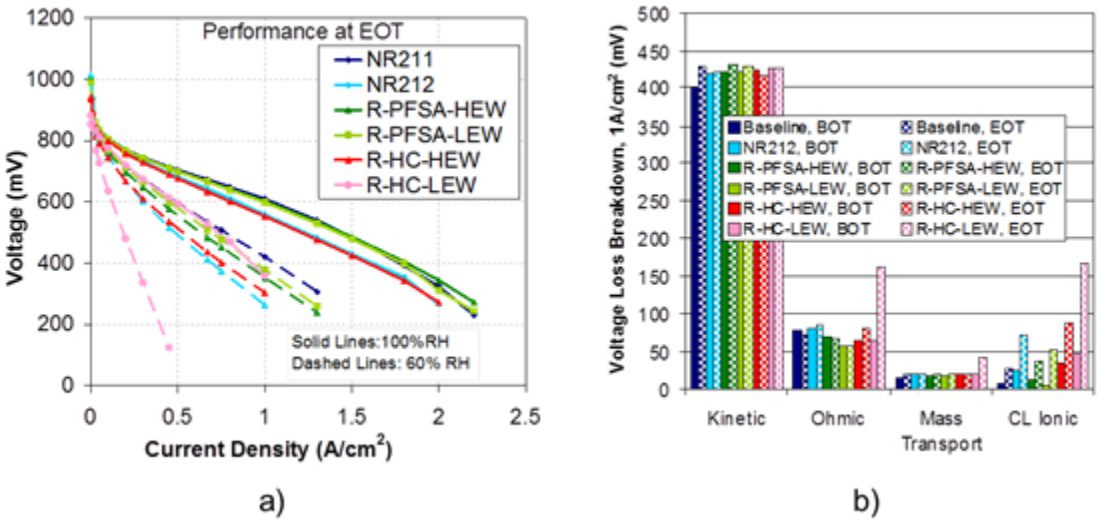

Figure 23: a) Performance at EOT (4700 AST cycles) and b) voltage loss breakdown at BOT and EOT at 1A/cm^2 and 100%RH of MEAs with different membranes.

In addition to the operating conditions, membrane characteristics and transport properties, such as diffusion, electro-osmotic and pressure driven water crossover, water uptake, and hydrogen crossover, may impact degradation by affecting the local conditions of the catalyst layer. For example, higher catalyst layer water content is

expected to cause more degradation, given that previous operational studies[19,20] have shown that platinum dissolution degradation was found to increase with inlet RH. In addition, a study[21] on the effect of fuel hydrogen concentration on catalyst degradation for NR211 has shown that increased hydrogen crossover can hinder the platinum dissolution mechanism by reducing Pt oxides and subsequently decreasing the amount of Pt ions formed via the oxide pathway and leading to lower platinum agglomeration.

Since many of the membrane characteristics and properties vary together, no one characteristic can be separated as the main cause for the different degradation rates. The ECSA losses were found to decrease with membrane thickness for each membrane family, as shown in Figure 24, although the slopes were not similar. Even though the Nafion membranes were a true thickness comparison, several other parameters such as resistance and crossover rates also varied with thickness. The R-PFSA membranes showed a large change in degradation rate, although the variation in thickness was small. Therefore, the changes are most likely due to effects other than membrane thickness. The experimental R-HC membranes showed the highest and greatest variation in degradation rate. In addition to an EW effect, the observed membrane degradation for the R-HC-LEW membrane may have resulted in greater ECSA loss and therefore the results may not be consistent. It is believed that multiple factors are responsible for the changes in degradation rates.

It was observed that the NR211 test had higher PITM (16% Pt loss) than the NR212 test (7% Pt loss), while the agglomeration or Pt size was similar (7.5nm and 7.8nm, respectively). The larger membrane thickness of the NR212 membrane results in a larger distance to the PITM band and therefore a lower platinum migration flux into the membrane compared to NR211. In addition, the slower removal of dissolved platinum species at the catalyst surface may decrease the overall platinum dissolution rate as well. Although PITM was not quantified for the reinforced membranes, as membrane suppliers did not allow for chemical analysis of the membrane material, Pt band position and Pt migration rates are not expected to explain the different degradation rates for the R-PFSA membranes, as the thicknesses only varied slightly and the SEM images did not show an obvious difference in PITM band intensity, as seen for the Nafion membranes.

The resulting MEA performance variations of the different membranes also played a role in the degradation rates. Figure 25 shows the ECSA losses for the Nafion and R-PFSA membranes as a function of the current density at 0.6V, or the lower potential limit hold at the start of the cathode AST. The MEAs with the higher current density, and

---

[19] Bi, W.; Sun, Q.; Deng, Y.; Fuller, T. F., The effect of humidity and oxygen partial pressure on degradation of Pt/C catalyst in PEM fuel cell. *Electrochimica Acta* **2009,** *54* (6), 1826–1833.
[20] Xu, H.; Kunz, R.; and Fenton, J. M.; Investigation of Platinum Oxidation in PEM Fuel Cells at Various Relative Humidities. *Electrochemical and Solid-State Letters* **2009,** *10* (1), B1-B5.
[21] Cheng, T. T. H.; Rogers, E.; Young, A. P.; Ye, S.; Colbow, V.; Wessel, S., Effects of crossover hydrogen on platinum dissolution and agglomeration. *Journal of Power Sources* **2011**, 196 (19), 7985-7988.

therefore more product water as well as crossover water, showed the higher ECSA degradation, which is consistent with the hypothesis of greater water content leading to greater Pt dissolution. In comparison, previous air vs. nitrogen oxidant AST studies showed that air operation (with water production during the 0.6V LPL phase) showed 10% more ECSA loss than the nitrogen test where no water was produced[22]. However, the air vs nitrogen comparison testing had less relative time at 0.6V than the present study, so water production effects may not have been as prominent. Since the air vs nitrogen differences were similar in value to the ECSA loss improvements within the membrane families, where a much smaller product water effect occurs, this hypothesis may only partially explain the degradation improvements within the membrane families.

The Nafion and R-PFSA membranes show similar slopes but different magnitudes of ECSA loss, with Nafion showing higher degradation at comparable current density. The overall lower degradation of the R-PFSA membranes may be related to thinner membranes with less water crossover (to the anode) at similar current density.

Since the current density and water production at 0.6 V only partially explain the variation in degradation rates for the R-PFSA membranes, the EW differences may also be a factor. It is hypothesized that the lower EW, resulting in higher absolute water content in the membrane, can lead to slightly higher local catalyst layer water content at the membrane/catalyst interface where Pt dissolution is the greatest. This may cause a higher ECSA loss.

Table 8: Summary of hypotheses relating membrane properties to cathode degradation.

Hypothesis		Supporting / Non-supporting information
Increased CL water content increases degradation	Higher current density during 0.6V hold increases product water and crossover water leading to higher degradation (Decreased membrane resistance due to higher conductivity, lower EW and or thinner membrane thickness, increases performance and current density at 0.6V hold)	• Nafion and R-PFSA membrane families show increased ECSA loss with higher performance • Air vs nitrogen tests show less sensitivity to water production than observed for the membrane studies, but the AST cycle parameters were different with less relative time held at the LPL
	Increased water crossover leads to higher cathode	• NR211 and R-PFSA-LEW, which had the same current

[22] M. Dutta, N. Jia, V. Colbow, G. Faubert and S. Wessel “Effects of Accelerated Stress Test Oxidant Gas on PEM Fuel Cell Cathode Degradation” 4th Annual Fuel Cells Durability & Performance **2008** in Las Vegas, NV (Dec. 11-12, 2008).

	water content and higher degradation	density at 0.6V, showed higher degradation for the thicker Nafion membrane which had higher water crossover
	Increased membrane EW leads to a lower absolute water content of the membrane and may give lower catalyst layer water content, especially at the membrane / catalyst interface where Pt dissolution is the strongest, leading to lower degradation	• R-PFSA-HEW had lower ECSA loss than R-PFSA-LEW
Increased hydrogen crossover decreases degradation	Hydrogen crossover can hinder the platinum dissolution mechanism by reducing Pt oxides and subsequently decreasing the amount of Pt ions formed via the oxide pathway and leading to lower platinum agglomeration	• Previous study[23] on the effect of fuel hydrogen concentration supports this hypothesis • Effect was not clearly observed in the membrane study, as other parameters may have a stronger effect
Increased membrane thickness decreases degradation due to PITM band position	Increased membrane thickness results in a further PITM band position from the cathode which reduces the Pt migration flux and therefore degradation	• NR211 had more PITM and a closer band position than NR212. NR211 had more ECSA loss than NR212

All in all, there are several hypothesized effects which may help explain the ECSA degradation rates observed (Table 8). The membranes with lower resistance due to thickness and EW effects result in better performance and higher water production, as well as water crossover during the 0.6V lower potential hold. This leads to higher degradation for the thinner or lower EW membranes of each family. In addition, for the Nafion membranes, the further PITM band position for the thicker NR212 membrane resulted in lower Pt migration flux and overall ECSA loss. The R-PFSA-LEW membrane may have additional ECSA losses, in comparison to the HEW membrane due to water content effects. For MEAs showing the same amount of water production at 0.6V, the

[23] Cheng, et al, Effects of crossover hydrogen (see footnote 21).

thinner membrane (i.e. R-PFSA vs Nafion) has less net water crossover and therefore less degradation.

In summary, performance variations at BOT may be due to a combination of membrane characteristics and transport effects. Ohmic losses were due to membrane resistance related to the membrane thickness and conductivity, while other losses may have varied due to membrane transport properties and reaction distribution. The ECSA degradation was found to be impacted by a combination of factors, including thickness, water production, water crossover and water content.

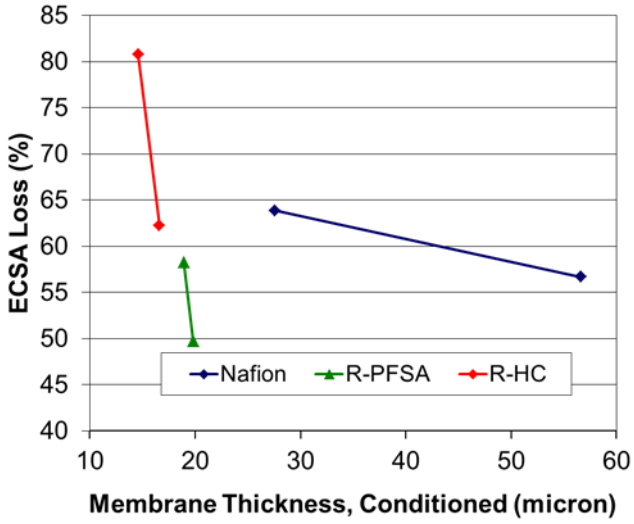

Figure 24: ECSA loss after 4700 cathode AST cycles vs membrane thickness for R-PFSA and Nafion Membranes.

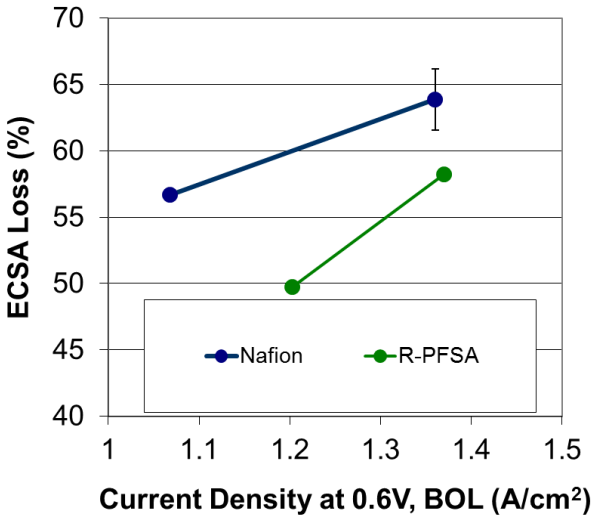

Figure 25: ECSA loss after 4700 cathode AST cycles vs BOT current density at 0.6V (lower potential limit of AST) for R-PFSA and Nafion Membranes.

2.3.2 Impact of Membrane Degradation on the Pt Dissolution Mechanism

The objective of this task was to investigate the impact of membrane degradation on catalyst layer durability, focusing on the effect of changes in water transport properties after the MEAs were subjected to the membrane AST.

2.3.2.1 Membrane Down-selection for Membrane Degradation Experiments

Three membranes, NR211, NR212 and reinforced PFSA Low EW, were down-selected for the study of membrane degradation impact on the platinum dissolution mechanism.

The MEAs were first subjected to a modified membrane OCV AST of 3 cycles, which included a chemical degradation phase at OCV under hot and dry conditions and diagnostic tests. The planned wet / dry cycling phase was eliminated to prevent mechanical degradation and pinhole formation. Three to five cell stacks of each membrane type were subjected to the membrane AST and then were followed by single cell testing for performance diagnostics and cathode degradation testing.

Membrane and MEA property changes after OCV degradation are given in Table 9. The NR211 and R-PFSA Low EW membranes showed 3-4 micron membrane thinning while the NR212 membrane showed over 20 micron membrane thinning and also developed leaks during the cathode AST. The thinning rates showed a trend with the BOT OCV values for the three membranes, although other structural parameters may also have played a role in the high degradation rate for NR212.

The higher degradation rate for NR212 also resulted in greater changes to the membrane transport properties listed in Table 9, such as decreased resistance and conductivity and increased H_2 permeability. Similar changes to the resistance and conductivity were also observed for the other membranes, but to a lesser degree. In addition to the membrane property changes, ECSA loss was also observed for all three membranes, although the Pt size was constant after the membrane AST for all three membranes. The platinum content of the cathode catalyst layers had also decreased and is hypothesized to have washed out towards the GDL, as no PITM was observed. Although only 3 potential cycles occurred during the OCV test, the long hold at OCV is presumed to result in a large formation of sub-surface oxide, and lead to Pt dissolution. Although ECSA was lost, the Pt size was not affected and therefore it is hypothesized that the remaining Pt nanoparticles did not undergo any stabilization during the OCV AST that would affect the subsequent cathode AST results.

Table 9: Membrane and MEA property changes after three membrane OCV AST cycles.

Membrane	NR211	NR212	R-PFSA-LEW
Thickness, BOT (µm)	27.6	56.6	18.9
Thickness, EOT (µm)	24.7	35.3	14.9
Thickness Loss (%)	10	38	21
Resistance Loss (%)	1	26	17
Conductivity Loss (%)	9	16	6
H_2 Permeability, BOT (mol / m / s / Pa)	4.2×10^{-14}	4.0×10^{-14}	4.4×10^{-14}
H_2 Permeability, EOT (mol / m / s / Pa)	4.3×10^{-14}	2.2×10^{-13}	3.5×10^{-14}
OCV (mV)	966	983	974
ECSA Loss (%)	19	20	27

Membrane resistances before and after OCV testing for a range of humidity levels are shown in Figure 26. At saturated conditions of 120% RH, the degraded membranes fall on the same resistance vs. membrane thickness relationship as the BOT membrane. While the degraded membranes did show a drop in resistance due to the thinning, the voltage drop was smaller than expected due to a decrease in the membrane conductivity. At under-saturated conditions, the degraded membranes showed a much higher resistance vs. membrane thickness relationship than the BOT membranes. The membrane conductivities over the range of humidity levels studied given in Figure 27 show that, in general, the conductivity losses with OCV degradation are greater for drier conditions. The changes in conductivity with degradation suggest loss of sulfonic acid groups, ionic conductivity/connectivity and/or water uptake occurring.

Water uptake measurements after OCV degradation were not performed as the membrane could not be removed from the catalyst layers for the measurement. In addition, water crossover after OCV degradation could not be measured, as the testing involved repeated operation at wet and then dry conditions which resulted in undesirable wet / dry cycles leading to mechanical stresses and membrane transfers. Consequently, undersaturated diagnostic protocols were eliminated in all subsequent testing of membrane degraded MEAs to avoid any inadvertent wet / dry cycling.

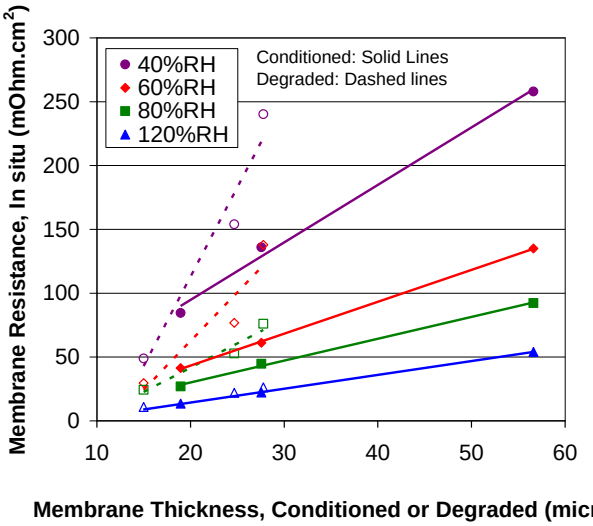

Figure 26: Membrane resistance vs. membrane thickness for conditioned and OCV AST degraded membranes.

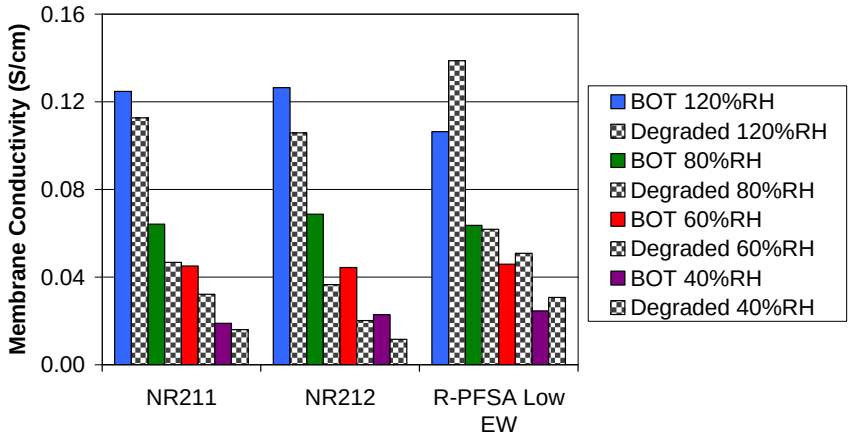

Figure 27: Membrane conductivities for conditioned and OCV degraded membranes.

In summary, membrane degradation at OCV led to membrane thinning, lower membrane conductivity and ECSA, minimal platinum agglomeration, and higher hydrogen crossover.

2.3.2.2 Impact of Membrane Degradation on Performance

The effect of membrane degradation on MEA performance is shown by the polarization curves in Figure 28. All MEAs showed performance loss with membrane degradation. At 100%RH the performance drop was greatest for NR211, followed by NR212 and then R-PFSA LEW. At 60% RH, both the NR211 and R-PFSA had a larger change with membrane degradation, while NR212 showed a small decrease in performance.

The changes in performance can be explained by the voltage loss breakdowns at 100%RH in Figure 29. Although the membranes thinned and showed loss of conductivity, the ohmic losses observed for NR211 and R-PFSA-LEW were minimal, as the thickness losses balanced the conductivity losses and the overall resistance observed was similar for both BOT and EOT at 100%RH. NR212 showed an ohmic improvement or lower resistance after membrane degradation, as the membrane thinning of 38% more than offset the 16% loss of conductivity.

The CL ionic losses were the most affected by membrane degradation (Figure 29). The NR211 and R-PFSA LEW membranes had 3-4 micron thinning, 6-10% conductivity loss and CL Ionic loss increases of ~40%. The absolute increase of the CL ionic losses for NR211 was larger than for the R-PFSA LEW. The NR212 membrane was degraded by the largest amount (38% membrane thinning, 16% conductivity loss) and also showed the highest increase (>300%) to the CL ionic losses. Since the NR212 saw improved membrane resistance due to the thinning, the overall performance loss for the NR212 membrane was smaller than for NR211. In addition to the CL ionic loss degradation, increases to the CL ionomer resistance, measured by EIS, were observed. CL ionomer resistance changes may be due to CL ionomer degradation or membrane / CL interface degradation, but these changes do not account for the entire amount of increased CL ionic losses. It is suspected that membrane degradation by-products, such as hydrophilic side chain fragments may be present in the catalyst layer resulting in reaction distribution shifts further into the catalyst layer due to oxygen mass transfer effects and increased CL ionic losses.

After membrane degradation the NR211 and R-PFSA-LEW membranes showed greater sensitivity to 60%RH operation than 100% operation due to ohmic and CL ionic resistive losses increasing under drier conditions. The NR212 degraded membrane did not show as much sensitivity to dry 60% RH as the other membranes due to the ohmic loss improvement caused by the reduced thickness counteracting CL ionic losses.

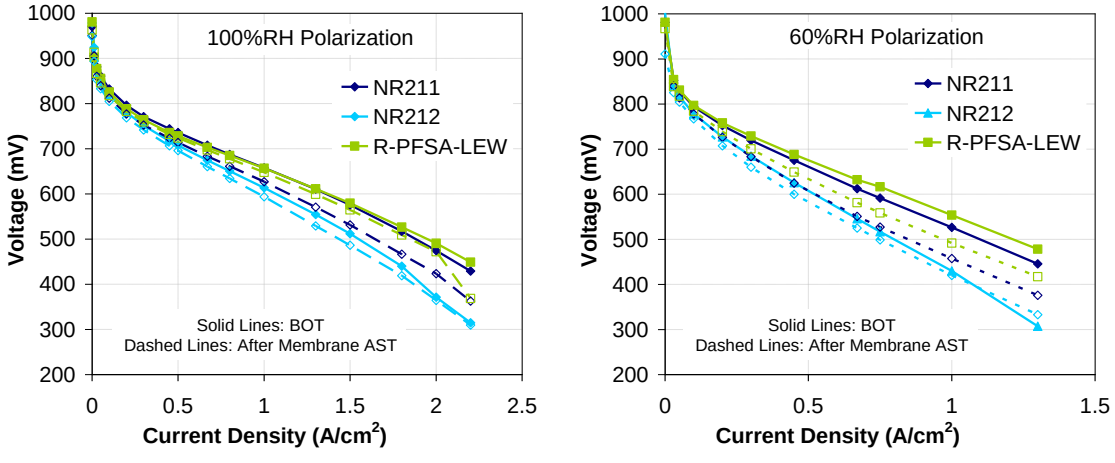

a) b)

Figure 28: Polarization curves before (solid lines) and after membrane AST (dashed lines) at a) 100%RH and b) 60% RH.

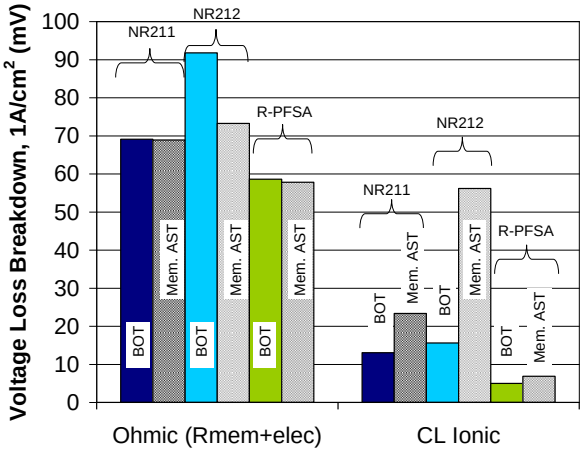

Figure 29: Ohmic and CL ionic losses before and after membrane AST at 1A/cm^2 and 100%RH.

In summary, membrane degradation, leading to membrane thinning and conductivity losses, decreases the performance due to ohmic and CL ionic losses. Since membrane thinning and conductivity losses have opposite effects on resistance, the overall ohmic losses were similar or even improved. The CL ionic loss changes were found to be an important factor in the performance loss and were due to a combination of CL ionomer resistance increases related to membrane and/or CL ionomer degradation and reaction distribution shifts related to membrane degradation by-product contamination of the catalyst layer.

2.3.2.3 Impact of Membrane Degradation on the Pt Dissolution Mechanism

After three membrane AST cycles, the MEAs were stressed by the cathode AST. The ECSA and ECSA loss vs. AST cycles are shown in Figure 30. All three membranes started and ended the cathode AST with a lower ECSA than the fresh MEA cathode AST tests. As discussed above, ECSA loss was observed after the membrane AST, so the ECSA loss for membrane degraded samples was normalized to the ECSA at the start of the cathode AST rather than the fresh MEA, to allow for a consistent comparison of effect of number of cathode AST cycles. Air performance losses were also normalized in a similar manner. The results show that the OCV degraded NR211 and R-PFSA membranes had lower ECSA losses after cathode AST cycling than the pristine samples. The NR212 showed similar results up to 700 cycles, but then had much higher ECSA losses for the degraded membrane. This membrane showed signs of pinhole formation, which may have convoluted the cathode AST. A repeat of the NR212 test to a lesser degree of membrane degradation was done and will be discussed in a subsequent section.

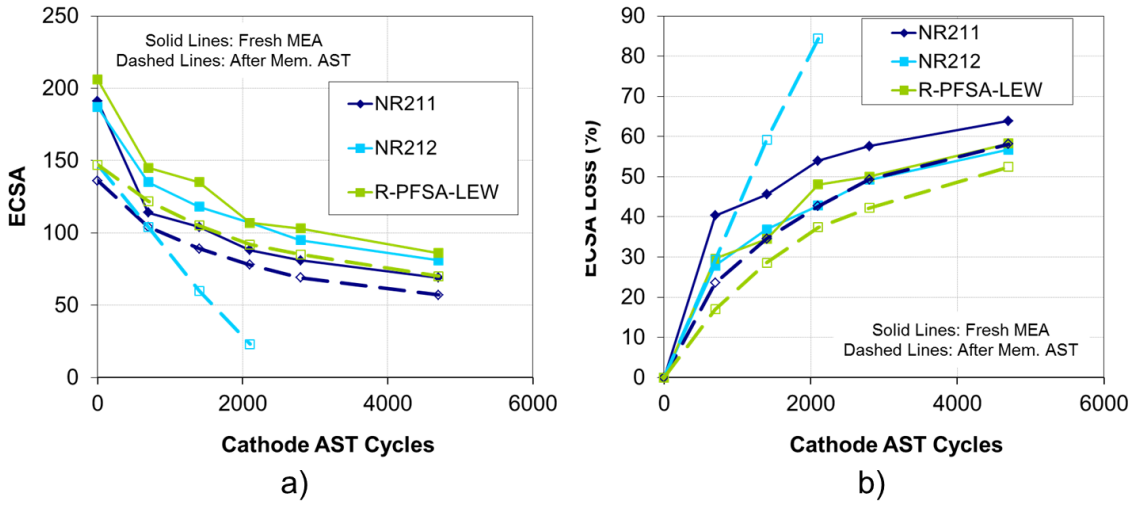

Figure 30: a) ECSA and b) ECSA loss vs. cathode AST cycles for fresh (solid lines) and degraded (dashed lines) membranes.

Failure analysis of the membranes was done to quantify the platinum dissolution mechanism. Figure 31 compares the Pt size and amount of platinum in the membrane (PITM) for MEAs after conditioning, after membrane AST, after cathode AST and after both membrane and cathode AST. The results show that the Pt size did not grow and no PITM occurred with membrane AST. After membrane and cathode AST, the Pt size was slightly higher and the PITM was much lower than that for the cathode AST alone, suggesting that the platinum migration into the membrane was hindered by pre-existing membrane degradation. For NR211, the decrease in PITM with membrane degradation matched well to the increase in Pt size from Pt agglomeration. For the NR212, the larger Pt size did not account for the lower amount of PITM and additional Pt washout occurred with the pre-existing membrane degradation.

Figure 32 shows the SEM images for NR211 and NR212 after cathode AST and after OCV plus cathode AST. Comparing the membrane & cathode AST images in Figure 32 c) and d) with the respective cathode AST images in Figure 32 a) and b) the membrane thickness loss and decrease in the intensity of the platinum band for the membrane degraded samples can be observed. The lower PITM for membrane degraded samples is similar to the catalyst layer Nafion ionomer loading study from the previous project[24], where it was found that lower Nafion content MEAs had less PITM and slightly higher agglomeration with cathode AST. The hypothesis for the fresh samples was that the lower CL ionomer content provided fewer pathways for platinum migration. In the present membrane degradation study, there may also be a decrease in pathways for

[24] Wessel, Silvia, and David Harvey. *Final Project Report: Development of Micro-Structural Mitigation Strategies for PEM Fuel Cells: Morphological Simulations and Experimental Approaches*. United States: N. p., 2013. Web. doi:10.2172/1087665.

platinum migration as a result of the degradation of the membrane, which also showed a loss of proton conductivity. Another possible cause may be lower water content/transport of the degraded membrane slowing platinum migration rates.

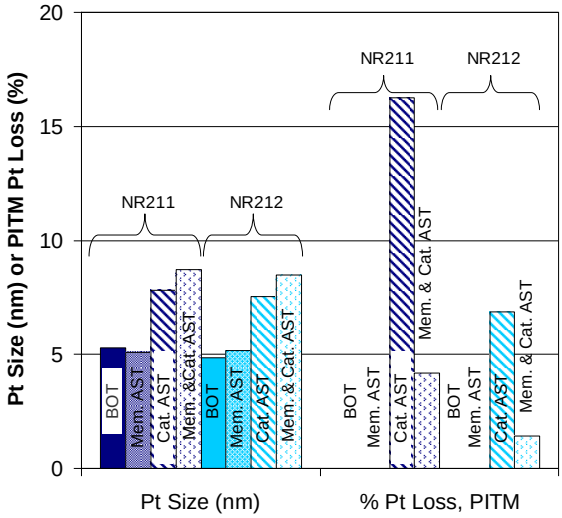

Figure 31: Pt Size and PITM, expressed as a percentage of Pt lost from the BOT cathode, after membrane AST, after cathode AST and after both membrane and cathode ASTs for NR211 (baseline NR211) and NR212.

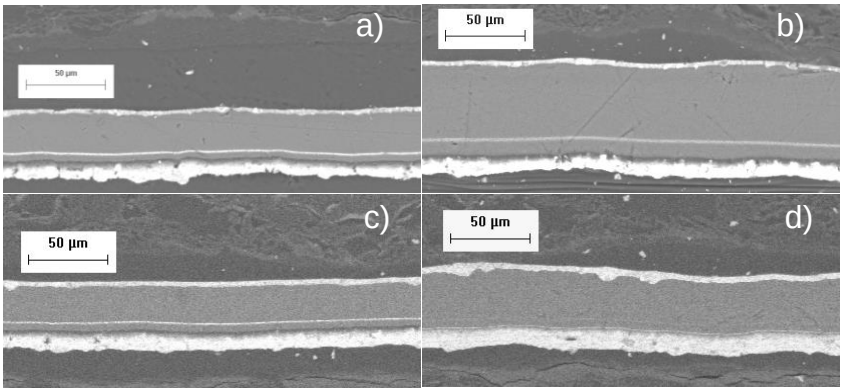

Figure 32: SEM images a) NR211 after cathode AST b) NR212 after cathode AST c) NR211 after OCV and cathode AST and d) NR212 after OCV and cathode AST.

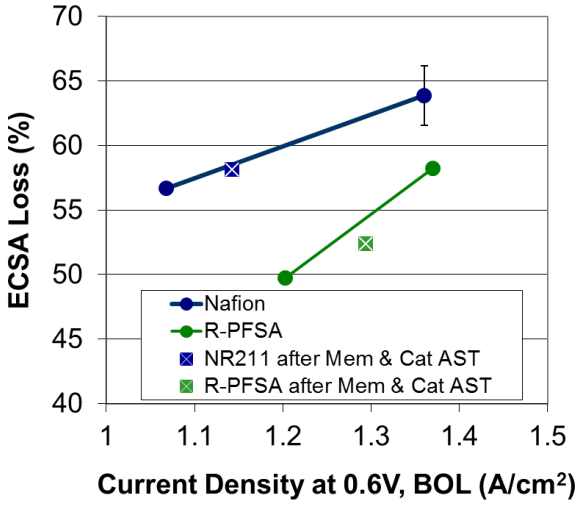

Figure 33: ECSA loss as a function of performance at 0.6V at the start of the cathode AST for MEAs with and without membrane OCV AST cycles.

A comparison of the ECSA loss and the current density at 0.6V at the start of the cathode AST for fresh MEAs and those having pre-existing membrane degradation show that the same relationship for each membrane family is followed (Figure 33). This suggests that the lower ECSA loss with pre-existing membrane degradation is related to the lower performance leading to lower water production and water crossover during the 0.6V hold of the AST cycle.

The air performance loss with cathode AST for the fresh and degraded membranes is given in Figure 34. Similar to the ECSA loss analysis, the air performance loss was normalized to the start of cathode AST for the membrane AST samples. This shows that despite the lower ECSA losses, the degraded membranes had higher performance losses than their corresponding non-degraded membranes. Figure 35 shows that the majority of the performance variations with different AST testing were due to CL Ionic losses. Compared to BOT, both the cathode and membrane AST tests resulted in increased CL ionic losses. With the combination of a membrane AST followed by the cathode AST, the resulting CL ionic losses were much more than the additive effect of each AST alone.

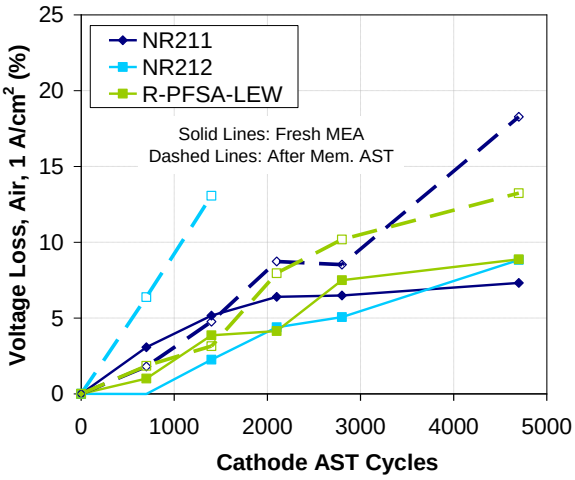

Figure 34: Voltage loss vs. cathode AST cycles for fresh (solid lines) and degraded (dashed lines) membranes.

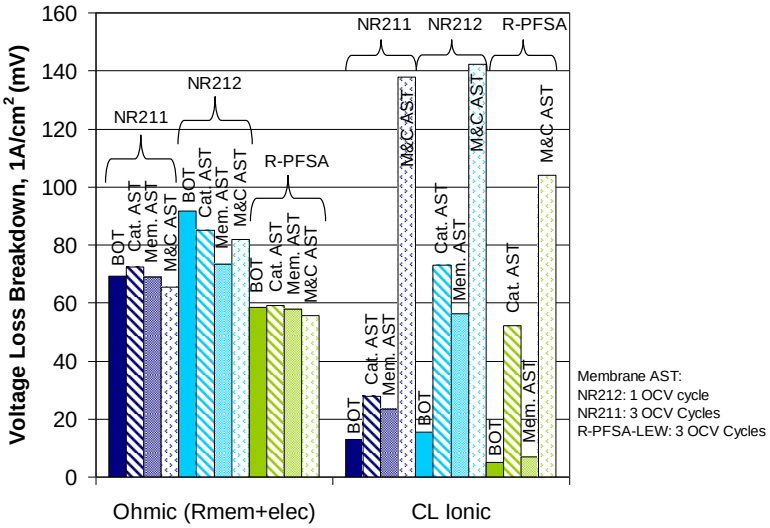

Figure 35: Ohmic and CL ionic losses before and after membrane and cathode ASTs for NR211, NR212 and R-PFSA-LEW membranes.

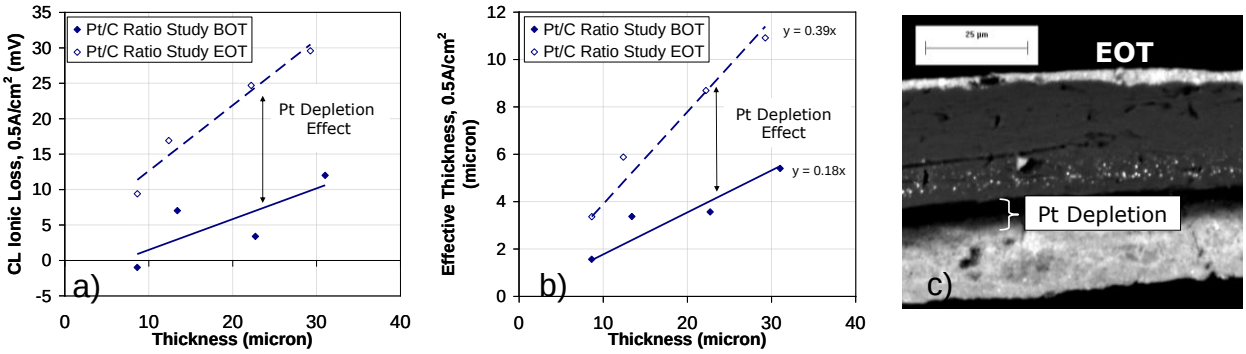

Figure 36: a) Catalyst layer ionic loss and b) effective thickness as a function of CL thickness before and after cathode AST for Pt/C ratio samples with NR211 membrane and c) an example SEM image showing Pt depletion at the membrane / catalyst interface at EOT[24].

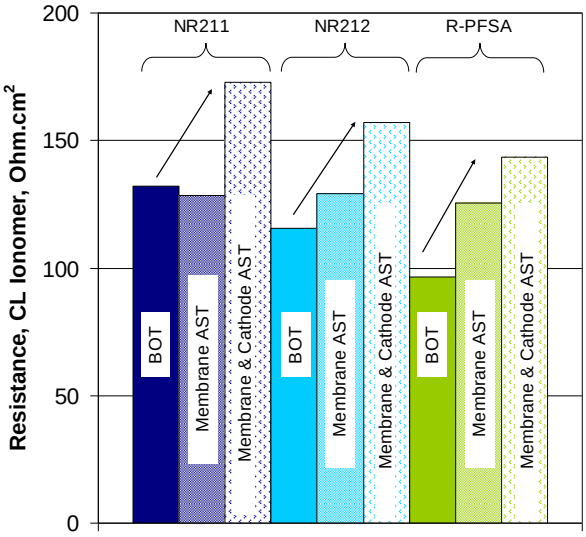

Figure 37: CL ionomer resistance before and after membrane and cathode ASTs for NR211, NR212 and R-PFSA-LEW membranes.

In the previous project[24] it was explained that high CL ionic losses occurring after cathode AST were due to the local platinum depletion at the membrane / cathode interface (Figure 36). The reaction distribution shifted further into the catalyst layer, beyond the depleted region to access the catalyst sites. This was shown by the effective thickness, which is a measure of the reaction distribution in the catalyst layer, calculated from the CL ionic loss and CL resistivity. The increase in effective thickness agreed with the thickness of the platinum depleted region as measured by SEM (Figure 36). This resulted in increased CL ionic losses due to the additional catalyst ionomer resistance associated with the longer conduction path.

Figure 37 shows the general trend that the CL ionomer resistance increased with the membrane AST and further increased with additional cathode AST cycling. Therefore, when both membrane and cathode ASTs are performed consecutively, the CL ionic

losses are magnified due to both a loss of CL conductivity and platinum depletion at the membrane / cathode interface. The effective thicknesses given in Figure 38 show that while the reaction distribution shifted further into the catalyst layer after the cathode AST, it also showed a shift with the membrane AST and a larger than expected shift for the combined ASTs. These data show that in addition to reaction distribution shifts related to Pt depletion at the membrane / catalyst interface, there are additional reaction distribution shifts due to the membrane degradation. It is hypothesized that the membrane degradation is causing increased catalyst layer hydrophilicity due to membrane degradation by-products, such as hydrophilic side chain groups, which shift the reaction distribution towards the GDL due to oxygen mass transfer effects. Therefore, the CL ionic losses observed after the combined membrane and cathode AST are related to reaction distribution shifts due to both Pt depletion and oxygen mass transfer effects influenced by catalyst layer hydrophilicity changes via membrane degradation by-product contamination. Moreover, additional CL ionic losses related to the higher CL ionic resistivity also occur. The reaction distribution effects suggest that the by-product contamination of the catalyst layer is the primary contributor to the additional CL ionic losses.

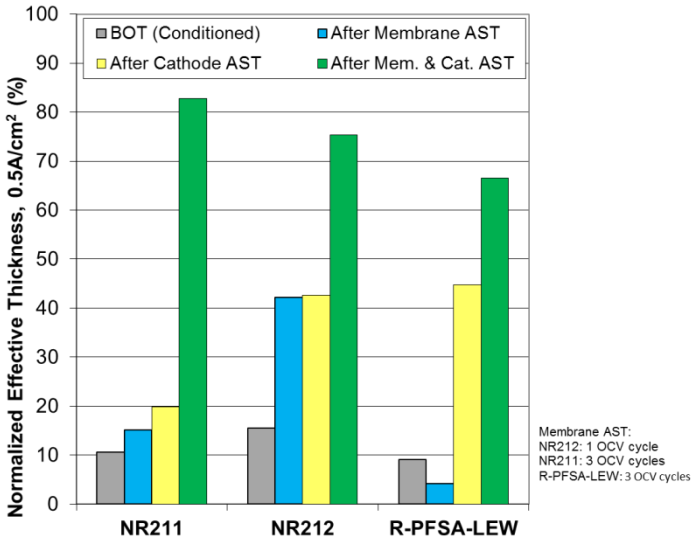

Figure 38: Normalized effective thickness before and after membrane and cathode ASTs for NR211, NR212 and R-PFSA-LEW membranes.

In summary, an interactive effect to incur greater CL ionic losses than the sum of losses of each AST alone prevails with pre-existing membrane degradation. This is explained by a shift in the reaction distribution due to both membrane degradation by-products increasing the hydrophilicity of the catalyst layer and platinum depletion at the membrane / catalyst layer interface coinciding with the lower membrane / ionomer conductivity after membrane degradation. Thus the catalyst layer ionomer resistance is larger due to both longer conduction path and lower proton conductivity and causes the higher performance losses.

2.3.2.4 Effect of Membrane Degradation Cycles

To study the effect of membrane degradation cycles on cathode degradation, the NR212 was degraded with one and three OCV cycles before running the cathode AST. Figure 39a) shows the increase in membrane thinning and decrease in ECSA with OCV cycles. Linear correlations of ECSA loss, membrane conductivity loss and H_2 crossover increase with membrane thinning were observed, as shown in Figure 39 b) and Figure 40. Similarly, the performance also decreased linearly with membrane thinning (Figure 41a). The effect of membrane thinning on performance losses is given in Figure 41b). The ohmic losses decreased due to reduced membrane thickness, while the CL ionic losses increased. Although these correlations were non-linear, the ohmic and CL ionic losses were observed to correlate linearly with OCV cycles (not shown).

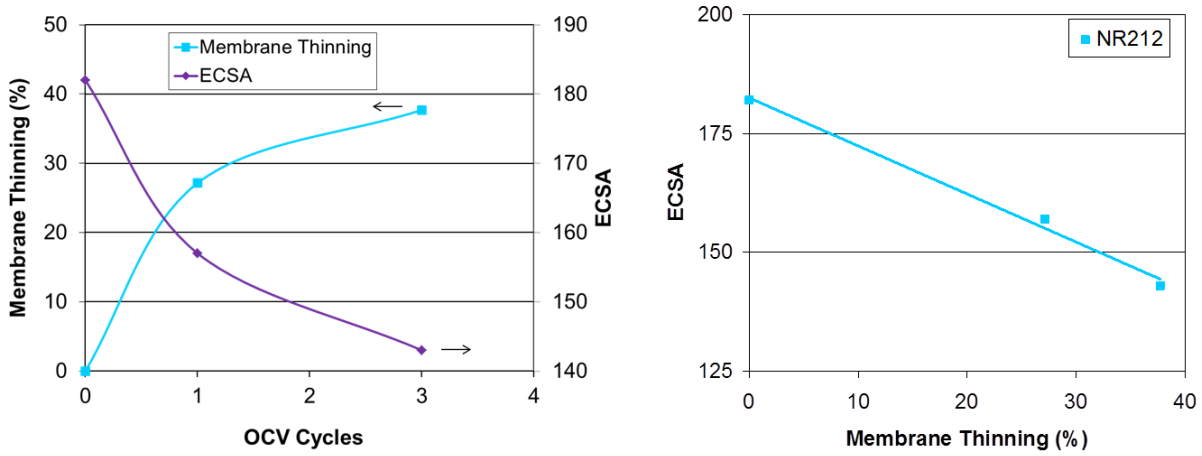

a) b)

Figure 39: a) Impact of OCV cycles on membrane thinning and ECSA and b) Correlation of ECSA with membrane thinning for NR212 membrane.

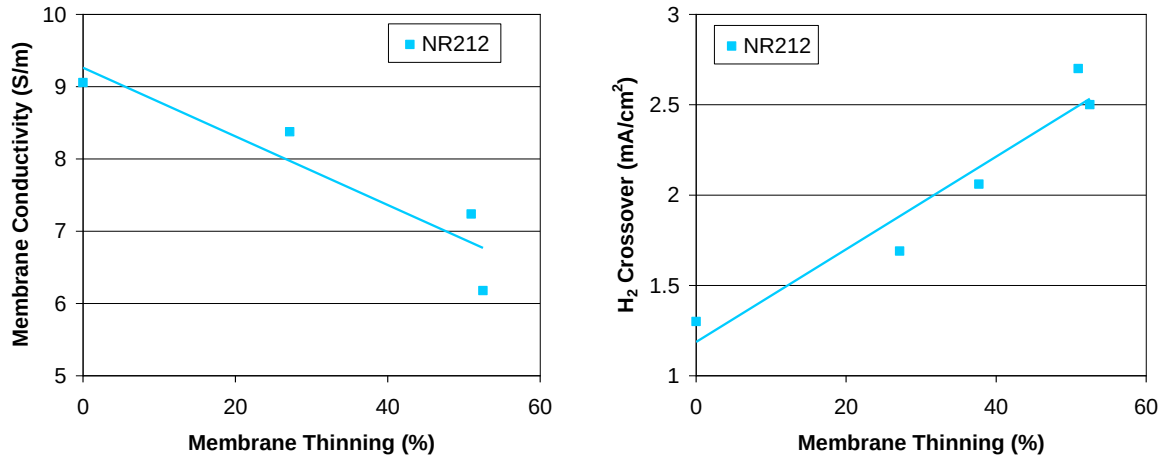

a) b)

Figure 40: Impact of membrane thinning on a) membrane conductivity and b) H_2 crossover for NR212 membrane.

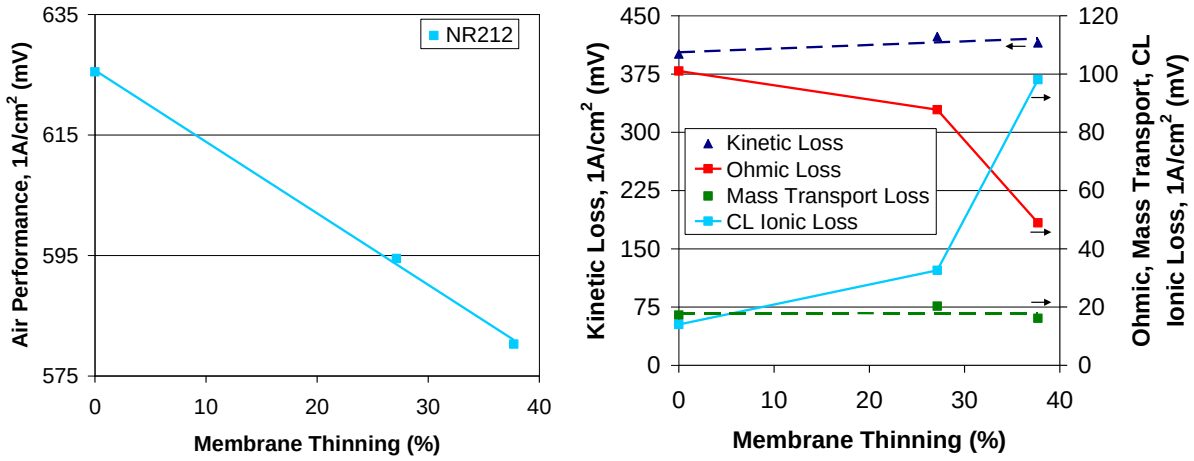

a) b)

Figure 41: Impact of membrane thinning on a) air performance and b) kinetic, ohmic, mass transport and CL ionic losses for NR212 membrane.

Figure 42 shows the air polarization curves and air performance loss for NR212 with 0, 1 and 3 OCV cycles, before and after the cathode AST. The after cathode AST results are presented at 1400 cycles, since the 3 OCV cycle test developed an internal leak and could not be tested further. The degraded membrane tests showed greater performance loss with cathode AST cycling than for the no OCV comparison. Moreover, increased OCV cycles had a greater impact on performance with subsequent cathode AST cycling.

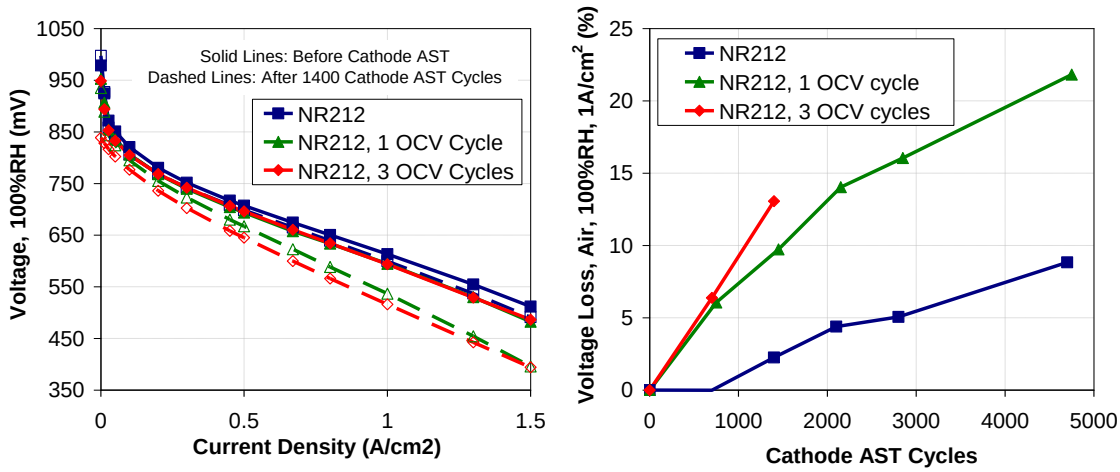

a) b)

Figure 42: Polarization curves for NR212 with 0, 1 and 3 OCV cycles, before and after 1400 Cathode AST cycles. b) Voltage loss with cathode AST cycles for NR212 after 0, 1 and 3 OCV cycles.

ECSA losses increased with higher levels of pre-existing membrane degradation, as shown in Figure 43. This was not observed for the NR211 and R-PFSA-LEW membranes, which showed lower ECSA losses with membrane degradation. Both degraded NR212 tests did not depart from the fresh NR212 ECSA loss curve until after 700 cycles when the hydrogen crossover started increasing (Figure 44a), suggesting additional membrane degradation occurred during the cathode AST. In comparison, the no OCV test showed decreasing H_2 crossover with cathode AST cycling due to the consumption of crossover hydrogen through the reaction with crossover oxygen at the PITM band location (see Figure 44b showing the correlation of H_2 crossover and PITM content after various cathode AST cycles). Since the NR212 tests behaved differently than NR211 and R-PFSA-LEW it is inferred that these results may be convoluted with additional membrane degradation occurring during the cathode AST. In contrast to recoverable membrane degradation by-product catalyst poisoning effects reported in literature[25], the NR212 membrane degradation effects were not found to be recoverable. Although membrane degradation occurrence during cathode AST was not the desired intent of the testing for purposes of model validation, this mixed mode of degradation is relevant for fuel cell operation and is recommended for further investigation.

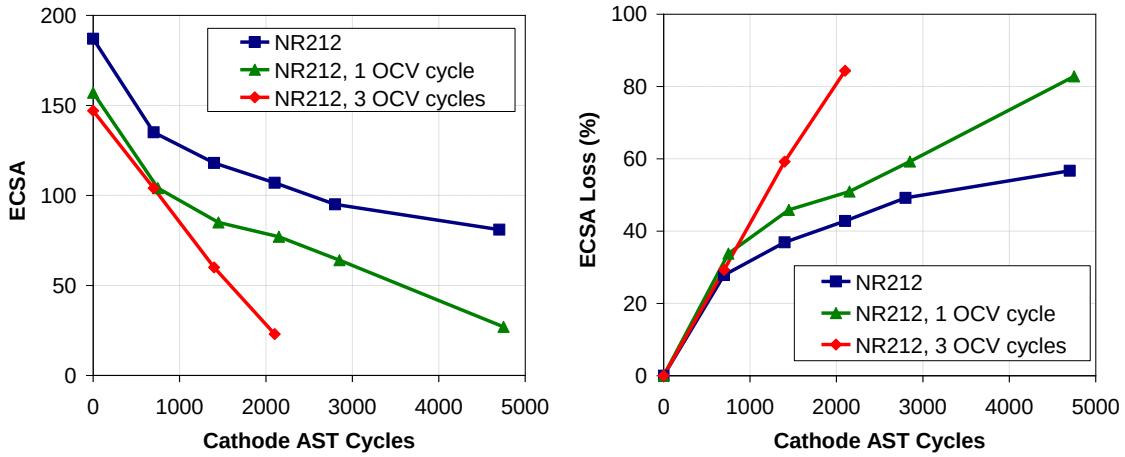

Figure 43: a) ECSA and b) ECSA loss with cathode AST cycles for NR212 after 0, 1 and 3 OCV cycles.

[25] Zhang, et al, Recoverable Performance Loss (see footnote 7).

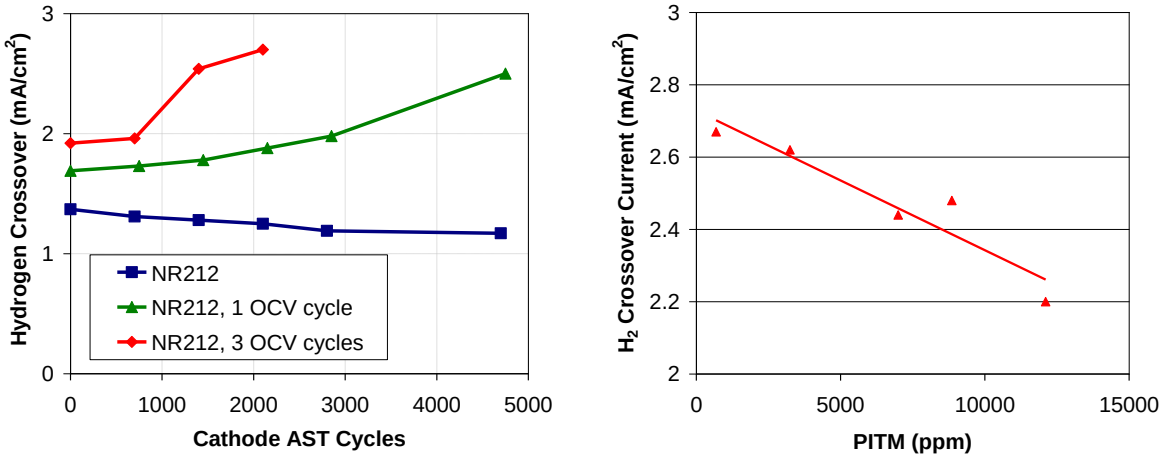

a) b)

Figure 44: a) Hydrogen crossover vs. cathode AST cycles for NR212 MEAs with 0, 1 and 3 OCV cycles and b) effect of PITM on hydrogen crossover for NR211 MEAs undergoing different numbers of cathode AST cycles.

In summary, membrane thinning increased with OCV cycles and linear correlations of membrane conductivity, hydrogen crossover, and air performance with membrane thinning were observed. The air performance losses were mostly due to increased CL ionic losses, although ohmic loss improvements also occurred. In contrast to the NR211 and R-PFSA-LEW which showed less ECSA losses with pre-existing membrane degradation due to reduction in Pt migration and water content related to lower current density during the 0.6V hold, the NR212 showed increased ECSA loss with concurrent membrane degradation. This is suggestive of an additional failure mode occurring.

2.3.2.5 Impact of Membrane Degradation at Low Pt Loading

Since lowering Pt loadings is an important goal for reducing costs, the impact of membrane degradation (NR211) at low cathode Pt loadings of 0.2 mg/cm^2 and 0.05 mg/cm^2 was studied.

The effects of Pt loading[24] on cathode degradation and performance, without membrane degradation, are shown in Figure 45. The results show that the rate of ECSA and performance degradation increases substantially as the platinum loading drops below 0.3 mg/cm^2. The performance vs. ECSA relationship (Figure 45b) shows a slight decrease in performance with decreasing ECSA until an ECSA of $\leq$ 60, where the performance becomes much more sensitive.

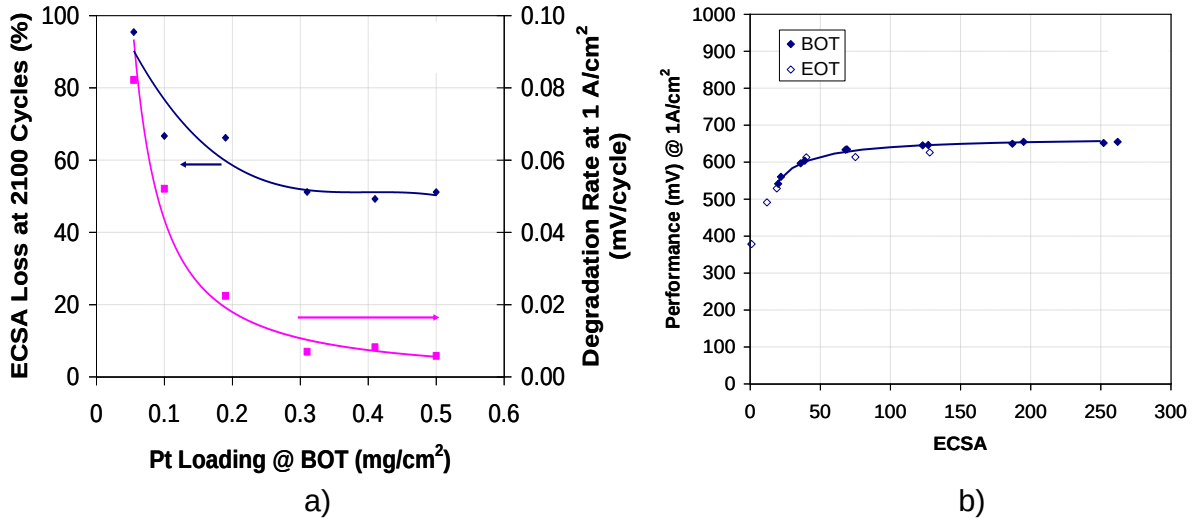

a) b)

Figure 45: a) Effect of BOT Pt loading on degradation rate, b) correlation of performance and ECSA[24].

The impact of membrane degradation on the cathode degradation of low loaded cathode catalyst layers was investigated at 0.2 mg/cm^2 and 0.05 mg/cm^2 Pt loadings. The 0.2 mg/cm^2 showed pinhole formation after 1400 cycles, as seen by the large H_2 crossover rates in Figure 46, so only data up to 1400 cycles was considered.

The ECSA and performance data are shown in Figure 47 and Figure 48, respectively. All three loadings showed ECSA and performance losses after membrane OCV cycles and an improvement in ECSA degradation rate with additional cathode AST cycling in comparison to the corresponding fresh samples. Although the 0.05 mg/cm^2 loaded degraded MEA showed similar relative performance losses as the corresponding fresh sample, unlike the 0.4 mg/cm^2 loaded MEA, a comparison of air performance vs. ECSA shows that both membrane degraded tests indicated performance sensitivity in comparison to the fresh samples (Figure 49). The cathode AST results for the fresh samples follow the same relationship as the Pt loading study BOT samples discussed above. In contrast, the membrane degraded tests at both baseline and low loading showed lower performance than the BOT relationship. These additional losses from the BOT relationship are due to increased CL ionic losses associated with ionomer degradation and platinum depletion discussed above. After 2100 voltage cycles, the membrane degraded 0.05 mg/cm^2 loaded MEA showed over 100mV lower performance than the BOT performance vs ECSA relationship, while the membrane degraded 0.4 mg/cm^2 loaded MEA showed only 50mV deviation. This clearly shows that the lower Pt loaded MEA was more sensitive to cathode degradation following membrane degradation.

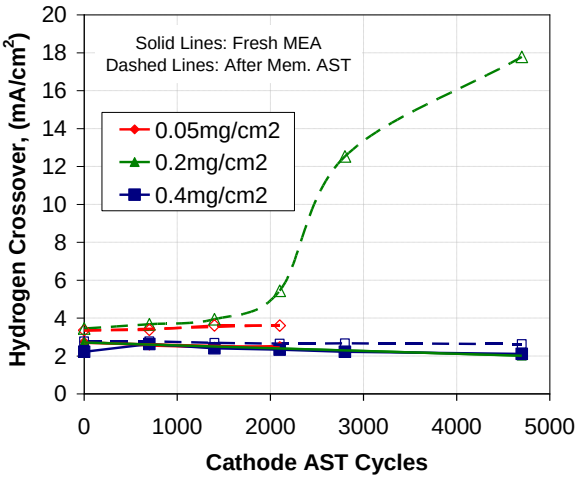

Figure 46: Hydrogen crossover as a function of cathode AST cycles for fresh and degraded (3OCV cycles) NR211 membranes with 0.05mg/cm^2, 0.2mg/cm^2 and 0.4mg/cm^2 cathode Pt loadings.

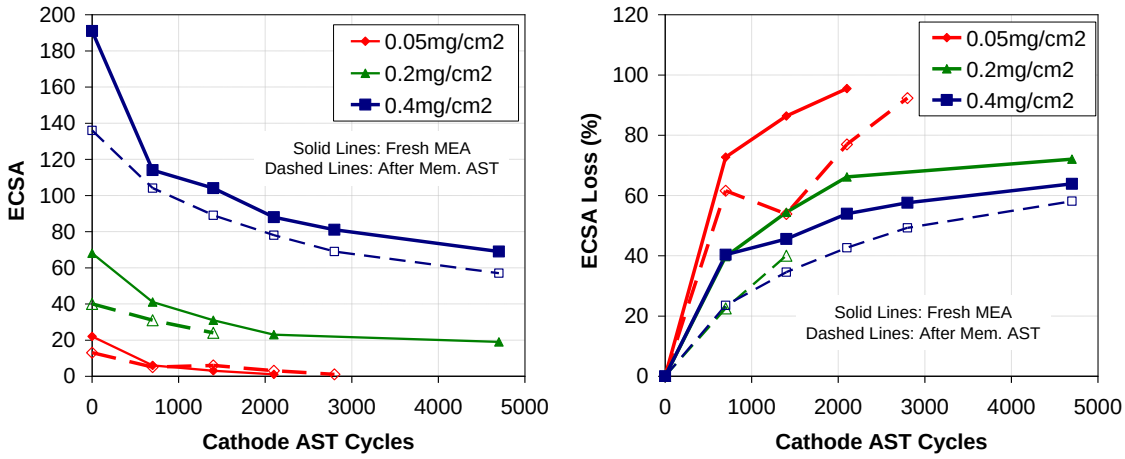

a) b)

Figure 47: ECSA loss as a function of cathode AST cycles for fresh and degraded (3OCV cycles) NR211 membranes with 0.05mg/cm^2, 0.2mg/cm^2 and 0.4mg/cm^2 cathode Pt loadings.

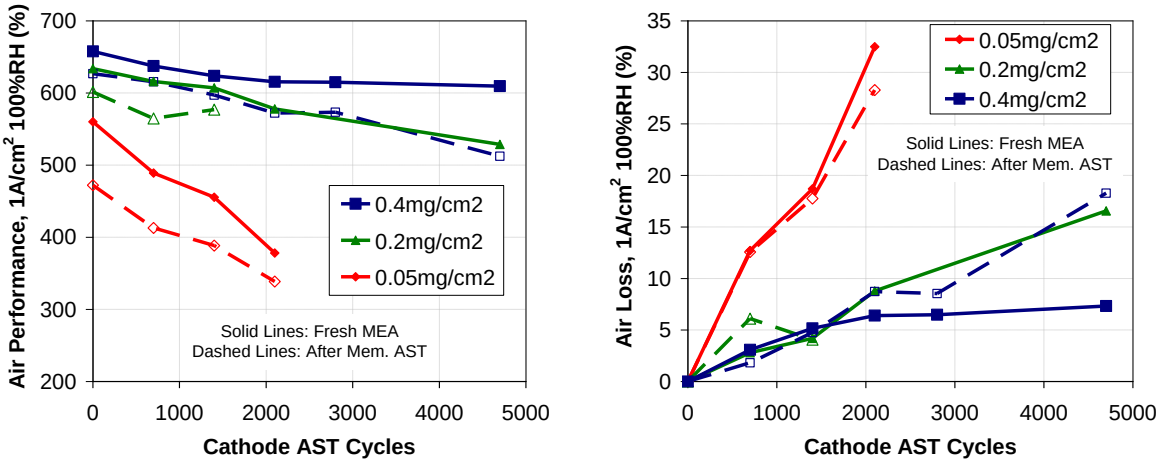

a) b)

Figure 48: a) Performance and b) performance loss as a function of cathode AST cycles for fresh and degraded (3 OCV cycles) NR211 membranes with 0.05mg/cm^2, 0.2mg/cm^2 and 0.4mg/cm^2 cathode Pt loadings.

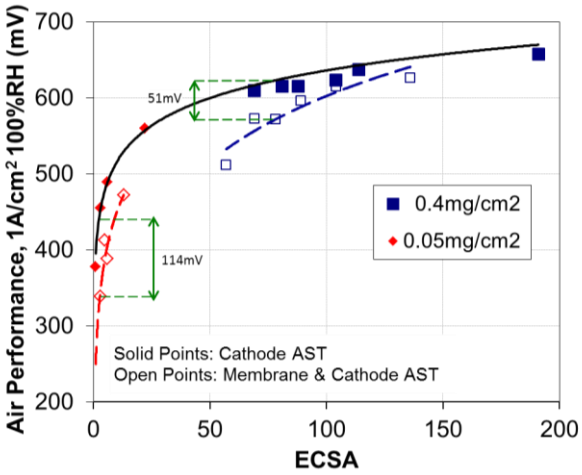

Figure 49: Performance as a function of cathode ECSA during cathode AST cycling for fresh and degraded (3OCV cycles) NR211 membranes with 0.05 mg/cm^2 and 0.4 mg/cm^2 cathode Pt loadings. Deviation from the performance vs ECSA relationship after 3 OCV and 2100 cathode AST cycles are highlighted for both loadings.

In summary, while the lower loadings behaved similarly to the baseline loading in that there were ECSA and performance losses due to OCV membrane degradation and the ECSA losses with subsequent cathode AST cycling were less than for the fresh samples, they had greater deviation from the performance vs ECSA relationship for fresh samples than the higher loading.

2.4 Summary / Conclusions

Six membranes were tested for the effects of membrane properties on BOT performance and cathode AST durability. In addition, three of the membranes underwent chemical membrane degradation to observe the changes in membrane properties and the effects on performance and cathode AST durability.

The membrane transport parameters, including membrane resistance, hydrogen permeance, water crossover and water uptake, were affected by the membrane thickness and EW, in addition to operating conditions including temperature and humidity. After normalizing for thickness, the membrane transport properties including membrane conductivity and hydrogen permeability showed a correlation to the membrane water uptake. These interactions of the membrane component characteristics and the membrane transport properties were represented in a flow chart.

Membrane resistance and membrane water uptake were the dominant parameters for performance variations at BOT due to effects on ohmic and CL ionic losses, respectively. In addition to these effects, after membrane degradation, the loss of CL ionomer conductivity resulted in additional CL ionic losses.

ECSA degradation for pristine membranes increased for thinner and/or higher EW membranes within a membrane family and several different hypotheses were discussed. With pre-existing membrane degradation, the ECSA degradation during the cathode AST was decreased.

After membrane degradation at OCV, losses in membrane thickness, membrane conductivity, performance and ECSA were observed. In addition the hydrogen crossover increased due to the membrane thinning. It is hypothesized that the membrane degradation resulted in lower current and therefore catalyst layer water content at 0.6V which resulted in lower ECSA degradation.

Although the ECSA degradation was lessened with pre-existing membrane degradation, the performance losses were worse. The increased performance losses are explained by the combination of higher CL ionomer resistance, and reaction distribution shifts due both to increased catalyst layer hydrophilicity with membrane by-product contamination and platinum depletion, which leads to higher CL ionic losses related to a reaction distribution shift further into the catalyst layer. These additional performance losses caused a deviation from the expected performance vs ECSA relationship, and it was found that this sensitivity was increased for lower platinum loading.

When membrane degradation occurs during the cathode AST, as was seen for NR212, both ECSA and performance losses increased significantly. This is suggestive of an additional failure mode occurring and requires further studies.

All in all, membrane transport properties were found to have a significant effect on BOL performance and durability, and therefore, need to be considered in performance and durability models as well as design work.

3 Material/Component Characterization

University of New Mexico: XPS Analysis of Catalyst layers, K. Artyushkova (PI)

3.1 Introduction and Background

This chapter describes the catalyst layer characterization that was carried out by the University of New Mexico. The objective of this work was to complement the AST investigations and modeling activities at Ballard by identifying catalyst layer surface speciation and content changes using X-ray Photoelectron Spectroscopy (XPS) measurements.

XPS provides critical information on the chemical composition of the electrocatalyst and ionomer within the catalyst layer. In the previous project, structure-to-performance correlations were developed linking catalyst and catalyst layer properties with CCM performance and degradation[26,27]. For example, after AST cycling, increases in cathode catalyst layer relative percentage of metallic Pt and surface oxides C_xO_y, such as carbonates and carboxylates, correlated to the Pt size and voltage losses, respectively. In addition, XPS was found to be a tool to monitor the changes in ionomer morphology within the catalyst layer with the catalyst surface properties and water content that have also been reported in literature[28-35] for idealized thin ionomer films.

Several experimental studies, using model ionomer thin films coated on idealized substrates such as SiO_2, Au, Pt, glassy carbon, and other functionalized versions, have shown that the Nafion morphology is dependent on the substrate material, hydrophilicity, and humidity, with varied morphologies being proposed[28,29,30,31]. In addition, molecular dynamics and experimental studies of ionomers films coated on

---

[26] Artyushkova, K.; Atanassov, P.; Dutta, M.; Wessel, S.; Colbow, V., Structural correlations: Design levers for performance and durability of catalyst layers. *Journal of Power Sources* **2015,** *284*, 631-641.

[27] Artyushkova, K.; Patel, A.; Atanassov, P.; Colbow, V.; Dutta, M.; Harvey, D.; Wessel, S., Statistical Structure-to-Property Relationships for Fuel Cell Materials. *Materials Characterisation VI: Computational Methods and Experiments*, **2013**, 77-86.

[28] Wood, D. L. III; Chlistunoff, J.; Majewski, J.; Borup, R. L., Nafion Structural Phenomena at Platinum and Carbon Interfaces. *Journal of the American Chemical Society* **2009,** *131* (50), 18096-18104.

[29] Ohira, A.; Kuroda, S.; Mohamedz, H. F. M.; Tavernier, B., Effect of interface on surface morphology and proton conduction of polymer electrolyte thin films. *Physical Chemistry Chemical Physics* **2013**, *15*, *11494-11500.*

[30] Dura, J. A.; Murthi, V. S.; Hartman, M.; Satija, S. K.; and Majkrzak, C. F., Multilamellar Interface Structures in Nafion. *Macromolecules* **2009,** *42* (13), 4769–4774.

[31] Paul, D. K.; Fraser, A.; Pearce, J.; Karan, K., Understanding the Ionomer Structure and the Proton Conduction Mechanism in PEFC Catalyst Layer: Adsorbed Nafion on Model Substrate. *ECS Transactions* **2011,** *41* (1), 1393-1406.

graphite and Pt/graphite surfaces have shown that the Nafion® morphology is also dependent on the surface characteristics of the substrate[32,33,34,35]. For example, Mashio et al.[32], have shown through molecular dynamics studies of Nafion® oligomers on bare graphite that the ionomer is predominantly adsorbed on the graphitized carbon sheet via the backbone, while the side chains face toward the pore space. The addition of ionized functional groups to the graphite surface resulted in an increase in the number of sulfonic acid groups near the graphite surface. Lamas' et al.[33], molecular dynamic studies of the polymer-catalyst-carbon interface have shown that the side chains interact preferentially with the Pt catalytic particles through the sulfonic groups.

Recent molecular dynamics work by Borges et al[35], has used a tunable surface, by including a hydrophilicity parameter, which could simulate hydrophobic and hydrophilic surfaces with contact angles between 30° - 150°. The ionomer interaction with surfaces ranging from highly hydrophobic to highly hydrophilic at low, medium and high water contents revealed different proposed morphologies including sandwich, cluster and multilayer structures, among others. According to the molecular dynamics modelling and morphologies proposed[35], the ionomer/air interface is hydrophobic with the backbone facing the pore and side chains pointing toward the substrate for all conditions, while the substrate hydrophilicity and water content results in different layered or clustered ionomer orientations deeper into the ionomer film. As XPS gives compositional information for the top 5-10nm of the surface analyzed, these differences in ionomer orientation of backbone and side chain can be observed by the relative amounts of CF_2 and CF which are mostly present in the backbone and side chain, respectively. For example, the multilayer structure with a second layer of ionomer with sidechains pointing to the top may give a lower CF_2:CF ratio than the bilayer structure where one layer of ionomer is formed with side chains pointing toward the substrate and water layer. In our previous studies[36], changes in the relative amounts of CF_2:CF ratio in the cathode catalyst layer were correlated to the degree of oxidation of the carbon support and were also observed to change as a response to conditioning.

The focus of the present work was to characterize the cathode catalyst layers of MEAs with different membranes to determine the effects of membrane transport properties on

---

[32] Mashio, T.; Malek, K.; Eikerling, M.; Ohma, A.; Kanesaka, H.; Shinohara, K., Molecular Dynamics Study of Ionomer and Water Adsorption at Carbon Support Materials. *The Journal of Physical Chemistry C* **2010**, *114*, 13739-13745.

[33] Lamas, E. J.; Balbuena, P. B., Molecular dynamics studies of a model polymer–catalyst–carbon interface. *Electrochimica Acta* **2006**, *51*, 5904-5911.

[34] Masuda, T.; Naohara, H.; Takakusagi, S.; Singh, P. R.; Uosaki, K.; Formation and Structure of Perfluorosulfonated Ionomer Thin Film on a Graphite Surface. *Chemistry Letters* **2009**, *38* (9), 884-885.

[35] Borges, D. D.; Gebel, G.; Franco, A. A.; Malek, K.; Mossa, S., Morphology of Supported Polymer Electrolyte Ultrathin Films: A Numerical Study. *The Journal of Physical Chemistry C* **2015**, *119* (2), 1201-1216.

[36] Artyushkova, et al, Structural correlations (see footnote 26).

the catalyst layers, in particular on the ionomer morphology and show experimental correlations. MEAs were examined after conditioning and aging to investigate the effects of membrane transport properties and membrane degradation on cathode durability.

3.2 Experimental

X-ray photoelectron spectroscopy (XPS)

XPS measurements were performed using Kratos Axis Ultra DLD spectrometer using an Al Kα X-ray source, with an emission voltage of 15 kV and emission current of 10 mA. Three large area spectra from 300x700 micron areas were acquired for each sample analyzed. The base pressure was about $2x10^{-10}$ torr, and operating pressure was around $2x10^{-9}$ torr. Survey and high-resolution spectra were acquired at pass energies of 80 eV and 20 eV, respectively. Data analysis and quantification were performed using CasaXPS software. A linear background subtraction was used for quantification of C1s, F 1s and O1s while Shirley background was used for Pt 4f spectra. Sensitivity factors provided by the manufacturer were utilized. Spectra were fitted with a series of 70% Gaussian/30% Lorentzian line shapes. Figure 50 and Figure 51 show examples of the high resolution C1s and Pt 4F spectra and deconvolution of the different surface species.

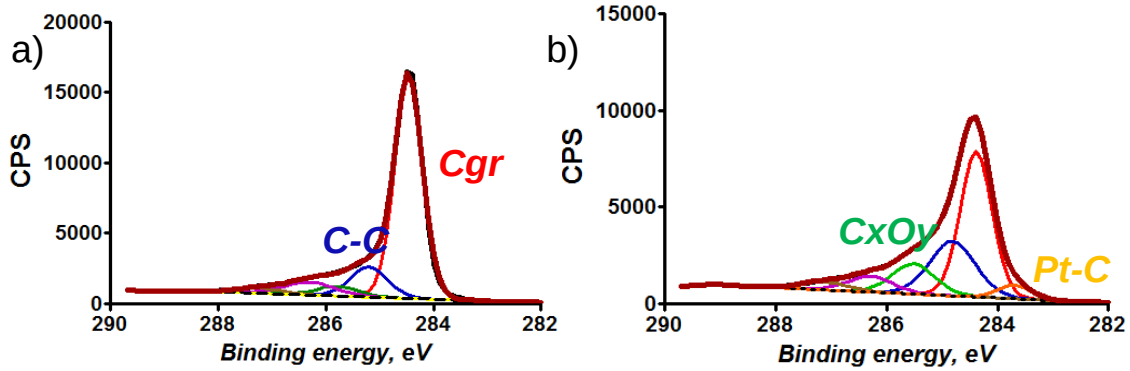

Figure 50: High resolution C 1s spectra for a) LSAC and b) HSAC samples.

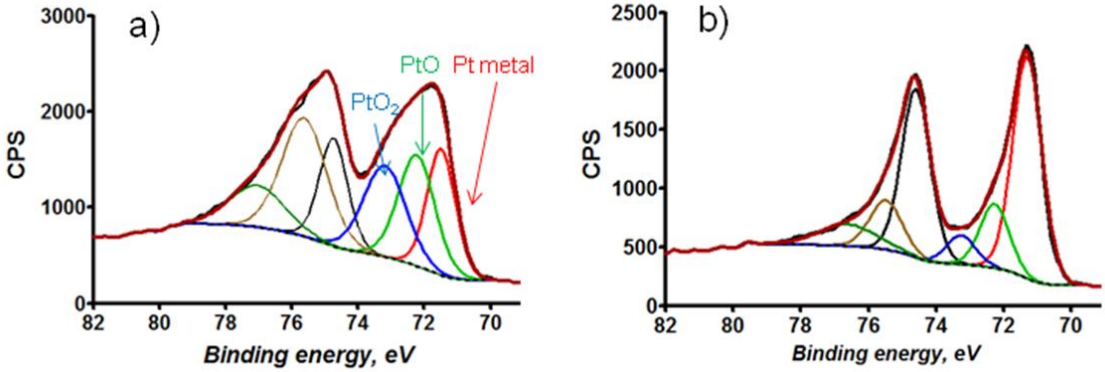

Figure 51: High resolution Pt 4f spectra for a) HSAC2 and b) HSAC-HT samples.

3.3 Results and Discussion

XPS analysis was performed on the exposed catalyst layers after removal of the GDLs, for conditioned BOT and aged MEAs from the experimental workstream. XPS provides the chemical composition from the top 5-10nm of the material analyzed. Six peaks in the spectra come from the catalyst itself with the major components identified as graphitic carbon (C_{gr}, 284.3 eV), aliphatic carbon (C-C, 285 eV), secondary carbons (C*-C-O, 286.0 eV) and three types of carbon-oxygen bonding (C-OC/ C-OH, 286.9 eV; C=O, 288 eV and COOH, 289.3 eV). Ionomer contributes mainly to the higher binding energy regions with three peaks identified as partially fluorinated carbons (C-F, 290.2 eV), fully fluorinated carbons (CF_2-CF_2, 291 eV) and peak due to the C-F_3 end-group or C-OF_2 groups in the polymer pendant sidechain (292.9 eV). Quantitative results of the distribution of different types of carbon species provided by XPS are suitable as they are representative of oxidation changes in the carbon chain (amount of C_xO_y species) as well as a measure of ionomer morphology due to the ability to separate C-F (located in side chain and branch point) and CF_2 (mainly located in the backbone).

Performing Principal Component Analysis (PCA), an exploratory tool that converts a set of observations into a set of values of uncorrelated variables called principal components, of the XPS data set for the BOT samples (shown in Figure 52), resulted in the identification of 3 groups. The left half of the plot shows a large group (Group 1) of similar samples with large amounts of carbon, Pt, surface oxides, metallic Pt and CF. This group contains the Nafion and R-PFSA membranes. A separate group (Group 2) in the upper right quadrant of the PCA plot, containing the R-HC membranes which were associated with the largest amounts of F, CF_2 and CF_3 species, was identified. Similarly, the bar chart of the elemental composition of the BOT cathode catalyst layers, in Figure 53, highlights the difference between the first and second groups of the PCA plot. The R-HC membranes, with a partially fluorinated hydrocarbon ionomer type, resulted in noticeably different elemental composition of the cathode catalyst layers, with higher F and O content than with the Nafion and R-PFSA membranes. As the experimental R-HC membranes showed durability issues, there may have been some catalyst by membrane degradation components resulting in the higher F and O contents.

The PCA plot in Figure 52 also revealed a third group (Group 3) in the lower right quadrant, which had the largest amount of CF_2:CF ratio. It was found that these were repeat test articles of the Nafion and R-PFSA membranes, which did not undergo the full suite of diagnostics as did the other MEAs, and in particular did not undergo the water crossover testing at varied humidity gradients. Whereas both groups were last conditioned at 75°C, 0A/cm^2 and 100%RH humidity on the anode, Group 3 had a 100%RH humidified cathode inlet, while Group 1 was dry (0 %RH) at the cathode inlet. Therefore the cathode catalyst layer of Group 1 is expected to have lower water content than Group 3. As previous studies have shown that the ionomer morphology of thin ionomer films is dependent on the water content[35], it is not surprising that the MEAs with

different cathode inlet humidities gave different XPS results, especially the CF_2:CF ratio, an indicator of ionomer side chain / main chain orientation variations.

As the XPS results differentiated between the repeat MEAs by operation history, the MEA storage period and XPS testing environment did not allow for the previous operating history to be removed. This is in agreement with other studies that have shown that ionomer relaxation is a slow process at room temperature[37]. Due to this sensitivity to operational history, the results from the repeat MEAs that did not undergo the water crossover testing were not included in comparisons and correlations related to ionomer morphology.

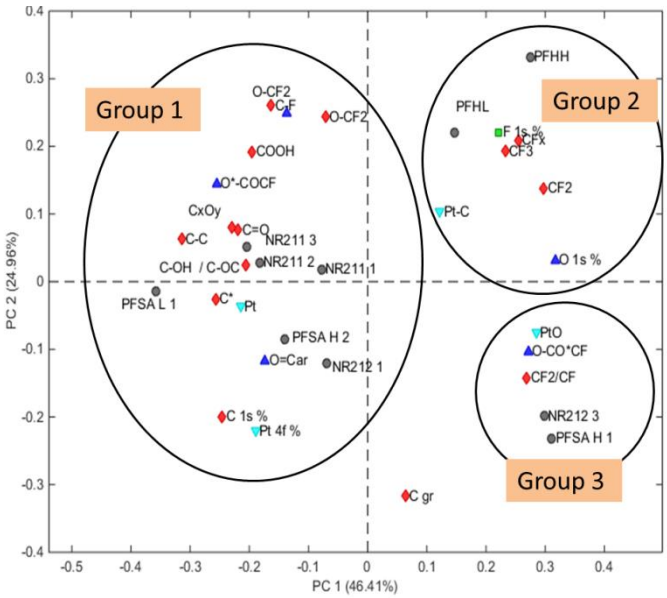

Figure 52: PCA biplot for BOT cathode catalyst layer XPS results.

[37] Abuin, G. C.; Fuertes, M. C.; Corti, H. R., Substrate Effect on the Swelling and Water Sorption of Nafion Nanomembranes. *Journal of Membrane Science* **2013,** *428*, 507–515.

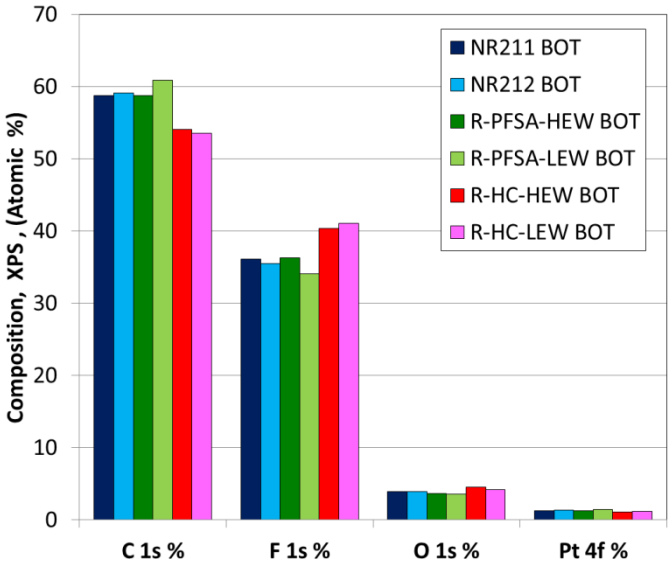

Figure 53: Catalyst layer surface elemental composition for MEAs with different membranes.

In addition to the higher CF_2:CF ratio observed for the Group 3 MEAs which had a wetter cathode catalyst layer due to higher inlet humidity than Group 1 MEAs, correlations of CF_2:CF ratio with membrane thickness and in situ water crossover results were also observed at BOT for the Nafion and R-PFSA (Group 1) membranes as shown in Figure 54. The thicker membranes with the higher water crossover to the cathode, and therefore higher cathode catalyst layer water content showed higher CF_2:CF ratios. In relation to the morphologies proposed by Borges[35], as discussed above, increasing the water content of the layer to favor the bilayer ionomer morphology over the multilayer morphology resulting in a higher CF_2:CF ratio is a possible explanation. Although these correlations may not be causal, they support the general conclusion that the ionomer morphology changes (swelling, reorientation) with the CCL water content, where greater CL water content also results in greater Pt dissolution.

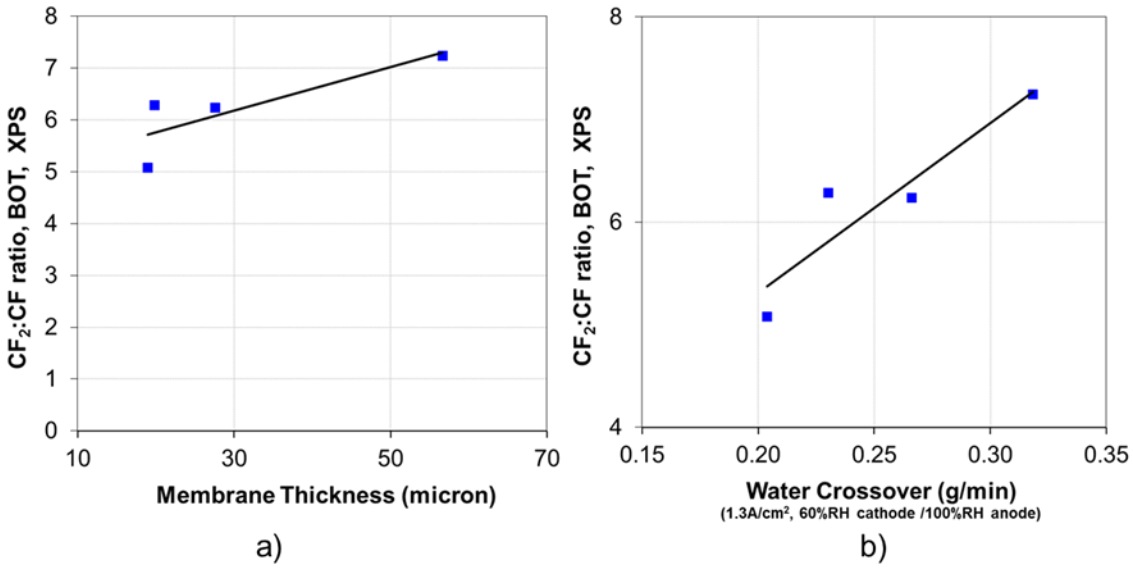

Figure 54: Correlation of BOT catalyst layer CF_2:CF ratio and a) membrane thickness and b) in situ water crossover for Nafion and R-PFSA membranes.

After membrane degradation through OCV cycling, it was observed that for all three membranes tested the oxygen content of the cathode catalyst layer increased. Neither the double layer capacitance, nor the CxOy and PtO speciations showed significant and/or consistent increase after OCV testing, so the increase in oxygen content is not expected to be due carbon or platinum surface oxidation. Alternatively, it is hypothesized that membrane degradation by-products, such as side chain fragments, wash into the catalyst layer, resulting in the increased oxygen content. In addition, as discussed in the experimental chapter, it is hypothesized that the membrane degradation by-products may increase the hydrophilicity of the catalyst layer, resulting in catalyst layer flooding, causing poor oxygen mass transfer and a shift in the reaction distribution towards the GDL which consequently increases CL ionic losses. The correlation of increasing effective thickness, which is a measure of the reaction distribution in the catalyst layer calculated from the CL ionic loss and CL resistivity, and increasing oxygen content of the catalyst layer for the MEAs after membrane AST testing (Figure 55) supports this hypothesis. After the cathode AST or the combined cathode and membrane ASTs, similar relationships were not observed as the reaction distribution was convoluted due to Pt dissolution effects.

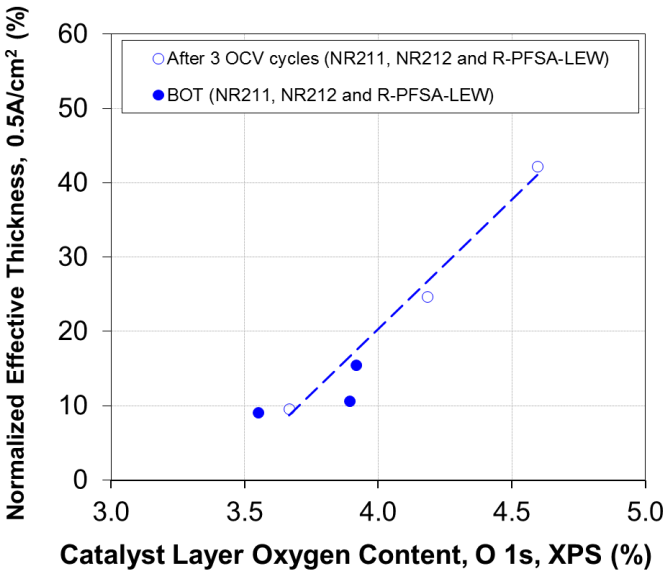

Figure 55: Correlation of normalized effective thickness, a measure of the reaction distribution in the catalyst layer, and catalyst layer oxygen content by XPS.

3.4 Summary / Conclusions

XPS results showed that the cathode catalyst layers of the membranes studied showed differences at BOT and after AST cycling. The R-HC MEAs were clearly different from the Nafion and R-PFSA MEAs, possibly due to durability and contamination issues. The Nafion and R-PFSA MEAs showed a correlation of the BOT CF_2:CF ratio, an indication of the ionomer side chain / main chain orientation, with the water crossover, suggesting that the catalyst layer ionomer morphology was affected by the membrane transport properties. After membrane degradation the oxygen content of the catalyst layer increased and this correlated with the effective thickness, a measure of the reaction distribution, which supports the hypothesis that membrane degradation contaminates the catalyst layer and increases the hydrophilicity/flooding leading to a shift in reaction distribution toward the GDL.

4 Theoretical Simulations

4.1 Introduction

Results from the experimental portion of this project demonstrate that membrane properties, composition and structure can affect the rate and extent of catalyst layer degradation. Proper, quantitative description of the distribution of water in the membrane and catalyst layer ionomer is clearly important for discerning the role of water in these interactions, and this was the primary goal of the modeling workstream.

The *as-planned* stages of the modeling portion of this project were: i) identify the most promising set of candidate physics to describe the membrane over a broad compositional and operational design space, ii) develop a membrane sub-model and validate the physics and transport properties against ex-situ water transport data, and iii) integrate the membrane physics into the FC-APOLLO MEA model framework and then use the integrated model to explore possible interactions between catalyst degradation and membrane properties. As discussed below, not all of these objectives were achieved by the end of the project (Q2 2015). The modeling effort will continue through 2017, and the planned next stages for model development –as part of the open source FAST-FC platform– are discussed in the conclusion section.

4.2 Background & objectives

4.2.1 Numerical modeling of transport in the membrane

Modeling of proton and water transport in the membrane has been previously approached at widely different scales (nanometers to microns) and with disparate hypotheses as to the dominant transport mechanisms. Microscopic models at the nanometer scale are based on quantum mechanics, molecular dynamics and physical models based on a simplified membrane structure. These models provide insight into the influence of membrane micro-structure on transport processes but cannot realistically be extended to the full-membrane scale due to computational limitations. Macroscopic models, necessarily, do not explicitly represent the membrane micro-structure and, therefore, rely on effective transport mechanisms and properties. These models have been demonstrated to reasonably represent proton and water transport in the membrane over a range of operational conditions and have been widely-used in both characterization and design studies.

There are two end-member types of macroscopic membrane models: diffusion-type[38],[39] and hydraulic-type[40]. In general, the former considers the membrane to have a single

[38] Fuller, T. F., Solid-Polymer-Electrolyte Fuel Cells, *Ph.D. thesis*, University of California, Berkeley, **1992**.
[39] Springer, T.; Zawodzinski, T. A.; Gottesfeld, S., Polymer Electrolyte Fuel Cell Model. *Journal of the Electrochemical Society* **1991,** *138* (8) 2334-2342.

transport domain, whereas the latter assumes that transport occurs in two parallel domains. Both approaches can capture membrane behavior over specific operational windows, e.g., transport in the presence of only water vapor, but often fail when extended to conditions where both liquid water and water vapor are present.

Diffusion-type models are based on dilute solution theory[41], which assumes that interactions between solute species (water and protons) can be neglected; the only interactions accounted for are those between the solute species and the solvent (membrane). The primary driving force for transport in the diffusion-type model is typically the gradient of the membrane water content or the gradient of the water activity; however, this formulation fails to describe water transport in the presence of liquid water where water activity gradients approach zero. This problem has been addressed by considering transport as a function of gradients in the water chemical potential[42]; however, certain phenomena, such as the water content profile and the drying of the anode-side of the membrane are not always well-described[43].

Hydraulic models differ from diffusion-type models in that they consider a transport pathway in which water fluxes across the membrane are driven by gradients in liquid pressure. This liquid transport pathway can be in parallel to[44] or in lieu of a gas pore network through the membrane. These models can account for the sensitivity of water transport to saturation of the liquid pore network, hydrophobicity, and the membrane pore size distribution[45]. Under normal operating conditions, however, the anode-side of the membrane has a tendency to dry-out, such that the membrane interface is not in contact with liquid water on both sides. In this scenario, the core assumptions of many of the hydraulic-type models are not appropriate.

Most models of membrane water transport assume that the proton flux across the membrane is determined only by proton conduction, as described by Ohm's law, and that there is no influence of the water flux on proton transport. This is an outcome of the assumptions underlying dilute solution theory; however, the solute species in the membrane (water and protons) are not dilute[46], and the interactions between all specie

---

[40] Bernardi, D. M.; Verbrugge, M. W., A Mathematical Model of the Solid-Polymer- Electrolyte Fuel Cell. *Journal of The Electrochemical Society* **1992,** *139* (9), 2477-2491.
[41] Newman, J.; Thomas-Alyea, K. E., Electrochemical Systems, Electrochemical Society series, John Wiley & Sons, **2004**.
[42] Janssen, G. J. M., A Phenomenological Model of Water Transport in a Proton Exchange Membrane Fuel Cell. *Journal of The Electrochemical Society* **2001,** *148* (12), A1313-23.
[43] Buchi, F. N.; Scherer, G. G., Investigation of the Transversal Water Profile in Nafion Membranes in Polymer Electrolyte Fuel Cells. *Journal of The Electrochemical Society* **2001,** *148* (3), A183-188.
[44] Bernardi and Verbrugge, A Mathematical Model (see footnote 40).
[45] Eikerling, M.; Kharkats, Y. I.; Kornyshevf, A. A.; Volfkovich, Y. M., Phenomenological Theory of Electro-osmotic Effect and Water Management in Polymer Electrolyte Proton-Conducting Membranes. *Journal of The Electrochemical Society* **1998,** *145* (8), 2684-2699.
[46] Fuller, Solid-Polymer-Electrolyte Fuel Cells, *(see footnote 38)*.

fluxes should be considered. This can be achieved by using concentrated solution theory[47], generalized Stefan-Maxwell equations[48], dusty fluid model[49] or irreversible thermodynamics[50]. The major difficulty with such methods is the lack of easily-quantified transport parameters, and the difficulty in obtaining these parameters has made chemical potential models less popular than diffusive or hydraulic models. Despite these difficulties, a significant body of work –starting with Fuller[51] and developed to maturity by Weber and co-workers[52] – has resulted in a modified concentrate solution approach that has numerous advantages: i) water fluxes arise from gradients in water chemical potential, which can include contributions from both vapor activity and liquid pressure, ii) interactions between proton and water fluxes are inherently considered, and iii) transport properties for protons and water can be readily estimated from experimental data sets.

The chemical potential-driven approach allows for quantitative description of water and proton transport in a way that is consistent with the physical model of the membrane presented by Weber and Newman[53]. Their conceptual model describes the transition from a vapor-equilibrated state at low RH, in which connectivity between macro-pores in the membranes is very limited, to full liquid equilibration, where macro-pores are connected by a network of expanded micro-pores (Figure 56). This model reconciles the so-called "Schroeder's paradox" where membrane water uptake under liquid equilibration significantly exceeds that of a vapor-equilibrated membrane at 100% RH, even though the water activity is the same between the two conditions. As discussed in a later section, expansion of the membrane pore network is critical to describing the transition between vapor-equilibration, where diffusion dominates, and liquid-equilibration, where hydraulic permeation dominates.

---

[47] Weber, A. Z.; Newman, J., Transport in Polymer-Electrolyte Membranes I. Physical Model. *Journal of The Electrochemical Society* **2003,** *150* (7) A1008-A1015.
[48] Baschuk, J. J.; Li, X., A Comprehensive, Consistent and Systematic Mathematical Model of PEM Fuel Cells. *Applied Energy* **2009,** *86* (2), 181-193.
[49] Berg, P.; Promislow, K.; St. Pierre, J.; Stumper, J.; Wetton, B., Water Management in PEM Fuel Cells. *Journal of The Electrochemical Society* **2004**, *151* (3), A341-A353.
[50] Auclair, B.; Nikonenko, V.; Larchet, C.; Mffetayer, M.; Dammak, L., Correlation Between Transport Parameters of Ion-exchange Membranes. *Journal of Membrane Science* **2002,** *195* (1), 89-102.
[51] Fuller, Solid-Polymer-Electrolyte Fuel Cells, *(see footnote 38)*.
[52] Weber, A. Z.; Newman, J., Transport in Polymer-Electrolyte Membranes: II. Mathematical Model. *Journal of The Electrochemical Society* **2004,** *151* (2), A311-A325.
[53] Ibid.

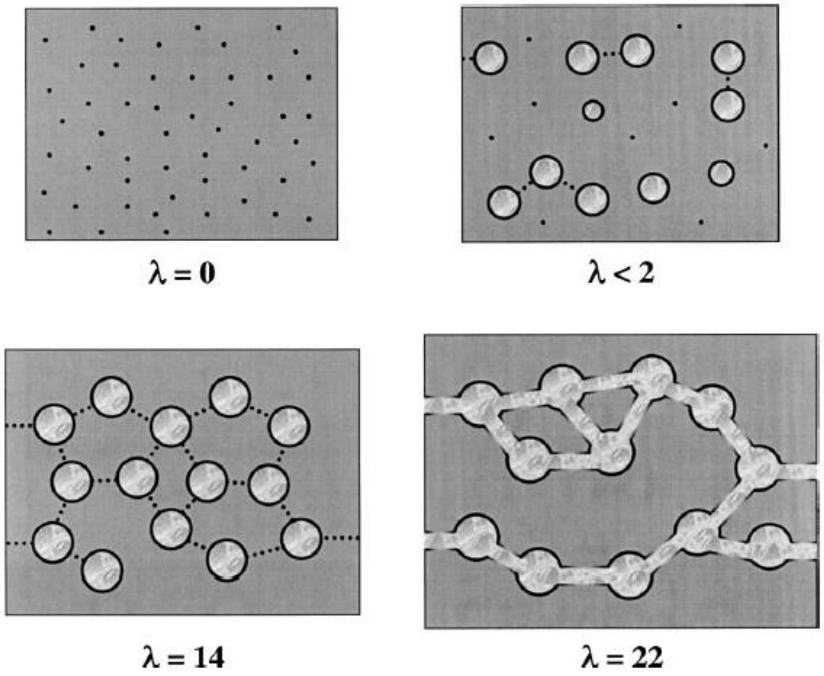

Figure 56: Adapted from Weber and Newman[54]. Evolution of the membrane structure as a function of water content, □ (moles of water per mole of sulfonic acid sites). The pictures are cross-sectional representations of the membrane where the gray area is the fluorocarbon matrix, the black is the polymer side chain, the light gray is the liquid water, and the dotted line is a collapsed channel.

Results from experimental studies of membrane water transport[55],[56] support the importance of a model framework that can describe transport in the presence of both water vapor and liquid water. These studies demonstrate that water permeation rates through conventional PFSA membrane (Nafion, NR211) are highest when one side of the membrane is contact with liquid water and the other side is in contact with water vapor. In contrast, fluxes driven by differences in water vapor concentration or by differences in liquid pressure are lower at almost all conditions (Figure 57 and Figure 58). In other words, mixed-mode transport is likely more effective than either vapor-only or liquid-only transport. As such, the membrane model should include the capability of describing all three modes of transport.

[54] Ibid.
[55] Adachi, M.; Navessin, T.; Xie, Z.; Frisken, B.; Holdcroft, S., Correlation of In Situ and Ex Situ Measurements of Water Permeation Through Nafion NRE211 Proton Exchange Membranes. *Journal of The Electrochemical Society* **2009,** *156* (6), B782.
[56] Kientiz, B.; Yamada, H.; Nonoyama, N.; Weber, A. Z., Interfacial Water Transport Effects in Proton-Exchange Membranes. *Journal of Fuel Cell Science and Technology* **2011,** *8* (1), 011013.

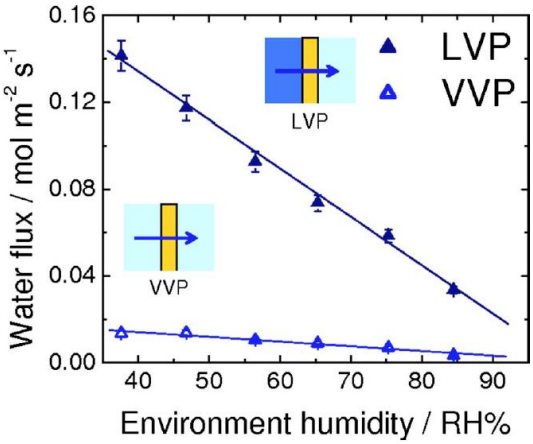

Figure 57: Adapted from Adachi et al.[57] Rate of water permeation through NRE211 at 70 C as a function of RH of the drier side of the membrane. LVP configuration = liquid water / membrane / variable RH. VVP configuration = 96% RH / membrane / variable RH.

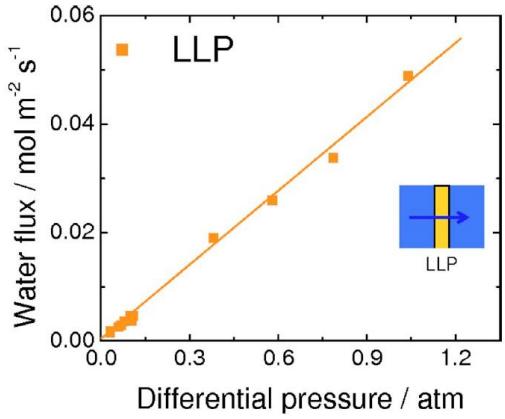

Figure 58: Adapted from Adachi et al.[58] Rate of water permeation through NRE211 at 70 C as a function of differential hydraulic pressure (LLP).

In addition to the description of intra-membrane processes, it is also important to consider interfacial water transport resistances between the membrane and adjacent phases. In experiments with bare membranes of varying thickness in the presence of both water vapor and liquid water, Kientiz et al.[59] and Monroe et al.[60] both inferred non-zero transport resistances even when the full intra-membrane transport resistance was considered (Figure 59 and Figure 60). This resistance is likely due to vaporization-sorption effects at the membrane-vapor interface. There is some disagreement from

[57] Adachi, et al, Correlation of In Situ and Ex Situ Measurements (see footnote 55).
[58] Ibid.
[59] Kientiz, et al, Interfacial Water Transport Effects (see footnote 56).
[60] Monroe, C. W.; Romero, T.; Mérida, W.; Eikerling, M., A vaporization-exchange model for water sorption and flux in Nafion. *Journal of Membrane Science* **2008,** *324* (1-2), 1-6.

the experimental studies about the relative magnitude of the interfacial resistance[61,62], however it is clear that such resistances should be accounted for when describing membrane water transport.

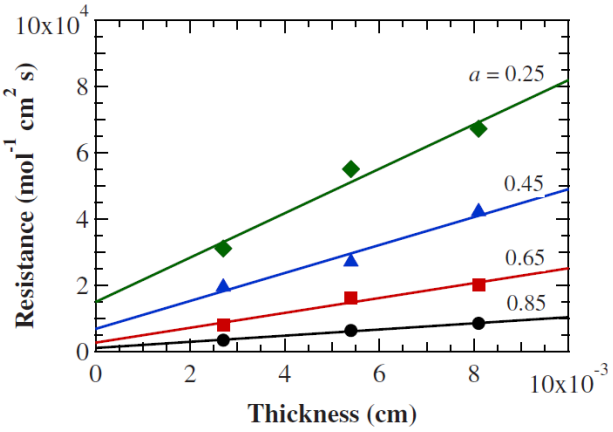

Figure 59: Adapted from Kientiz et al.[63] Total resistance to water transport in Nafion 21x membranes as a function of membrane wet thickness for different vapor activities. RH-dependence of interfacial resistance is inferred from increase in y-intercept with lower vapor activity.

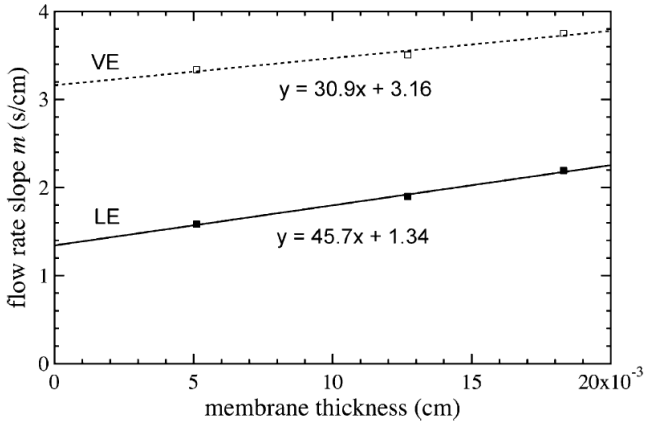

Figure 60: Adapted from Monroe et al.[64] Flow resistance as a function of Nafion 11x thickness for vapor-equilibrated and liquid-equilibrated conditions. The y-intercept of the linear fits gives the interfacial transport resistance, and the slopes represent the water permeation resistance.

[61] Cheah, M. J.; Kevrekidis, I. G.; Benziger, J., Effect of interfacial water transport resistance on coupled proton and water transport across Nafion. *J Phys Chem B* **2011,** *115* (34), 10239-50.
[62] Duan, Q.; Wang, H.; Benziger, J., Transport of liquid water through Nafion membranes. *Journal of Membrane Science* **2012,** *392-393*, 88-94.
[63] Kientiz, et al, Interfacial Water Transport Effects (see footnote 56).
[64] Monroe, et al, A vaporization-exchange model (see footnote 60).

4.2.2 Governing equations

In the presence of water, the membrane system consists of three relevant species: membrane (SO_3^-), protons (H^+) and water (H_2O)[65]. The concentrated solution approach of Fuller[66] and of Weber and Newman[67], accounts for interactions between all three species. In concentrated solutions, the driving force for transport of a species is equal to the sum of the frictional forces acting on that species due to its interactions with the other species. This results in a set of coupled, multi-component transport equations in the membrane[68],[69]. Full development of the proton and water transport equations was presented by Weber and Newman[70]; only the key equations and relationships are highlighted here.

The flux of protons, here expressed as a protonic current density i_p, and the flux of water, N_o, through the membrane can be expressed as functions of the protonic potential, Φ_p, and the water chemical potential, μ_o:

$$i_p = -\kappa \nabla \Phi_p - \frac{\kappa \xi}{F} \nabla \mu_o \quad (2)$$

and:

$$N_o = -\frac{\kappa \xi}{F} \nabla \Phi_p - \left(\alpha + \frac{\kappa \xi^2}{F^2} \right) \nabla \mu_o \quad (3)$$

where κ is the proton conductivity, α is the effective water transport coefficient, ξ is the electro-osmotic drag coefficient, and F is Faraday's constant. The gradient of chemical potential can be related to the gradients in water activity and liquid pressure by:

$$\nabla \mu_o = RT \ln a_o + \bar{V}_o \nabla p \quad (4)$$

where R is the universal gas constant, T is temperature, a_o is the water vapor activity, $\bar{V}_o$ is the molar volume of water, and p is the pressure of liquid water.

At steady-state, requirements of electro-neutrality and mass balance of water in the membrane allow for closure of the equation set in the membrane:

$$\nabla \cdot i_p = 0 \quad (5)$$

and:

$$\nabla \cdot N_o = 0 \quad (6)$$

The boundary conditions required to solve equations 2-6 are dependent upon the water state within the membrane, making this a challenge to simulate when both modes of transport are active.

Models including water transport within both membrane and the catalyst layer ionomer require that additional mass balances and internal boundary conditions be specified. Within the ionomer of the catalyst layer, equations 5 and 6 must be modified to account

---

[65] Newman and Thomas-Alyea, Electrochemical Systems (see footnote 41).
[66] Fuller, Solid-Polymer-Electrolyte Fuel Cells, *(see footnote 38)*.
[67] Weber, et al, Transport in Polymer-Electrolyte Membranes: II (see footnote 52).
[68] Fuller, Solid-Polymer-Electrolyte Fuel Cells, *(see footnote 38)*.
[69] Newman and Thomas-Alyea, Electrochemical Systems (see footnote 41).
[70] Weber, et al, Transport in Polymer-Electrolyte Membranes: II (see footnote 52).

for: i) the rate of electrochemical reaction, r_{rxn}:

$$\nabla \cdot i_p = r_{rxn} \quad (7)$$

and ii) the rate of exchange of water between the ionomer and pore space of the catalyst layer, r_{exch}:

$$\frac{\partial\left(\frac{\varepsilon_o \varepsilon_m}{\bar{V}_o}\right)}{\partial t} + \nabla \cdot N_o = -r_{exch} \quad (8)$$

where ε_o is the volume fraction of water in the membrane phase, and ε_m is the volume fraction of ionomer in the catalyst layer. The first term in equation 8 represents the accumulation term of water in the ionomer phase. Finally, the rate of water exchange can be written as:

$$r_{exch} = k(a_v - a_o) \quad (9)$$

where the rate constant k can be dependent on the local RH and a_v is the water vapor activity[71].

4.2.3 Determination of membrane properties

The membrane water content, λ (moles of H_2O / moles SO_3^-), is the key characteristic in determining the membrane transport parameters and transport mode. The volume fraction, concentration and mole fraction of water in the membrane can all be expressed in terms of the water uptake and the molar volumes of membrane and water. For a given membrane in contact with either water vapor or liquid water, the value of λ can be related to the water mass uptake, m_o:

$$\lambda = \frac{m_o/\bar{V}_o \rho_o}{m_m/EW} \quad (10)$$

where *EW* is the equivalent weight of the membrane, ρ_o is the density of water, and m_m is the mass of dry membrane. Experimental studies suggest that the magnitude of membrane swelling with water uptake is consistent with constant additive molar volumes[72,73].

In experimental studies of membrane water transport, the relative humidity is directly controlled instead of the membrane water content. Thus, the relationship between λ and relative humidity, or the sorption isotherm, must be determined[74,75,76,77]. The

---

[71] Kientiz, et al, Interfacial Water Transport Effects (see footnote 56).
[72] Fuller, Solid-Polymer-Electrolyte Fuel Cells, *(see footnote 38)*.
[73] Oberbroeckling, K. J.; Dunwoody, D. C.; Minteer, S. D.; Leddy, J., Density of Nafion Exchanged with Transition Metal Complexes and Tetramethyl Ammonium, Ferrous, and Hydrogen Ions: Commercial and Recast Films. *Analytical Chemistry* **2002,** *74* (18), 4794-4799.
[74] Zawodzinski, et al, Water Uptake (see footnote 16).
[75] Morris, D. R.; Sun, X., Water-sorption and Transport Properties of Nafion 117 H. *Journal of Applied Polymer Science* **1993,** *50* (8), 1445-1452.
[76] P. Choi, N. H. Jalani, R. Datta, Thermodynamics and Proton Transport in Nafion: I. Membrane Swelling, Sorption, and Ion-Exchange Equilibrium. *Journal of The Electrochemical Society **2005,** 152* 93), E84-E89.
[77] Ochi, S.; Kamishima, O.; Mizusaki, J., Investigation of Proton Diffusion in Nafion®117 Membrane by Electrical Conductivity and NMR. *Solid State Ionics* **2009,** *180* (6-8), 580-584.

modified chemical potential model of Weber and Newman[78] is used to calculate the isotherms. Following Fuller[79], their model assumes equilibrium between protons and water with a hydronium ion [21]:

$$H_2O + H^+ \rightleftharpoons H_3O^+ \quad (11)$$

Two equations are required to uniquely determine the sorption isotherm as a function of water activity (RH). The first of these represents the equilibrium of the chemical reaction:

$$\frac{\lambda_{H_3O^+}}{\left(1-\lambda_{H_3O^+}\right)\left(\lambda-\lambda_{H_3O^+}\right)}\exp\left(\phi_1\lambda_{H_3O^+}+\phi_2\lambda\right)=K_1 \quad (12)$$

and the second equation represents the equilibrium between water in the membrane and water in the adjacent vapor phase:

$$a_o = K_2\left(\lambda-\lambda_{H_3O^+}\right)\exp\left(\phi_2\lambda_{H_3O^+}\right)\exp(\phi_3\lambda) \quad (13)$$

where $\lambda_{H_3O^+}$ is the ratio of moles of hydronium ions to moles of sulfonic acid sites. The parameters K_1, K_2, ϕ_1, ϕ_2, and ϕ_3 are calculated by fitting an experimental sorption isotherm over a range of water vapor activity[80]. Some further modifications are required to accurately describe water uptake at very low RH and at varying temperatures. Studies of membrane water uptake at different temperatures have demonstrated a consistent decline in the water uptake with increasing temperatures[81], which can be accommodated in equation 13 through an Arrhenius temperature-dependence of K_2 [82].

Following Weber and Newman[83], it is assumed that the transition between vapor and liquid equilibrated states is determined by the fraction of the micro-pore network that has expanded due to elevated liquid pressures. For Nafion membranes, the fraction of expanded pores, S, has been estimated as:

$$S=\frac{1}{2}\left(1-\operatorname{erf}\left(\frac{\ln\left(\frac{2\gamma\cos\theta}{p}\right)-\ln(1.25)}{0.3\sqrt{2}}\right)\right) \quad (2)$$

where γ is the surface tension of water and θ is the contact angle of the ionomer / water interface. It is then this fraction of expanded pores that dictates the transition between purely vapor- and liquid-equilibrated membrane states.

The net water flux through the membrane can be expressed as a linear combination of the vapor equilibrated flux, $N_{o,v}$, and the liquid equilibrated flux, $N_{o,L}$:

$$N_o = N_{o,V}(1-S) + N_{o,L}S \quad (15)$$

Because each of the membrane transport parameters, κ, α and ξ, are also strongly dependent upon the water content[84,85], it is clear that an iterative numerical method is required for internally consistent solution of the membrane system. The approach taken

[78] Weber, et al, Transport in Polymer-Electrolyte Membranes: II (see footnote 52).
[79] Fuller, Solid-Polymer-Electrolyte Fuel Cells, *(see footnote 38)*.
[80] Weber, et al, Transport in Polymer-Electrolyte Membranes: II (see footnote 52).
[81] Luo, et al, Effect of free radical-induced degradation (see footnote 15).
[82] Weber, et al, Transport in Polymer-Electrolyte Membranes: II (see footnote 52).
[83] Ibid.
[84] Ibid.
[85] Springer, et al, Polymer Electrolyte Fuel Cell Model (see footnote 39).

in this work is presented in Figure 61. For a given set of operational conditions, initial values are determined for the membrane water uptake and associated transport properties. The transport equations are solved using the initial properties, and the updated water content is then used to update the transport properties. This procedure is then followed until the changes in the membrane water content distribution fall below a convergence tolerance.

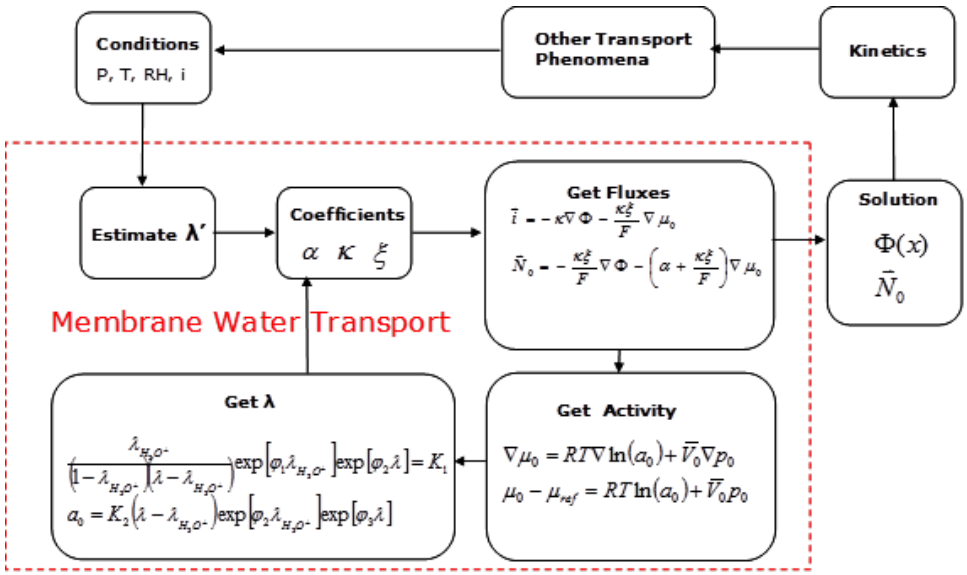

Figure 61: Iterative approach for solution of water chemical potential in fully coupled MEA model framework

4.2.4 Approach towards model development and validation

The *as-planned* high-level approach for the modeling portion of this project is summarized in Figure 62. The first stage is development of a prototype membrane sub-model in COMSOL, a commercial Multiphysics package. COMSOL allows for rapid model development, typically up to a certain level of complexity, and enables quick exploration of model physics and parameter sensitivities. Lessons learned from the prototype model are then used to develop the detailed membrane sub-model in an open source platform (Foam Extend). This model is validated against ex-situ water transport data to confirm proper implementation of physics and appropriate estimation of effective transport properties. After validation of the membrane sub-model, it is then incorporated into the FC-APOLLO MEA model, which is then used to understand possible interactions between membrane water transport and catalyst degradation.

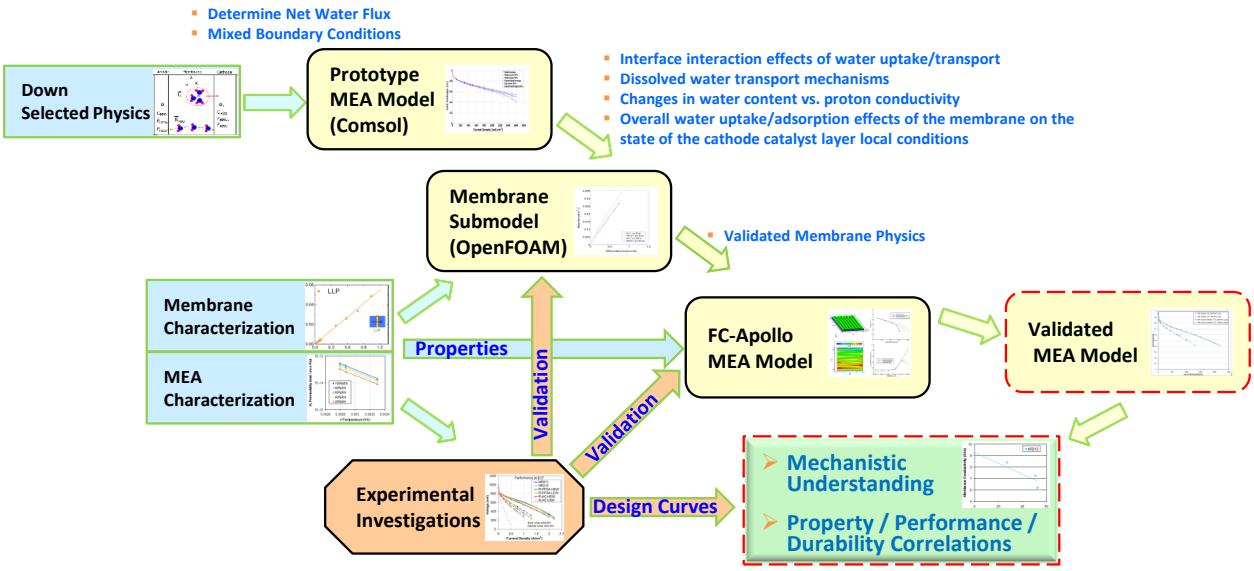

Figure 62: High-level approach for model development and validation

4.3 Prototype MEA model

The prototype model implements the membrane physics and properties outlined in the previous section within a full COMSOL-based MEA performance model. The COMSOL model was a predecessor to the Foam Extend implementation of FC-APOLLO[86], and so the assumptions made in FC-APOLLO also hold for the COMSOL model. The intent of first exploring the membrane transport physics in this framework is that model development in COMSOL is quite efficient, which enables quick exploration of model sensitivities.

The MEA model is a 1-D transient fuel cell performance model and includes the following physics:

- Gas transport in the porous domains of the MEA by diffusion (Fickian) and convection (Darcy flow)
- Heat transport in the solid phase (conduction)
- Liquid water transport in the cathode CL and cathode GDL (Darcy flow)
- Reaction kinetics for ORR and HOR in the cathode and anode CL's, respectively (Butler Volmer)
- Electron transport in the GDL's and CL's (Ohm's law)
- Proton transport in the CL ionomer (Ohm's law)

The MEA model has previously been demonstrated to agree well with MEA performance data collected at Ballard across a wide range of compositional (Pt loading, Ionomer/catalyst ratio) and operational (temperature, pressure, RH) design space. For

[86] Wessel and Harvey, Final Project Report (see footnote 24).

further details about the base MEA physics and validation, please refer to the previous DOE report[87].

The water content in the membrane is assumed to be at steady-state and to be equilibrated at the anode and cathode catalyst layer interfaces with the local vapor RH, i.e., there are no interfacial transport resistances. The membrane is assumed to only interact with the vapor phase of water in the catalyst layer pore space: liquid equilibration is dealt with in the more detailed Foam Extend implementation. Liquid water can occur in the catalyst layer, and it interacts with the membrane only through changes in the local pore space RH. Liquid water transport in the catalyst layer and gas diffusion layer (GDL) is driven by gradients in liquid saturation not by gradients in liquid pressure. To ensure consistency between the liquid water transport equations in the membrane and in the porous domains of the MEA, the detailed MEA model (Foam Extend) will have similar liquid-pressure driven transport expressions.

The prototype model was used to explore the sensitivity of membrane water crossover to current density, membrane equivalent weight, and imposed RH gradients across the MEA. Of particular interest in these simulations is the interplay between electro-osmotic drag and back-diffusion from the cathode to anode catalyst layer across the membrane.

Figure 63 shows the sensitivity of membrane water crossover to the applied current density, the cathode-anode RH difference for membrane, and the equivalent weight. An equivalent weight of 1100 g/mol was used as a baseline value for membrane. In the first set of simulations, the current density was fixed at 0.4, 0.8, and 1.6 A/cm^2, and the cathode and anode channel humidities were varied from 50% to 90% RH (dashed lines). The resulting water crossover rates vary nearly linearly with current density, implying that the main effect of current density is on the water production rate, not enhanced electro-osmotic drag. The second set of simulations used the same set of current densities and varied the anode channel RH while the cathode channel RH was fixed at 90% (solid lines). The anode-to-cathode RH difference is seen to be of secondary importance to the membrane water flux in comparison with the current density. The final simulation was at 0.4 A/cm^2, with fixed cathode RH of 90%, variable anode RH, and a lower (1000 g/mol) equivalent weight (green dotted line). The impact of the equivalent weight, in and of itself, is quite small relative to the impacts of channel RH and applied current density. These results will be revisited once the full MEA model is developed.

[87] Ibid.

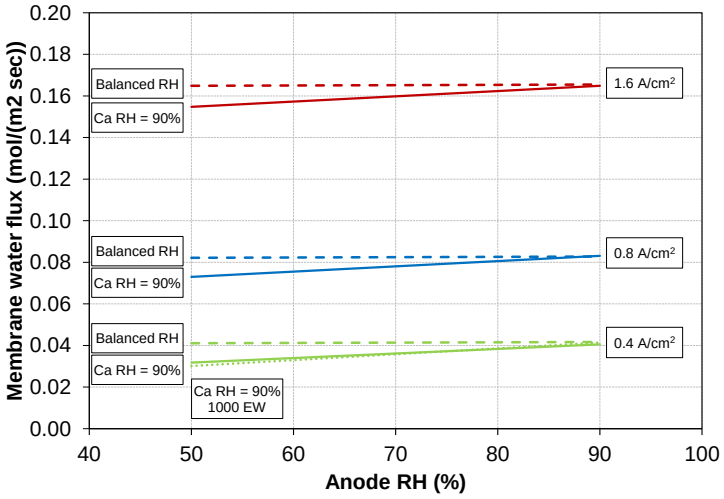

Figure 63: Prototype model predictions for balanced and unbalanced channel RH.

Figure 64 and Figure 65 show comparisons of performance predictions from the prototype MEA model with measured polarization data from standard Ballard MEA's in a standard test configuration. These data sets have been presented in the previous DOE reports, and details of the MEA configuration and test conditions are also provided[88]. Two sets of conditions are shown, with slight differences in operating temperature and pressure. Without fitting of any additional parameters, the prototype model matches the measured polarization data very well, providing some confidence that the model physics are consistent with in-situ MEA operation.

[88] Ibid.

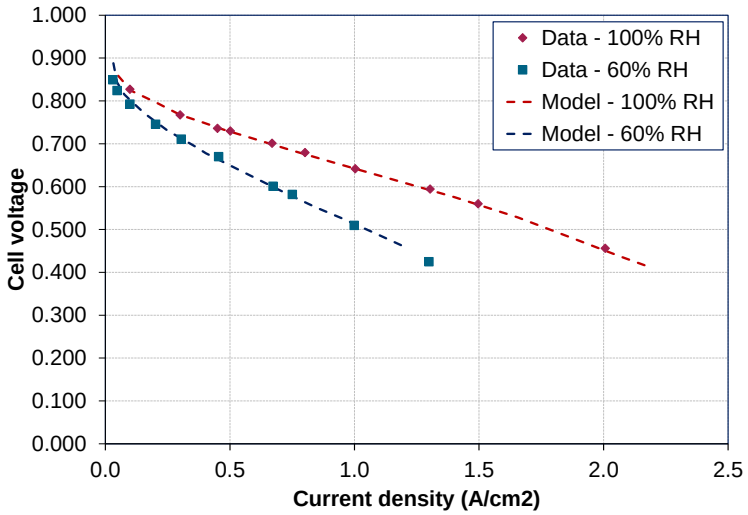

Figure 64: Performance comparison at 75ºC and 2 psig showing good agreement between prototype MEA model and data

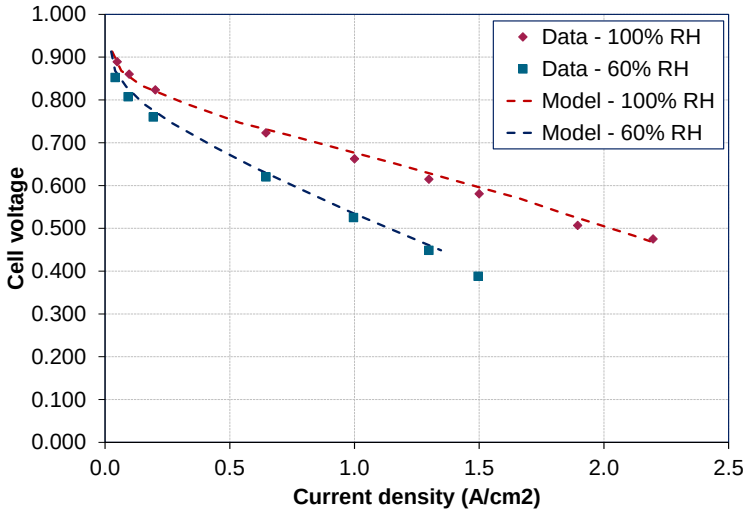

Figure 65: Performance comparison at 70ºC and 2 bar showing good agreement between prototype MEA model and data

4.4 Detailed membrane sub-model (Foam Extend)

The Foam Extend implementation of the membrane sub-model contains the membrane physics and properties presented in the background section, largely following the

approach of Weber and Newman[89]. The membrane sub-model was developed separately for several reasons: i) to verify implementation of the membrane physics, and ii) to validate the membrane physics and properties against ex-situ water transport data from literature.

Adachi et al.[90] documented water fluxes across NR211 for a range of conditions where differential liquid pressures and/or vapor concentration gradients were applied. Data from experiments at 70°C are shown as blue lines in Figure 66 and Figure 67 for vapor and liquid driving forces, respectively. Model simulations were run for comparison using single transport mechanisms (vapor-only and liquid-only): these results are shown in red lines in Figure 66 and Figure 67.

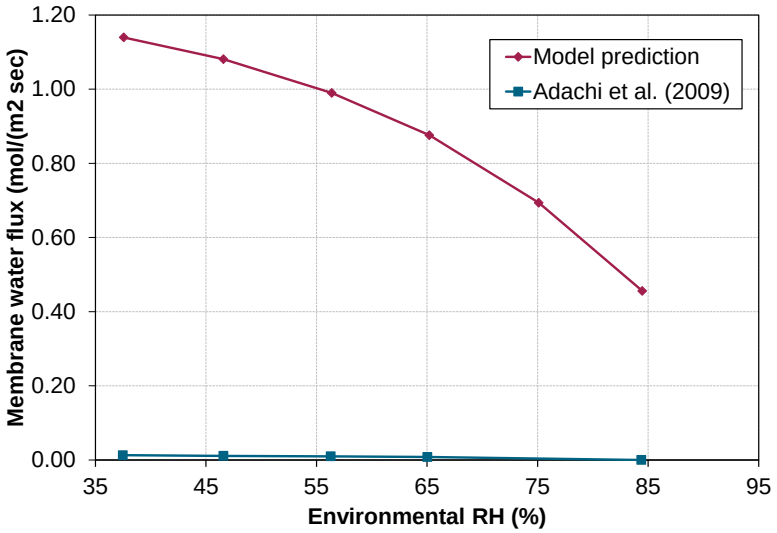

Figure 66: Measured and predicted membrane water fluxes for differential RH across the NR211 membrane at 70ºC. Configuration is 96%RH / membrane / Variable RH. Data are from Adachi et al.[91]

[89] Weber, et al, Transport in Polymer-Electrolyte Membranes: II (see footnote 52).
[90] Adachi, et al, Correlation of In Situ and Ex Situ Measurements (see footnote 55).
[91] Ibid.

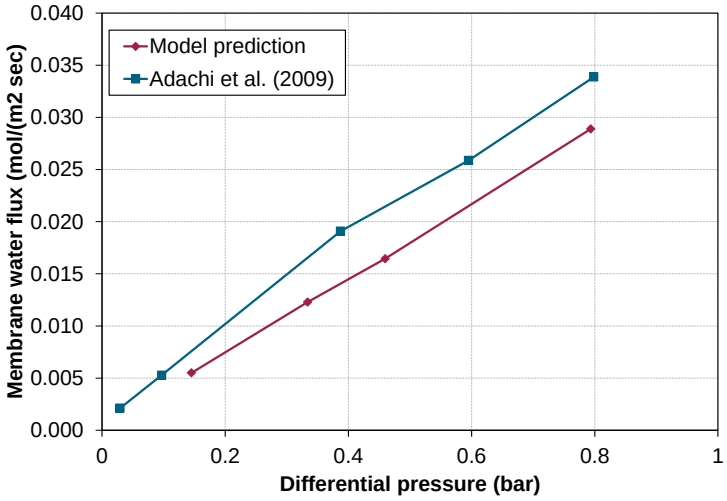

Figure 67: Measured and predicted membrane water fluxes for differential liquid pressures across the NR211 membrane at 70ºC. Data are from Adachi et al.[92]

There is reasonable agreement between model and data for the liquid driving force conditions but significant mismatch between model and data for the vapor driving force conditions. The cause of this mismatch is not known and could reside in i) missing physics or properties or ii) the implementation of the vapor-equilibrated transport physics in Foam Extend. The mismatch is directionally consistent with the model not considering interfacial transport resistances; however, experimental studies suggest that interfacial resistances are 10-50% of the total transport resistance[93,94], not the >95% required to reconcile the misfit in Figure 66. The relatively good agreement for the liquid driven experiments suggests that the more likely cause of the misfit is in the implementation of the vapor driven transport equations.

The predictive gap for vapor-driven transport was not resolved by the end of the scheduled project (Q2 2015), and as a result, the next stages of the workstream were not completed. Due to funding issues for the student's work, there was little additional progress in the remainder of 2015 or in 2016. These issues will be addressed going forward as part of follow-on work to the original project.

[92] Ibid.
[93] Kientiz, et al, Interfacial Water Transport Effects (see footnote 56).
[94] Monroe, et al, A vaporization-exchange model (see footnote 60).

4.5 Summary & Conclusions

The chemical potential approach of Weber and co-workers[95] was selected as the most promising candidate set of physics to describe water and proton transport in the membrane and catalyst layer ionomer. A prototype MEA model, including a partial set of the membrane physics, was developed and was used to explore, on a preliminary basis, the sensitivity of membrane water fluxes to channel humidity, ionomer equivalent weight and applied current density. Performance predictions from this model were found to match Ballard MEA polarization data. A more complete membrane sub-model was developed in Foam Extend but was found to significantly misfit ex-situ membrane transport data from literature.

Though the targets of complete model development and validation were not achieved by project-end, there are still plans for improvement of the model and eventual release of the open source code. The student tasked with the model development is continuing to work towards a complete model as part of his thesis, with completion scheduled for early 2018. Furthermore, with the transition of the FC-APOLLO code base into the FAST-FC platform, development of the membrane and degradation physics will continue according to a publically available roadmap. In addition, Ballard Power Systems will continue to support the work by providing access to relevant data sets for model validation.

[95] Weber, et al, Transport in Polymer-Electrolyte Membranes: II (see footnote 52).